EFFECT OF STREAMWISE/STREAMLINE PRESSURE GRADIENTS ON TURBULENT FLOW SEPARATION AT HIGH REYNOLDS NUMBERS WITH PASSIVE SCALAR TRANSPORT

by

MATTHEW HOLLAND,

DISSERTATION
Presented to the Graduate Faculty of
The University of Texas at San Antonio
In Partial Fulfillment
Of the Requirements
For the Degree of

MASTERS OF SCIENCE IN MECHANICAL ENGINEERING

COMMITTEE MEMBERS:
Guillermo Araya, Ph.D., Chair
Kiran Bhaganagar, Ph.D.
Zhigang Feng, Ph.D.

THE UNIVERSITY OF TEXAS AT SAN ANTONIO
College of Engineering
Department of Mechanical Engineering
December 2024

DEDICATION

There are a few people to dedicate this work to, so bear with me. First, my parents, who have been there since the beginning and have invested untold hours into my education leading up to college, and then even hours of discussion beyond that point. Second, my wife, Rachel, who has to exercise an inhuman amount of patience with my working through all the different aspects of graduate school. Third, my dog, Riker, who has to listen to the first draft of everything and at least pretends to understand.

ACKNOWLEDGEMENTS

Dr. Araya needs to be acknowledged first. I have certainly learned a lot with him and we have gotten to explore a variety of techniques for beginning to understand turbulence better. Dr. Roy is also acknowledged for his ability to combine his knowledge of turbulence and practical experience with OpenFOAM. Dr. Bhaganagar has been a great help as our in-class and out-of-class discussion have solved many of the issues in the analyses that blocked progress. Dr. Feng has been a great resource for understand the math, a personal weak point, and fluid mechanics behind this study. He expects a lot invested, but consistently returns much on that investment. I want to thank the Department of Mechanical Engineering of the University of Texas at San Antonio (UTSA) for providing me with the necessary resources and support to accomplish my master degree.

Finally, I want to acknowledge NSF-CAREER award #2314303 and AFOSR grant #FA9550-23-1-0241 for financially supporting this research effort. Computational time and resources are supplied by HPC UTSA and the Texas Advanced Computing Center (TACC) at UT Austin via allocation #CTS24023.

This Masters Thesis was produced in accordance with guidelines which permit the inclusion as part of the Masters Thesis the text of an original paper, or papers, submitted for publication. The Masters Thesis must still conform to all other requirements explained in the Guide for the Preparation of a Masters Thesis/Recital Document or Doctoral Dissertation at The University of Texas at San Antonio. It must include a comprehensive abstract, a full introduction and literature review, and a final overall conclusion. Additional material (procedural and design data as well as descriptions of equipment) must be provided in sufficient detail to allow a clear and precise judgment to be made of the importance and originality of the research reported.

It is acceptable for this Masters Thesis to include as chapters authentic copies of papers already published, provided these meet type size, margin, and legibility requirements. In such cases, connecting texts, which provide logical bridges between different manuscripts, are mandatory. Where the student is not the sole author of a manuscript, the student is required to make an explicit statement in the introductory material to that manuscript describing the students contribution to the work and acknowledging the contribution of the other author(s). The signatures of the Supervising Committee which precede all other material in the Masters Thesis attest to the accuracy of this statement.

December 2024

EFFECT OF STREAMWISE/STREAMLINE PRESSURE GRADIENTS ON TURBULENT FLOW SEPARATION AT HIGH REYNOLDS NUMBERS WITH PASSIVE SCALAR TRANSPORT

Matthew Holland,
The University of Texas at San Antonio, 2024

Supervising Professor: Guillermo Araya, Ph.D.

In this study, Spatially-Developing Turbulent Boundary Layer (SDTBL) detachment is numerically analyzed via the two-dimensional (2D) Reynolds-averaged Navier-Stokes (RANS) equations, and its implication on passive scalar transport. In Adverse Pressure Gradient (APG), or flow decelerating, conditions, the transport of momentum and scalars in wall-bounded flows are impeded. In strong APG conditions, this can result in flow separation which interrupts this transport behavior. Due to the reality of engineering hydrodynamic, aerodynamic, or aerothermal designs, APG conditions are all but avoidable, and thus must be studied. To achieve this, the proposed objectives are:

1. Analyze the influence of strong streamwise/streamline APG's by decelerating flow and wall curvature on massively separated flow and SDTBL at the verge of surface detachment. The geometries must be relevant and corollary to engineering applications.

2. Evaluate the performance of popular RANS and passive scalar turbulence models on strong APG conditions over flat and curved walls. The first turbulence model used is the Spalart-Allmaras model, which is common for high Reynolds numbers and is a robust RANS model. The second model is the $k-\omega$ model with Shear Stress Transport (SST) treatment or formulation due to its specialty in APG conditions. These models will be tested in high Reynolds number flows.

3. Understand the mechanisms of passive scalar transport in highly separated or separating

flows.

The objectives are achieved by numerically replicating two experimental studies from the literature. In Patrick (1987) [31], an experimental investigation of SDTBL separation with reattachment over a flat plate was carried out by prescribing a strong APG via flow potential and subsequent favorable pressure gradient (FPG) by manipulating the opposite surface. The mean flow and Reynolds stresses were measured via laser PIV, hot-wire anemometry, and pneumatic probing techniques. The significant flow deceleration, infringed on the incoming turbulent flow, produced a separated SDTBL over a streamwise distance of approximately $55cm$, representing a potential challenge for standard turbulence models. Additionally, the high momentum-thickness Reynolds number range considered in [31] ($Re_\theta \approx 11.1e3$) adds difficulties to numerical modeling and computational resources. The second reproduced experimental setup was conducted by So and Mellor (1972) [41]. They investigated the effect of uniform (zero-pressure gradient) and moderately adverse pressure distributions on incoming SDTBL's along convex and concave walls. The hot-wire measurements confirmed the enhancement of turbulent mixing over the concave surface, while the opposite occurred in the convex surface.

The Computational Fluid Dynamics (CFD) analysis is performed with the open-source flow solver OpenFOAM using the IncompressibleFluid solver that uses the SIMPLE methodology, on UT Austin's TACC Lonestar6 system.

The RANS models in 2D steady CFD are able to simulate the conditions prior to and just into separation, but struggle to reach full separation or reattachment. Additionally, the normal stresses that a curvature imposes on the RANS models appears to cause issues with the CFD analysis coming to a resolved solution. This may be due to the 2D steady analysis that the RANS models are used in, and potential solutions are highlighted in this study.

TABLE OF CONTENTS

LIST OF TABLES

LIST OF FIGURES

0.1 Acronyms

2D	Two-dimensional, lacking the spanwise dimension
APG	Adverse Pressure Gradient, or decelerating flow
CFD	Computational Fluid Dynamics
CPU	Central Processing Unit, vernacular name for traditional processor achitecture
DNS	Direct Numerical Simulation, CFD simulation to resolve all scales of motion
FPG	Favorable Pressure Gradient, or accelerating flow
ID	Incipient Detachment, where detachment occurs 1% of the time
ITD	Intermittent Transitory Detachment, where detachment occurs 20% of the time
LES	Large Eddy Simulation, CFD where resolved motions are filtered
MSc	Masters of Science
NACA	National Advisory Committee for Aeronautics
PDE	Partial Differential Equation, where function depends on multiple parameters
PIV	Particle Image Velocimetry, flow visualization by particle tracking
RAE	Royal Aircraft Establishment, UK counterpart of NACA
RANS	Reynolds-Averaged Navier Stokes, typically appied to turbulence modeling
RMS	Root-Mean Square
SA	Spalart-Allmaras, specifically the one-equation turbulence model
SST	Shear Stress Transport
SIMPLE	Semi-Implicit Method for Pressure Linked Equations
STDBL	Spatially Developing Turbulent Boundary Layer
TACC	Texas Advanced Computing Center
TKE	Turbulent Kinetic Energy, k

0.2 Variables

∇	Del operator in vector space
∇^2	Laplacian operator, $\nabla \cdot \nabla$
α	Thermal diffusivity
$alpha$	OpenFOAM's inversion of Schmidt number
γ_{pu}	Intermittent backflow fraction, amount of flow reversed as fraction of time
Γ	Diffusion coefficient, effective if no subscript, effective is molecular if laminar
δ	Boundary layer thickness
δ^*	Displacement boundary layer thickness
ϵ	Error
θ	Momentum boundary layer thickness
κ	von Karman constant
μ	Dynamic viscosity, molecular if no subscript
ν	Kinematic viscosity, molecular if no subscript
Π	Wake parameter
ρ	Density
σ	Model constant for RANS models
τ	Stress, particularly shear stress
ϕ	Generic function, scalar as applicable
χ	Ratio of modified viscosity, $\tilde{\nu}$, to viscosity, ν
ω	Specific dissipation of turbulence
Ω	SST term to bound wall-normal stress treatment

a	Model coefficient
$C_?$	Model constant
C_f or Cf	Skin friction coefficient, wall shear stress normalized by freestream kinetic energy
C_p	Pressure coefficient, pressure difference to reference point normalized by freestream kinetic energy
dP	Pressure difference
$\frac{D}{Dt}$	Convective derivative operator, $\frac{\partial}{\partial t} + \mathbf{u} \cdot \nabla$
f or F	Function
$\mathbf{g}$	Reference frame acceleration
k	Turbulent kinetic energy, $\|\|\mathbf{u}'\|\|^2$
$k - \omega$	RANS turbulence model
N	Location of maximum backflow
P or p	Pressure
Pr	Prandtl number, ratio of momentum diffusivity to thermal diffusivity
P'	Kinematic pressure or P/ρ
R	Local radius
Re	Reynolds number, subscript describes dimensional size
$\mathcal{S}$	Source function
Sc	Schmidt number, ratio of momentum diffusivity to scalar diffusivity
streamwise	Parallel to streamline
t	Time
$\mathbf{u}$	Velocity vector
u_N	Velocity of maximum backflow
U or $\overline{U}$	Mean streamwise velocity
$\mathbf{u}'$	Fluctuating component velocity vector
$\overline{\mathbf{U}}$	Mean velocity vector
x	Streamwise coordinate without subscript, vector component with Einstein notation subscript
y	Wall-normal coordinate
y'	Wall-normal coordinate normalized by boundary layer height, y/δ

0.3 Subscripts & Superscripts

$\overline{variables}$	Ensemble time average
$\tilde{variables}$	Model modified value
$variable'$	Fluctuating component of Reynolds decomposition
$^+$	Wall units via Log Law of the Wall
$_\infty$ or $_{inf}$	Fresstream value
$_0$	Reference value
$_\tau$	Pertaining to shear
$_e$	Equilibrium flow value, about freestream values if boundary layer $threshold$ is near unity
$_{eff}$	Effective value for RANS model
$_{i,j,k}$	Components of vectors in Einstein notation
$_t$	Turbulent values
$_T$	Thermal values
^{T}	Transpose
$_w$	At the wall

CHAPTER 1: INTRODUCTION

The proposed body of work focuses on numerical modeling and replicating wind-tunnel experiments previously performed by Patrick [31] and So and Mellor [41]. These studies evaluated the effects of streamwise and streamline APG's due to an increasing cross-sectional section in a diffuser and wall curvature on incompressible SDTBL's. This behavior is referred to as an Adverse Pressure Gradient (APG) [28] or flow deceleration. If the APG strength on turbulent wall-bounded flows is large enough, the wall bounded flow (i.e., SDTBL) will experience significant distortions; and, eventually, surface detachment. Flow separation is a pressing issue in fluid dynamics since it induces rapid changes in the boundary layer parameters due to an abrupt thickening of the rotational flow region, called a recirculation bubble, close to the wall. This unwanted effect induces a critical reduction in the operation performance of engineering and thermal-fluids devices (e.g., airfoils and turbine blades). The major reasons why the separation of turbulent wall-bounded flows is so complicated to model and measure are (i) large separation of turbulent scales, (ii) highly unsteady and non-linear phenomena, (iii) challenges to determine near-wall pressure fluctuations, and (iv) the outer region becomes blended with the inner region and a new reverse flow region forms [35]. To our knowledge, the influence of strong APG on scalar transport has not been scrutinized in detail, specifically concerning isolation of specific circumstances and effects. The numerical study of the turbulent transport phenomena in SDTBL's subject to strong pressure gradients exhibits the following difficulties:

1. The shear behavior at the wall changes since there is an inflection point (like a change in the profile curvature) in the wall-parallel velocity profile due to a negative curvature at the wall (i.e., $\frac{\partial^2 u}{\partial x^2}|_{wall} = \frac{1}{\mu}\frac{dp}{dx} < 0$), given by the negative or adverse pressure gradient, dp/dx. At the separation or detachment point, the shear is zero (i.e.: $\frac{\partial u}{\partial x}|_{wall} = 0$) [28].

2. The different transport mechanisms of momentum and passive scalars (viscous diffusion, convection, turbulent mixing, etc.) are significantly impacted by strong streamwise/streamline pressure gradients, representing real challenges in modeling these flow behaviors [45].

3. It is well known that pressure gradient is a source of dissimilarity between the momentum and passive scalar fields [7, 8], which means that its presence causes a breakdown of the Reynolds analogy [27].

4. High Reynolds numbers considered in wind-tunnel experiments add substantial complications to numerical modeling and computational resources. Particularly, larger computational domains are required even under RANS approaches, making almost mandatory parallel CPU usage.

1.1 Flow Separation Phenomenon

The transport phenomenon in realistic flows generally occur under complicated external conditions, such as pressure gradients (favorable and adverse), complex geometry (concave/convex surface curvatures), high Reynolds numbers, and Spatially-Developing Turbulent Boundary Layers (SDTBL).

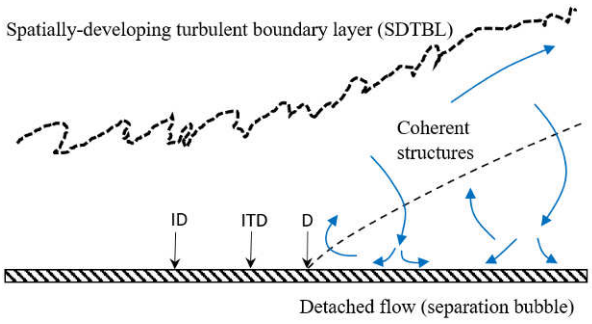

Figure 1.1: Cartoon of 2D Turbulent Boundary Layer Separation. Adapted from Simpson [35].

The separation of boundary-layer flow, caused by the presence of a sufficiently strong Adverse Pressure Gradient (APG), represents by far the most unwanted situation in the momentum or scalar transport of thermal-fluid problems. The boundary layer parameters experience sudden changes due to the presence of backflow close to the wall [45]. This negatively impacts the performance of engineering devices (e.g., increased drag on airfoils or heat flux decrease to turbine blades, to name a couple). For this reason, flow separation has been the subject of various theoretical, experimental, and numerical studies in the past few decades [34] [38], but there is still much to investigate. Figure 1.1 shows a schematic of the 2D turbulent boundary layer separation in low-curvature and flat surfaces according to Simpson in [35]. The dashed line indicates $U = 0$, and detachment (D) occurs where the time averaged wall shear stress is zero. Moreover,

the incipient detachment (ID) and intermittent transitory detachment (ITD) take place at locations where instantaneous backflow occurs 1% and 20% of the time, respectively. Thus, like most turbulent phenomenon, the separation point fluctuates with time with a mean value approximation. As the boundary layer encounters an APG, the near wall region flow decelerates until some backflow first takes place at the ID point. this reverse flow is attributed to the transport of outer momentum toward the wall by the large-scale, coherent structures [35].

Relevant to the present study is the analysis of passive scalar transport under the previously mentioned situation. The turbulent transport of passive scalars is crucial in many industrial applications of technological importance, such as in turbine-blade film cooling, heat transfer in electronic and mechanical devices, species dissolved or suspended in fluids, contaminants or humidity dispersed in atmospheric flow, to name a few. Furthermore, a passive scalar is defined as a diffusive contaminant that exists in such a low concentration in a flow that it has no effect on the dynamics of the fluid motion, Warhaft [44]. However, that low concentration of passive scalar is sufficient to cause a significant impact on energy expenditures, air pollution and design of chemical processes.

1.2 Application

The present study will contribute to the knowledge of fluid mechanics and scalar transport as applied to a variety of areas, including rotating machinery [31, 41], rocket nozzles, aircraft airfoils, and other wall-bounded flows [36]. When working with airfoils of many applications, and likely non-airfoil bounded flows, this separation issue determines the bounds of the operating envelope for engineered components [31]. Figure 1.2 shows a typical turbine blade and the separate flow distribution due to streamwise/streamline adverse pressure gradients. The current research efforts are done with an

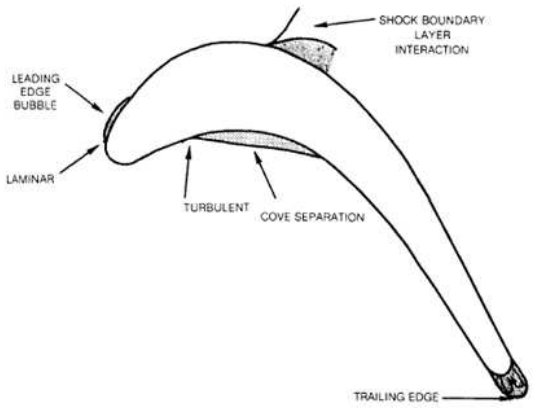

Figure 1.2: Illustration of Flow Separation on an Airfoil. Original Figure 1-1 from [31].

incompressible flow assumption - low Mach numbers with zero divergence in the velocity field, which is also aligned to the wind-tunnel experiments in [31] and [41]. Separation from shock waves interacting with the incoming turbulent boundary layer is beyond the scope of the present study. Furthermore, there are multiple ways to compensate for behavior changes caused by a separation of the boundary layer when dealing with wall-bounded flows in their applications, namely:

1. The turbulent eddy viscosity of the flow is modified by flow separation [45]. This, in turn, effectively changes the momentum diffusivity inside the turbulent boundary layer [32]. This change in one diffusivity raises the question of how the diffusivity of other scalars like temperature, contaminants or pollutants (i.e., passive scalars) will accommodate, altering the turbulent Prandtl/Schmidt numbers away from the Reynolds analogy [27], reportedly more determined by the wall pressure than viscosity [23], [40]. The breakdown of the Reynolds analogy is caused by the presence of strong FPG as well, according to [9].

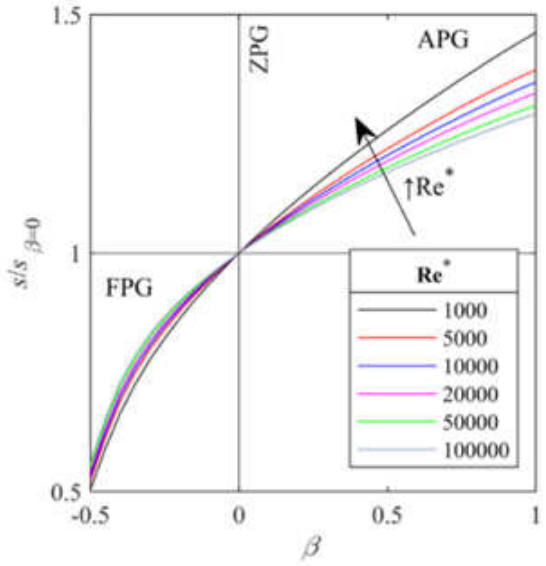

Figure 1.3: Relation of Pressure Gradient and Reynolds Analogy Factor. Reynolds Analogy Factor calculated using methods in [40]. Originally Figure 1(c) from [27].

2. The mixing length can change the overall behavior of the flow [45]. Some multiple models and correlations can be used. White and Majdalani [45] describe simple empirical models [45], and Simpson proposes more complex ones with comparisons to canonical data [36].

3. Higher order models like the Reynolds-Averaged Navier-Stokes (RANS) models can form a Partial Differential Equation (PDE) method for finding the same alterations. This provides a way to calculate the scalar transport through the flow for more complex situations that would

be experienced in an engineering context.

1.3 The Reynolds-Averaged Navier-Stokes (RANS) Equations

The premise of discretizing the fluid flow is that various fluxes and scalars convect, diffuse, are generated or destroyed in the flow, and these activities can be simulated by solving a set of PDE's. The generalized form can be seen in 1.1, where $\Gamma\nabla^2\phi$ is the diffusion term by diffusion value Γ, and $\mathcal{S}$ is the source and sink terms, with sinks being negative sources. A well-known case is the Navier-Stokes Equation, which focuses on the transport of momentum, as seen in 1.2 from [28].

$$\frac{D\phi}{Dt} = \Gamma\nabla^2\phi + \mathcal{S} \tag{1.1}$$

$$\frac{D\rho\mathbf{u}}{Dt} = \mu\nabla^2\mathbf{u} + \nabla P + \mathbf{g} \tag{1.2}$$

The RANS modeling methods takes advantage of the application of the general convection-diffusion equation to say that there are certain scalars that follow this behavior. In the case of the Spalart-Allmaras model, a modified viscosity is what is transported by a single equation [42]. In the case of the two-equation k-based models, the turbulent kinetic energy (TKE or k) is transported through the flow, with a dissipation term that is transported by another equation. In this study, the k-ω model transports a specific dissipation, which provides destruction and diffusion of the turbulent kinetic energy [46]. Here, the variable ω is the specific rate of dissipation.

The transport, diffusion, and generation/destruction affect the momentum via the RANS mean-momentum equation, seen in Equation 1.3 adapted from [32], which is the interface of the RANS models to the momentum. The effective viscosity is the summation of molecular and turbulent viscosity, i.e.: $\nu_{eff} = \nu + \nu_t$. Turbulent viscosity, ν_t, comes from the average fluctuations of turbulent flow per Equation 1.4 as adapted from [32].

$$\frac{D(\rho\overline{\mathbf{U}})}{Dt} = \nabla\left(\nu_{eff}\left(\nabla\overline{\mathbf{U}} + \left(\nabla\overline{\mathbf{U}}\right)^T\right)\right) - \frac{2}{3}\nabla k - \nabla P' \tag{1.3}$$

$$-\overline{\mathbf{u}'\mathbf{u}'} + \frac{2}{3}\delta k = \nu_t \left(\nabla \overline{\mathbf{U}} + \left(\nabla \overline{\mathbf{U}} \right)^T \right) \tag{1.4}$$

There are other ways to model turbulence for the conditions expected in the separating flow, like Large-Eddy Simulation (LES) [32] or some hybrid method between such and RANS. However, the assessment is focusing on if a 2D steady model can adequately model APG conditions, lending the analysis to a RANS model. Additionally, without a known mixing length from the experiments, tuning more advanced models may take more scope for the assessment than would be worth.

1.3.1 The Spalart-Allmaras (SA) Model

The central premise of the Spalart-Allmaras (SA) model [42] is that the effective kinematic viscosity, is responsible for diffusing momentum in the Navier-Stokes equations of turbulent flows. Equation 1.5 is the central equation for the SA model and shows the different transport mechanism terms of the scalar $\tilde{\nu}$. $\tilde{\nu}$ is a modified turbulent viscosity as it is related to turbulent viscosity via a blending function, $\nu_t = \tilde{\nu} f_{v1}$, where $f_{v1} = \frac{\chi^3}{\chi^3 + C_{v1}^3}$ and $\chi = \tilde{\nu}/\nu$.

$$\frac{D\tilde{\nu}}{Dt} = C_{b1}(1 - f_{t2})\tilde{S}\tilde{\nu} + \frac{1}{\sigma}(\nabla \cdot ((\nu + \tilde{\nu})\nabla\tilde{\nu}) + C_{b2}|\nabla\tilde{\nu}|^2) - (C_{w1} f_w - \frac{C_{b1}}{\kappa^2} f_{t2})(\frac{\tilde{\nu}}{d})^2 + f_{t1}\Delta U^2 \tag{1.5}$$

The above equation 1.5 possesses five terms, and the physical meanings will be further explained. The term on the left-hand side represents the material or convective derivative of scalar $\tilde{\nu}$, involving the convection of the scalar that is traveling through the flow, and its rate of change. The first term on the right-hand side is the production term. This term has a constant that is fitted to canonical data and a function that describes the production from laminar boundary layer behavior. The second term on the right-hand side is the diffusion term, with constants that are fitted and confirmed to canonical data. The third term on the right-hand side is the destruction or dissipation term. There are two sub-terms, the first is a destruction term that models near-wall behaviors, and the second is a term that describes the destruction by laminar boundary layer behaviors. The final term is a boundary layer trip term, which makes the SA model insensitive to boundary layer

tripping.

For more details on the derivation and the data that is the basis for the constants and functions, readers are referred to the original document [42] where the authors walk through the development of the SA model in detail. However, to summarize the overall methodology, the SA model takes advantage of the self-similarity between turbulent behaviors by fitting a model to the self-similar parameters.

1.3.2 The $k-\omega$ Model with Shear Stress Transport (SST) Treatment

In 1988, Wilcox [46] developed the k-ω RANS model that allows turbulence and dissipation to be transported by the turbulent kinetic energy, k, as shown by eq. 1.6, and the specific dissipation, ω, as depicted by eq. 1.7, respectively.

$$\frac{D\rho k}{Dt} = \tau_{ij}\frac{\partial u_i}{\partial x_j} - \beta^*\rho\omega k + \frac{\partial}{\partial x_j}((\mu + \sigma_{k1}\mu_t)\frac{\partial k}{\partial x_j}) \tag{1.6}$$

$$\frac{D\rho\omega}{Dt} = \frac{\gamma_1}{\nu_t}\tau_{ij}\frac{\partial u_i}{\partial x_j} - \beta_1\rho\omega^2 + \frac{\partial}{\partial x_j}((\mu + \sigma_{\omega 1}\mu_t)\frac{\partial \omega}{\partial x_j}) \tag{1.7}$$

However, Menter in 1993 [26] pointed out that there were significant shortcomings in this model. First, Menter points out that the original k-ω model is extremely sensitive to the freestream conditions that feed into the model. Second, the k-ω approach inaccurately models flow separation under APG conditions. In this discussion, Menter's changes to the k-ω model are glossed over to discuss and propose the new Shear-Stress Transport (SST) modeling or treatment addition. The SST model is an alternative formulation of RANS models to improve normal stress modeling. Since the turbulent stresses are allowed to be transported, it follows the same convection behavior as other scalars, as seen in equation 1.8, where the stress tensor is defined in eq. 1.9.

$$\frac{D\tau}{Dt} = \frac{\partial \tau}{\partial t} + \mu_k\frac{\partial \tau}{\partial x_k} \tag{1.8}$$

$$\tau = -\rho\overline{u_i' u_j'} \tag{1.9}$$

This changes the calculation of the turbulent viscosity from a single ratio calculation that simply considers a shear to a calculation that accepts both shear and rotational conditions, with those rotational conditions being more prominent in separation. The basis of this calculation is shown in equation 1.10.

$$\nu_t = \frac{a_1 k}{max(a_1\omega, \Omega)} \tag{1.10}$$

However, this equation does not handle the blending between the SST and baseline conditions of the standard or modified k-ω model. Thus, the eddy viscosity is finally defined by 1.11, which is supported by the functions in eqns. 1.12 and 1.13.

$$\nu_t = \frac{a_1 k}{max(a_1\omega, F_2\Omega)} \tag{1.11}$$

$$F_2 = tanh(a_2^2) \tag{1.12}$$

$$a_2 = max(2\frac{\sqrt{k}}{0.09\omega y}, \frac{500\nu}{t^2\omega}) \tag{1.13}$$

According to the data that Menter presents in [26], there is not a strong effect on the shear stresses, but there is a significant improvement in wall-normal forces.

1.3.3 Turbulence Models for Passive Scalar Transport

Whereas the major objective in the present project is to assess popular turbulence models, such as the $k-\omega$ SST and the SA models, under extreme external conditions (i.e., at very high Reynolds numbers and flow separation), an important intellectual merit of the present analysis is the prediction of passive scalars under such extreme conditions. By definition, a passive scalar is that diffusive contaminant or pollutant (e.g., temperature, humidity, etc.) that exists in such a low concentration in a fluid flow that it does not possess any influence on the dynamics of the fluid

motion. Such quantity is transported and does not directly affect the fluid flow described by the momentum equation. For instance, if the temperature difference in the thermal turbulent boundary layer is assumed small, the buoyancy forces and temperature dependence of material properties can be assumed negligible. Therefore, the temperature may be treated as a passive scalar, and the momentum and the passive scalar transport equations are uncoupled. The passive scalar transport equation becomes a linear problem. It is well known that pressure gradients (either adverse or favorable pressure gradients) are sources of dissimilarity between the momentum and passive scalar fields, causing the breakdown of the Reynolds analogy [7–9, 27]. Additionally, this can also apply to other passive scalars, say species concentration for a suspended species in a homogeneous mixture, like the titanium dioxide Patrick [31] used for PIV.

Since RANS models find turbulent viscosity, the turbulence models consider the contribution to diffusion of momentum within the model itself. In certain applications, scalar transport like energy or species in a homogeneous mixture is a vital study for CFD. The category passive is applied when the scalar transport does not affect the transport of mass or momentum for the fluid or homogeneous fluid mixture.

Let's assume that the instantaneous passive scalar, ϕ, (e.g., temperature, humidity, chemical species, pollutant, contaminant, and particles) can be decomposed using the classical Reynolds decomposition, as seen in Equation 1.14: a time-averaged component, $\overline{\phi}$, plus a fluctuating component, ϕ'. The mathematical procedure is similar to the one applied in the obtention of the Reynolds-averaged NS equations. Briefly, the instantaneous variable ϕ is substituted in the advection-diffusion passive scalar equation by $\overline{\phi}$ + ϕ' and the time average is taken in the full equation. After breaking down all terms and by making the corresponding assumptions on the time-averaged correlated values for mean and fluctuations, the Reynolds-averaged passive scalar transport equation is obtained. It can be shown that the turbulent diffusivity for the passive scalar results in the gradient-diffusion hypothesis, seen in Equation 1.15 [32].

$$\phi = \overline{\phi} + \phi' \tag{1.14}$$

$$\overline{\mathbf{u}'\phi'} = -\Gamma_t \nabla \overline{\phi} \tag{1.15}$$

The effective diffusion for the passive scalar is the summation of this turbulent diffusion, Γ_t, and the molecular behavior diffusion, Γ, as seen in Equation 1.16. This results in an equivalent mean flow behavior, seen in Equation 1.17. For momentum, this diffusion is obviously viscosity, specifically kinematic viscosity, ν, in this study [32]. For thermal energy or temperature difference, this is called thermal diffusivity, or α. The ratio of the momentum to the thermal diffusivity is the Prandtl number, as defined by Equation 1.18, describing the ratio of diffusion of momentum to thermal energy [45]. For species, this is simply a species diffusion, as per Fick's law [32]. For air, the Prandtl number will be near unity (1), but there are also algebraic solutions based on the momentum and heat transfer conditions that come from the Crocco-Busemann relation [45].

$$\Gamma_{eff} = \Gamma + \Gamma_t \tag{1.16}$$

$$\frac{\overline{D\phi}}{\overline{Dt}} = \nabla \cdot \left(\Gamma_{eff} \nabla \overline{\phi} \right) \tag{1.17}$$

$$Pr = \frac{\nu}{\alpha} \tag{1.18}$$

A more general form of the Prandtl number is the Schmidt number, which describes simply any scalar diffusivity parameter, Γ, like in Equation 1.19. Given that diffusion breaks into a turbulent and mean flow quantities for both momentum and the passive scalar, Schmidt, and Prandtl number, form a turbulent quantity like

$$Sc = \frac{\nu}{\Gamma} \tag{1.19}$$

In a similar way that eddy viscosity models focus on setting a closure for the turbulent stresses (convective terms) via an effective fluid viscosity (ν_{eff} = $\nu_{molecular}$ +ν_t), an analogous concept is

applied to turbulent passive scalar flux modeling. The effective passive scalar diffusivity is defined as the contribution of the molecular and turbulent diffusivity, as shown by eq. 1.16. In the present analysis, the simple turbulent Prandtl or Schmidt number model is used in OpenFOAM [4] to compute the turbulent heat or passive scalar fluxes.

$$\Gamma_t = \nu_t / Sc_t \tag{1.20}$$

where Sc_t is the turbulent Schmidt number, which is assumed constant inside the turbulent boundary layer, and it depends on the considered molecular Schmidt number. Furthermore, the turbulent eddy viscosity, ν_t, varies in the wall-normal direction, being computed by the turbulence models described in §1.3.1 and §1.3.2.

1.4 Overview of Original Studies

In this section, experimental studies conducted by Patrick [31] and So & Mellor [41] are summarized. The collected sampling data was utilized for numerical validation purposes in this project. For the purposes of this project, a chief assumption is that the experiments were valid and produced quality data worthy of comparison. Questions of validity and uncertainty of the data should be addressed at the original studies.

1.4.1 Patrick Diverging-Converging Duct

Patrick [31] modified a test stand at the United Technologies Research Center to investigate the phenomenon of incompressible turbulent boundary layer separation, specifically aimed at addressing a turbomachinery application. The test section is illustrated in Figure 1.4. This produces a relatively simple set of data where the flow separation occurs over a flat plate, which removes any surface curvature effects in the turbulence statistics. Patrick [31] then measured the fluid flow and turbulence as the flow created a long separation bubble (of approximately 55 cm in length) where the boundary layer had detached, as observed in the schematic of Fig. 1.5. Notice the presence of “boundary layer scoops" in the lower diverging wall. According to [31], the scoops were designed

to bleed the incoming APG flow and to “force the lower wall boundary layer to remain attached throughout the strong adverse pressure gradient field required to produce 2D separation on the test surface". Furthermore, Patrick validated a 2D assumption via measurements. The mean flow and velocity fluctuations were measured via laser Doppler velocimetry, hot-wire anemometry, and pneumatic probing techniques. This study provides data on the mean flow wall-normal profiles (U and V), wall mean pressure coefficients (C_p), skin friction coefficients (C_f), Reynolds normal stresses (u'^2 and v'^2), as well as Reynolds shear stresses ($u'v'$) at several streamwise stations. For the straightforward comparison against the present RANS simulations, the following experimental data will be employed: U, V, C_p, and C_f. It is important to mention that the wind-tunnel analysis conducted by [31] presents the following numerical challenges:

1. Prescription of very strong APG and subsequent favorable pressure gradient (FPG) for flow reattachment purposes by manipulating the opposite surface, which induces severe distortion to the incoming SDTBL.

2. Massively separated flow, which is highly non-linear and unsteady.

3. Large-scale systems (wind-tunnel facility) and very high (experimental) Reynolds numbers ($Re_\theta \approx$ 11,100 - 55,000). Where $Re_\theta = U_\infty \theta/\nu$, here U_∞ is the freestream velocity, θ is the momentum thickness, and ν is the kinematic fluid viscosity.

4. Adequate setup of the boundary layer scoop on the opposite wall with the correct outlet pressure to avoid or minimize flow separation in that wall.

As previously mentioned, the phenomenon of massively turbulent flow separation is a highly unsteady problem. Selecting RANS as the numerical approach to predict it might be considered a restricted or inadequate methodology since the “RANS philosophy is to **resolve** the time-averaged solutions of the Navier-Stokes equations" by basically modeling the full velocity fluctuation spectra. However, it can provide *important first insights into the fluid dynamics problem quickly at a low computational cost*, making it an attractive “initial exploration numerical technique" for future

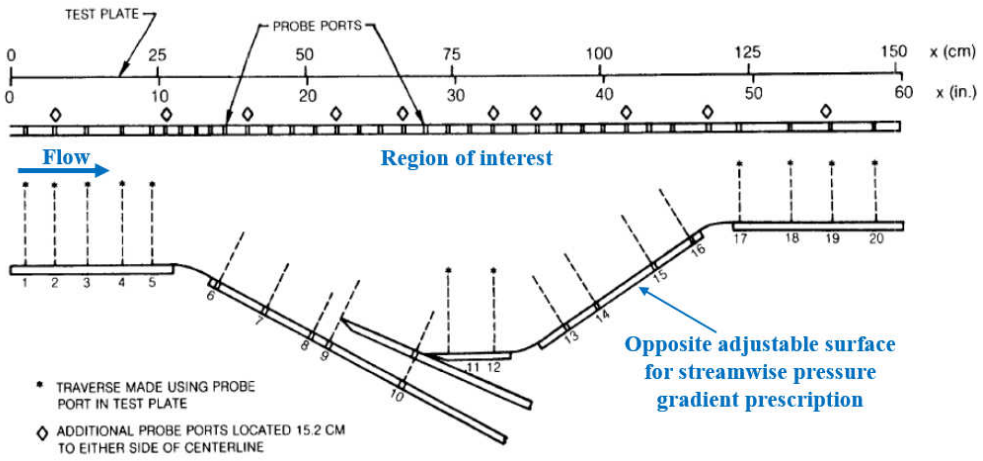

Figure 1.4: Experimental Test Section from Patrick. Adapted from Figure 3-6 in [31].

time-dependent three-dimensional flow solvers, such as Large-Eddy Simulations (LES) and Direct Numerical Simulation (DNS).

A more thorough review and comprehensive information for readers can be found in Appendix A.

1.4.2 So and Mellor Two-Dimensional Duct

So and Mellor [41] built a wind tunnel to scrutinize the effect of uniform (i.e., streamwise zero-pressure gradient, ZPG, or constant streamwise distribution of duct cross-sectional areas) and moderately adverse pressure distributions on incoming SDTBL's along convex and concave walls. The latter case was achieved by adjusting the top (concave) surface in order to impose an increasing cross-sectional area. The top wall modification generated a streamwise APG on the incoming flow. This second case was called "separating flow" in their studies since the SDTBL never detached from the convex surface. The measured mean skin friction coefficient, C_f, exhibits a clear decreasing trend but never achieves a zero value. If those conditions were preserved for a longer distance, the SDTBL would eventually separate from the wall. That is the major reason why they called "separating flow" to this case. On the other hand, the first case was labeled as "constant pressure flow". The selected measurement technique was the hot-wire technology. Their wind-tunnel measurements corroborated the intensification of turbulent mixing over the concave surface, while the opposite occurred on the convex surface. A schematic of the utilized wind tunnel is shown in

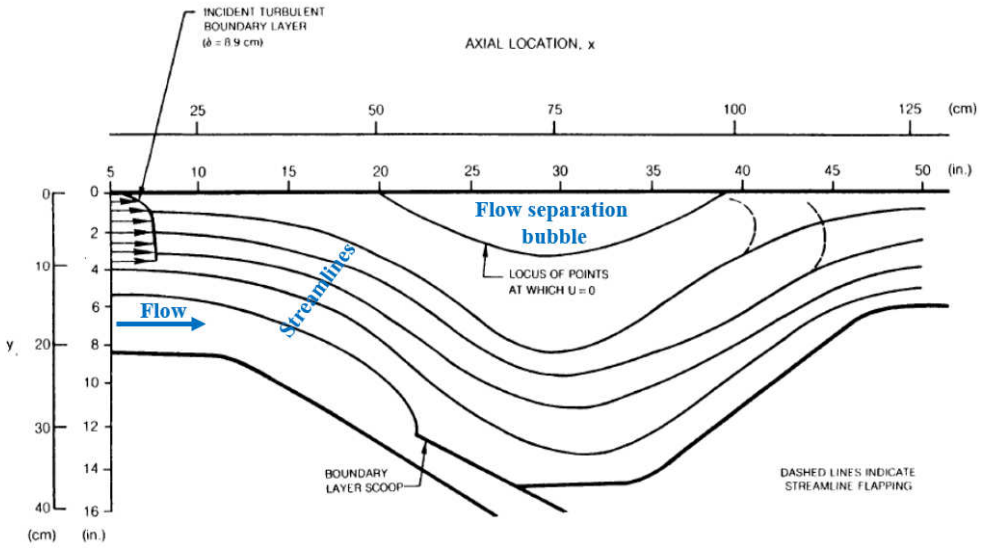

Figure 1.5: Schematic of flow streamlines and separation bubble. Adapted from Figure 4-6 in [31].

1.6. The depth of the wind tunnel is 4 feet, *which ensures a two-dimensional wall-bounded flow*. This facility produces a set of data over both curved surfaces (convex and concave) that locally causes flow deceleration and acceleration, respectively, for the “constant pressure" and “separating" flow cases. Similar to those done by Patrick [31], So and Mellor [41] also provided mean flow profiles and second-order turbulence statistics, which represent a good source of comparison against present RANS efforts. In [41], the following flow statistics were collected: (i) mean flow wall-normal profiles (U and V), wall static mean pressure coefficients (C_p), skin friction coefficients (C_f), Reynolds normal stresses (u'^2, v'^2, and w'^2), as well as Reynolds shear stresses ($u'v'$, $u'w'$, and $v'w'$) at several streamwise stations at the convex and concave wall.

The wind-tunnel analysis conducted by [41] exhibits the following numerical challenges:

1. In incompressible flow, the presence of convex walls induces local APG (flow deceleration); therefore, incoming turbulent boundary layers are more prone to wall detachment. In [41], the prescribed wall convex curvature ratio was in the order of $\delta/R \approx 0.08$. Here, δ in the local boundary layer thickness and R in the local curvature radius.

2. On the contrary, the presence of concave surfaces generates local FPG (flow acceleration). In wind-tunnel experiments by [41], the prescribed wall concave curvature ratio was approxi-

mately $\delta/R \approx$ -0.13 (usually, concave curvatures are considered negative).

3. According to Simpson [35], absolute values of wall curvature ratios larger than 0.1 can be considered strong (i.e., $|\delta/R| > 0.1$); thus, the wall curvatures prescribed by [41] can be assumed moderately strong and very strong, respectively.

4. The prescription of complex geometries (convex and concave surface curvatures) and their corresponding cell distribution in the computational mesh are non-trivial tasks in OpenFOAM [4].

5. The range of the momentum thickness Reynolds number ($Re_\theta \approx 2,100 - 4,000$) in So & Mellor [41] is roughly one order of magnitude lower than that of Patrick [31]. However, it still represents an authentic numerical challenge for the RANS approach.

Readers are referred to Appendix A for further information regarding the experimental setup in [41].

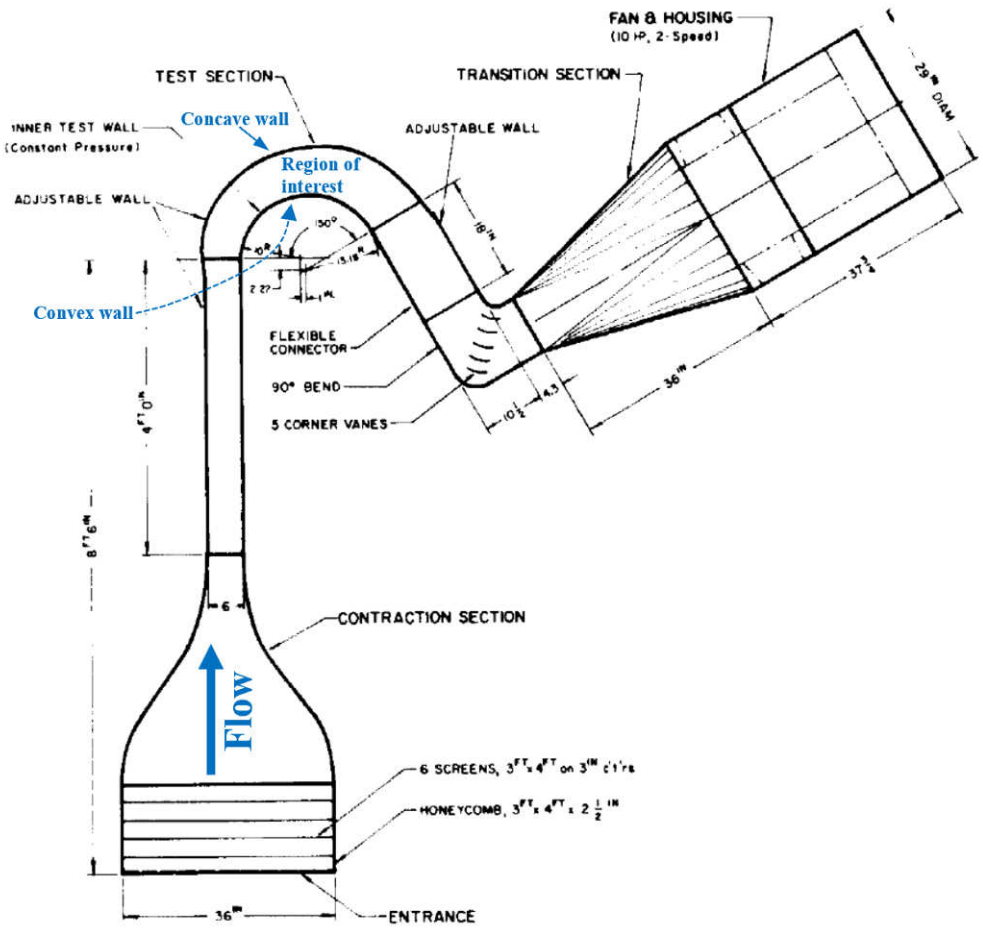

Figure 1.6: Schematic of the curved wall wind-tunnel. Adapted from Figure 1 in [41]. Images in original report of poor quality.

1.5 Intellectual Merit and Research Gap to be Filled

The proposed aims in the present MSc thesis will shed important light on the “gray zones" of detached spatially-developing turbulent boundary layers (SDTBL’s); perhaps, one of the most controversial and not well-understood issue in turbulence. Additionally, the effect of adverse pressure gradient on SDTBL under the combined influence of wall curvature (convex and concave) is also performed.

While the principal purpose of the present study is to “push the boundaries" of two popular turbulence models (i.e., the $k-\omega$ Shear Stress Transport and the Spalart-Allmaras models) in extreme external conditions (i.e., at very high Reynolds numbers, massively separated flow and strong wall

curvatures), a crucial intellectual merit of the present analysis is the prediction of passive scalars under such level of distortion in SDTBL's. Two wind-tunnel experimental setups [31, 41] from the literature are replicated and modeled via a RANS approach. The available experimental data is employed for validation purposes. It is worth mentioning that the diffusion and advection of passive scalars were not measured in previously mentioned experiments, but that the linear problem was numerically resolved in the present study via a transport equation for passive scalars and the consideration of a closure model for the turbulent passive scalar fluxes. Turbulent fluid mixing plays a key role in several engineering applications such as fuel injection, heat transfer, and pollutant dispersion, to name a few.

CHAPTER 2: LITERATURE REVIEW

In this chapter, relevant background is shown and discussed. The chapter is organized as follows:

- Background Literature
- Relevant Studies

2.1 Background Literature

2.1.1 Turbulence Models

Chapter 1 contains a summary of the turbulence models' equations, and thus this section is concerned with the implementation of the turbulence models.

Spalart-Allmaras Model

The SA model is a single equation model, and thus there is only one variable, ν_t or $\tilde{\nu}$, that determines the turbulence conditions. These two variables are linked via Equation 2.1, where f_{v1} is determined by Equation 2.2 and 2.3 [42].

$$\nu_t = f_{v1}\tilde{\nu} \tag{2.1}$$

$$f_{v1} = \frac{\chi^3}{\chi^3 + c_{v1}^3} \tag{2.2}$$

$$\chi = \frac{\tilde{\nu}}{\nu} \tag{2.3}$$

Spalart and Rumsey note that for the freestream, or as they refer to it, ambient, values of ν_t and $\tilde{\nu}$ should be held in relation to ν to certain ratios. Values of $\tilde{\nu}/\nu$, or χ, much less than unity, they point out, result in the model being unable to produce turbulent development. This ratio should be between 1 and 3 to produce a proper turbulent development. Spalart and Rumsey point out that

values above 3 will detrimentally change the behavior of the boundary layer. Finally, they point out that values for ν_t outside the boundary layer need to be less than those in the boundary layer's outer region [43]. Spalart and Allmaras demonstrate a better consistency to the experimental data on an RAE 2822 airfoil than other experiments do. However, Spalart and Allmaras point out that for low Reynolds number flows, the model tends to overpredict shear and velocity profiles for a Samuel-Joubert flow [42]. This may be due to the conditions of the case that they used to compare the SA model to experimental data. Furthermore, $\tilde{\nu}$ does not have an inherent wall function in OpenFOAM, but ν_t has the nutkWallFunction, which allows for the calculation of turbulent viscosity from a wall value along the trend that ν_t should follow for a boundary layer [6].

k-omega SST Model

Menter provides suggested freestream values in the Appendix of the $k-\omega$ SST origination paper [26]. Menter recommends values for ω in the freestream, as can be seen in Equation 2.4, ν_t in the freestream, as in Equation 2.5, which leads to the freestream values for k, as in Equation 2.6 [26].

$$\omega_\infty = A\frac{U_\infty}{L},\ where\ A \in [1, 10] \tag{2.4}$$

$$\nu_{t,\infty} = 10^{-B}\nu_\infty,\ where\ B \in [2, 5] \tag{2.5}$$

$$k_\infty = \nu_{t,\infty}\omega_\infty \tag{2.6}$$

Additionally, Menter provides a condition for ω near the wall, seen in Equation 2.7 [26]. This differs from Wilcox's formulation for ω near the wall, where Wilcox prescribes $C = 1$ [46].

$$\omega = C\frac{6\nu}{\beta_1 \Delta y_1^2},\ at\ y = 0,\ where\ C = 10 \tag{2.7}$$

Menter demonstrates that the $k-\omega$ SST model matches experimental data better than the

original $k-\omega$ model or even the $k-\epsilon$ model. There are a few weaknesses or deviations that would be worth pointing out before proceeding with this study. The $k-\omega$ model tends to underpredict skin friction coefficient, C_f, in certain APG regimes, as Menter demonstrates with flow along a cylinder wall and a backward-facing step. Additionally, the model underpredicts the velocity profile in the outer region of the boundary layers for the cylinder, backward-facing step, and NACA airfoil test cases. However, the $k-\omega$ SST model outperforms its predecessors and appears to have good agreement with experimental data [26]. This is only pointed out to inform the data in this study.

The CFD analyses will use the wall function for ν_t for the $k-\omega$ cases as the SA cases. However, there are two more scalars to consider near the wall. Turbulent kinetic energy, k, has two main wall functions, the *kqRWallFunction* and the *kLowReWallFunction*. The *kLowReWallFunction* artificially generates a k profile based on the distance from the wall. However, the *kqRWallFunction* creates a zero-gradient condition starting from a defined value. The specific dissipation, ω, has the *omegaWallFunction*, which produces the profile for ω from Wilcox's wall profile from [46] [6].

2.1.2 Turbulent Boundary Layer Theory

Flow Profiles

As previously mentioned in the review of the Spalart-Allmaras model, turbulent behavior has self-similar behaviors that occur regardless of scales. If one were to take the distribution of the wavenumbers relative to the energy that they contain, there is a clear trend of breakdown in energy from the lower to higher wavenumbers that follows a standard slope across all boundary layer [32]. This indicates a fractal behavior, which means that there are trends that exist across all scales independent of those scales [22]. To do this, the streamwise velocity and height from boundary layer can be non-dimensionalized into "wall units" via Equations 2.8 and 2.9, respectively. When working with boundary layers, this takes the form of the Log Law of the Wall, expressed by Coles in [14], seen in Equation 2.10, and a expression for the inner layer in Equation 2.11 [13].

$$u^+ = \frac{u}{u_\tau} \tag{2.8}$$

$$y^+ = \frac{yu_\tau}{\nu} \tag{2.9}$$

$$u^+ = \frac{1}{\kappa} ln(y^+) + C,\ where\, \kappa = 0.41\ and\, C = 5.0 \tag{2.10}$$

$$u^+ = y^+ \tag{2.11}$$

Pope compiled a number of papers that argue for a Reynolds-number dependent Law of the Wall, which can be more relevant for a wider range of condition. This does not violate the self-similarity principal. This idea comes from pipe flow boundary layers, and rather than going into detail, the formulation is shown in Equations 2.12, 2.13, 2.14, and 2.15. Rather than going in depth on this formulation, one can simply point out that based on the data Pope presents, as the Reynolds number approaches zero, these laws approach the original Log Law of the Wall.

$$u^+ = f_I(y^+) \tag{2.12}$$

$$\frac{U_\infty - \overline{u}}{u_0} = F_0(\eta) \tag{2.13}$$

$$u^+ = \frac{1}{\kappa} ln(y^+) + B \tag{2.14}$$

$$u^+ = C(y^+)^\alpha \tag{2.15}$$

There is also an extension that takes into account the wake formation at the edge of the boundary layer called the Velocity-Defect Law. In addition to the Log Law of the wall, there is a second function that considers the wake of the boundary layer, called the Law of the Wake, which is a function of y/δ [32]. Coles formulates this law as in Equations 2.16 and 2.17. Here, Π is a

non-dimensional constant for a boundary layer called "wake strength parameter".

$$\frac{\overline{u}}{u_\tau} = f_w\left(\frac{y}{\delta_v}\right) + \frac{\Pi}{\kappa} w\left(\frac{y}{\delta}\right) \tag{2.16}$$

$$w\left(\frac{y}{\delta}\right) = 2sin^2\left(\frac{\pi}{2}\frac{y}{\delta}\right) \tag{2.17}$$

Taking this idea further to develop a composite boundary layer velocity profile, Guarini et. al. [18] used a full composite profile for the boundary layer formulated in Equations 2.18 and 2.19 based on the Reichardt inner layer profile and Finley's wake function. For the conditions Guarini et. al. were studying, $C_1 = -(1/\kappa)ln(\kappa) + C$, $\eta_1 = 11$, $b = 0.33$, and $\Pi = 0.25$. It appears that C_1, η_1, and b are likely universal constants for the self-similar behavior of the boundary layers, whereas Π is dependent on the conditions of the flow [18]. It is also noteworthy that the cubic relation will be similar to the sine-function Coles originally used.

$$u^+ = \frac{1}{\kappa} ln(1 + \kappa y^+) + C_1\left(1 - e^{-y^+/\eta_1} - \left(\frac{y^+}{\eta_1}\right)e^{-by^+}\right) + \frac{1}{\kappa} w_G\left(\frac{y}{\delta}\right) \tag{2.18}$$

$$w_G\left(y'\right) = y'^2 - y'^3 + 6\Pi y'^2 - 4\Pi y'^3 \tag{2.19}$$

All these boundary layer relations are based on a ZPG condition. When APG conditions are present, there may be separation that results in regions of the boundary layer that have reversed flow, specifically closest to the wall. The outer region of the boundary layer will take a different shape, approaching a blend between the log layer and wake layer at an infinitely strong APG [45] [12]. The strength of the APG can be described by the Clauser factor, see Equation 2.34, and results in an intermittent backflow fraction by time, γ_{pu} change. For $\gamma_{pu} = 0.5$, there is an equal amount of backflow as forward flow in time for that point [35].

At the point of separation, Simpson [35] points out that the inner layer is no longer bound by the wall and disappears in a way. For the separation region, a new relation for $\gamma_{pu} \in (0, 0.5)$

describes the flow profile relative to the backflow behavior is in Equation 2.20. Simpson uses N to be the height where the maximum streamwise negative velocity, u_N, occurs, and $A = 0.3$. Once $y > 1.0N$, the outer region of the boundary layer behavior dominates. A viscous layer profile does appear and is described by Equation 2.21. Here, P_1 is a pressure gradient parameter that is analogous to a local Clauser parameter for the viscous region, defined in Equation 2.22.

$$\frac{\overline{u}}{|\overline{u}_N|} = A\left(\frac{y}{N} - ln\left|\frac{y}{N}\right| - 1\right) - 1,\ for\ y \in (0.2, 1.0)N \tag{2.20}$$

$$\frac{\overline{u}}{|\overline{u}_N|} = -C\frac{y}{N} + \frac{P_1}{2}\left(\frac{y}{N}\right)^2,\ for\ y \in [0, 0.2]N \tag{2.21}$$

$$P_1 = \frac{N^2}{\rho\nu|U_N|}\frac{dP}{dx} \tag{2.22}$$

Boundary Layer Sizes

In addition to the profile dimensions, an important measurement to the wall-bounded flow behavior are the thicknesses of the boundary layer, which is correlated to a number of things: the wake, pressure gradient quantification [45], momentum mixing length [45], and mean flow behavior.

The first and most basic definition of boundary layer is just where the ratio of velocity to freestream velocity meets a certain threshold, as in Equation 2.23. It seems like a common $threshold$ value is 99%, although there are studies that use other values [45].

$$\frac{\overline{U}}{U_\infty} = threshold,\ for\ y = \delta \tag{2.23}$$

The second definition of boundary layer is displacement boundary layer, which describes the height of where if the flow was uniformly the freestream value, would be blocked by the presence of a boundary layer. The definition is in Equation 2.24 from [45]. Sometimes authors use other notations for displacement thickness, so one should be careful to verify notations.

$$\delta^* = \int_0^\delta \left(1 - \frac{\overline{U}}{U_\infty}\right) dy \tag{2.24}$$

The third definition of boundary layer is the momentum boundary layer, which describes the height of where if the flow was uniformly the freestream value, the flow would have the same momentum. The definition is in Equation 2.25 from [45]. Again, sometimes authors use other notations.

$$\theta = \int_0^\delta \frac{\overline{U}}{U_\infty}\left(1 - \frac{\overline{U}}{U_\infty}\right) dy \tag{2.25}$$

Since in this study, scalar transport is considered, it is also worth discussing thermal and enthalpy boundary layer, which can be extended to other passive scalars. Like with boundary layer thickness, thermal boundary layer is defined as Equation 2.26. For Prandtl numbers near or above unity ($Pr \gtrapprox 1$), the ratio of the thermal boundary layer to boundary layer height is about the Prandtl number [45].

$$\frac{\overline{T}}{T_e} = threshold,\ for\ y = \delta_T \tag{2.26}$$

However, temperature is not the scalar being transported, and thus this idea is extended to the actual scalar, energy or enthalpy, that is transported through the flow. The boundary layer associated with this scalar, which represents the region that is the wall enthalpy if the flow is the freestream enthalpy uniformly. The formulation is in Equation 2.27 from [45].

$$\delta_h = \int_0^{\delta_T} \frac{T - T_e}{T_w - T_e}\frac{\overline{U}}{U_\infty} dy \tag{2.27}$$

Boundary Layer Development

This study is focusing on STDBL's, and thus the boundary layer heights and profiles and so on will change with the streamwise direction. To do this, White [45] outlines equilibrium velocity that follows a given power law, $U_e = Cx^m$, allowing for a developing boundary layer. Based on

this definition, $m = 0$ for uniform freestream conditions. This leads to the von Karman momentum relation for a boundary layer, which simply allows for the development and dissipation of momentum in that boundary layer, seen in Equation 2.28 [45].

$$\frac{d\theta}{dx} + (2 + H)\frac{\theta}{U_e}\frac{dU_e}{dx} = \frac{C_f}{2} = \frac{u_\tau}{U_e} \tag{2.28}$$

Additionally, there is a parameter, β, called the Clauser parameter that relates the pressure gradient to the acceleration of the flow, seen in Equation 2.29 [45]. This indicates some

$$\beta = \frac{\delta^*}{\tau_w}\frac{dP_e}{dx} = -\lambda^2 H\frac{\theta}{U_e}\frac{dU_e}{dx},\ where\ \lambda = \sqrt{\frac{C_f}{2}} = \frac{u_\tau}{U_e} \tag{2.29}$$

One of the parameters that is used up to this point is skin friction coefficient, C_f, defined in Equation 2.30 [45], which is helpful to describe the momentum dissipation from the boundary layer. This definition is not helpful for conditions where density, ρ, is not known like the OpenFOAM analyses in this study, and thus, the alternative formulation is more useful, as in Equation 2.31.

$$C_f = \frac{\tau_w}{\frac{1}{2}\rho U_e^2} \tag{2.30}$$

$$C_f = 2\nu\frac{\frac{du}{dy}|_w}{U_e^2} \tag{2.31}$$

Finally, the shear velocity, u_τ, helps define the self-similar shape of the boundary layer and allows for non-dimensionalizing the boundary layer for its shear behavior. Shear velocity is not a physical quantity and just describes the shear at the wall. Equation 2.32 shows the definition from [32]. Now, this definition does imply that shear velocity is always positive, which is not useful for reversed flow. Thus, this study uses the alternative definition to allow for better use of the parameter for the conditions expected, as in Equation 2.33.

$$u_\tau = \sqrt{\frac{\tau_w}{\rho}} \tag{2.32}$$

$$u_\tau = \frac{\tau_w}{||\tau_w||}\sqrt{\frac{\tau_w}{\rho}} \tag{2.33}$$

Note, for values of $threshold$ near unity (1), $U_e = U_\infty$.

2.2 Relevant Studies

Patrick's review of the literature [31] and foundation of the methods are based on the data produced by Simpson [36, 37]. Simpson provides a variety of data that gives insight to how turbulent boundary layers separate, like Patrick. Much of Simpson's data is dedicated to time-based turbulent flow statistics, and is thus not helpful for steady-state RANS simulation. However, as referenced in 2.1.2, Simpson had a later paper that described a better profile for flow with backflow [35].

In Paeres *et. al.* [29], an incoming incompressible SDTBL over a 2-D curved hill was numerically studied via the RANS equations plus two eddy-viscosity models: the $k-\omega$ SST and the Spalart-Allmaras turbulence models plus the consideration of passive scalar transport. The complex geometry with a combined strong adverse/favorable streamline curvature-driven pressure gradient caused by concave/convex surface curvatures was replicated from wind-tunnel experiments by Baskaran *et al.* [10]. It was concluded that the Reynolds analogy, defined by the $S_t/(C_f/2)$ ratio, was satisfied in zero-pressure gradient (ZPG) regions. On the contrary, the presence of streamline curvature-driven pressure gradient caused Reynolds analogy breakdown. Both models were able to reasonably capture very strong APG-induced outer secondary peaks in the Reynolds shear stresses $< u'v' >$ and turbulence production, as well as the negative slope on the constant shear layer. The presence of outer secondary peaks on $< u'v' >$ and u' was also detected by [8] in DNS of SDTBL subject to strong streamwise APG. According to DNS studies by Skote *et al.* [39], outer turbulent streaks are enhanced by APG which intensify streamwise velocity fluctuations and Reynolds shear stresses.

In a similar vein, Sanmiguel Vila et al. [17] studies the effects of the strength of an Adverse Pressure Gradient (APG) relative to the effects on the flow. Their description of strength uses an apt non-dimensional value called the Clauser factor [12] to compare self-similar boundary layer behavior, defined in 2.34. Sanmiguel Vila covers a range of of Clauser factors from 0.41 to 2.38 over a range of Reynolds numbers that were controlled by the freestream velocity. Sanmiguel Vila also provides some more resolution in a more limited range of conditions, but for a similar geometry as the Patrick study with a combination of LES and PIV [16]. There are a few key takeaways from Sanmiguel Vila's study to inform this one. First, the strength of the APG, quantified through the Clauser factor, affects the shape and shape factor of the boundary layer, increasing the shape factor with the Clauser factor. Second, while the distribution of Reynolds stresses is very similar across different strengths of the APG in the inner regions of the boundary layer, the distribution of Reynolds stresses in the outer region of the boundary layer is greatly affected by the strength of the APG. Stronger APG's will form a more prominent secondary peak of Reynolds stresses nearer to the edge of the boundary layer [17].

$$\beta = \frac{\delta^*}{\tau_w}\frac{dP}{dx} \tag{2.34}$$

Clauser [12] notes similar trends, but also notes some other points. First, the skin friction coefficient relative to the momentum thickness boundary layer decreases with increasing strength of APG until the skin friction relation reaches zero.

Similar to Patrick's study, Marusic and Perry [25] looks at the behaviors of APG boundary layers over a flat plate with a separating mechanism opposite the plate. This study contains much stronger APGs than the other studies, with Clauser factors reaching as high as 15.3 at low Reynolds numbers. This does, however, provide a good overview of how the APG will affect the turbulent behavior. Marusic and Perry provide both plotted and tabulated data that can correlate to a flat plate boundary layer in an adverse pressure gradient. One additional set of data that Marusic and Perry use is the Coles factor, which is used to modify the law-of-the-wall profile of the boundary layers to account for additional behaviors like the adverse pressure gradients [24]. In the Marusic

and Perry study, the best data is the distribution of Reynolds stress as the boundary layer separates, and shows that stronger Clauser parameters result in stronger Reynolds stress peaks in the outer region of the boundary layer [25]. This appears to be unaffected by local eddies in the flow.

CHAPTER 3: METHODS

The purpose of this chapter is to provide information regarding the employed computational resources, and software (flow solver, numerical schemes and postprocessing tools). It also discussed the strategies for setting proper turbulent inflow and boundary conditions in SDTBL's.

3.1 Computing Systems

Three computer systems produced CFD models in this study.

- **Home Ubuntu System:** This computer is an older desktop with Ubuntu 24.04 installed that is using a i7-3770 with 32GB of RAM. This computer was sufficient for building and iterating on smaller models rapidly before exporting to the larger HPC clusters.
- **UTSA ARC:** UTSA's Research Computing Support Group (RCSG) maintains computing nodes of various architectures [2]. This study used the following partitions:
  - compute1: This system allocates Intel Cascade Lake nodes with 40 cores and 80 threads with 384 GB of RAM.
  - compute2: This system allocates Intel Cascade Lake nodes with 40 cores and 80 threads with 384 GB of RAM. Unlike compute1, this partition's nodes can be containerized or have virtual machines placed on a node to only used the number of threads required to perform the job.
  - bigmem: This system allocates Intel Cascade Lake nodes with 80 cores and 160 threads with 1.5 TB of RAM.
- **UT Austin TACC Lonestar 6:** UT Austin's Texas Advanced Computing Center operates the Lonestar 6 system that is meant for research [3]. On this system, this study used the following partitions:

- vm-small: This partition allows a user to use one quarter (1/4th) of an AMD EPYC 7763 64-core processor with 32GB of RAM. Users can use up to one virtual node at a much lower cost than the normal partition, about 1/7th the price.
- normal: This partition contains two (2x) sockets of AMD EPYC 7763 64-core processors with 256GB of RAM, which provides a total of 128 threads on one node. A user can use up to 64 nodes. Note that the user pays for a whole node at any given time, so it is recommended that the user uses the whole thing. Additionally, the queues tend to be long, reaching up to a day and a half regularly.
- development: This partition allows more rapid use of the same node architecture of the normal partition, but users can only use up to 4 nodes for up to 2 hours, thus better for iteration and operations that require large computational resources for a short time.

3.2 CFD Software

OpenFOAM is an open-source CFD software that is installed on various computer systems [4]. At its core, it is a partial differential equation (PDE) solver that can be built and modified at will, but primarily gets applied for CFD.

Computer System	OpenFOAM Version
Home Ubuntu System	OpenFOAM 11
UTSA ARC	OpenFOAM v2406
UT Austin TACC Lonestar 6	OpenFOAM 12

Table 3.1: OpenFOAM Versions Used on the Computing Systems

Using OpenFOAM has a few considerations outside of the details pertaining uniquely to a CFD analysis. The primary one discovered during the project is the effect of splitting a CFD analysis amongst MPI ranks. On one hand, splitting the CFD case amongst too few ranks results in a slow solve that may not fit within a reasonable time for producing results. On the other hand, splitting the CFD case amongst too many ranks results in a few issues. The primary issue is that too few points or cells in a rank can result in instabilities for some solver conditions. Additionally, it

results in a lower efficiency, using excessive computational resources and spending too much time on serial portions of the solver. A short study on splitting CFD analysis amongst MPI ranks exists in Appendix B.

3.3 Auxiliary Software - Anser

There are a host of functions, programs, and such that OpenFOAM has to make the CFD software more usable. However, not all of the methods are readily documented, and thus during this project a Python software called Anser [1], Latin for goose. Like geese, there are lots of smaller software and objects that function together, using each other's capabilities to ease the workload of any one piece.

3.4 CFD Analyses

There are three analyses to assess the geometries, models, and behaviors that this study is interested in. They are:

- **Inlet Duct**: This analysis studies the development of a boundary layer along one side of the inlet duct for the Patrick study that the current study is replicating. This provides a few things.
    1. Testing the turbulence models along a flat and assumed smooth surface will allow for an immediate verification of the CFD code according to canonical data.
    2. The developing boundary layer can then be synthesized as an inlet condition for the test sections for each of the replicated CFD analyses.
    3. Testing the operational capability of OpenFOAM on smaller analyses like the inlet ducts allows for learning how to best utilize the software before moving to larger, more expensive analyses.
- **Patrick Test Section**: This analysis studies the separation of a boundary layer over a flat plate to the best faithful representation of Patrick's 1987 experiment [31]. Additionally, it investigates passive scalar transport to understand the physics in the same context.

- **So and Mellor Test Section**: This analysis studies the separation of a boundary layer over a curved surface to the best faithful representation of So and Mellor's 1972 experiment [41]. In this cases, there is no necessary inlet flow as the inlet to the So and Mellor geometry can be assumed uniform profile with a natural development of the boundary layer.

To produce the proper viscous model, all viscosity is assumed Newtonion, i.e. constant. The value for the viscosity is calculated by CoolProp, a free thermodynamic state software, using the default Helmholtz equation of state [11]. Adding scalar transport into the analysis is done through introducing a user-defined function that targets the built-in Shared Object (*.so) OpenFOAM has for passive scalar transport outside of the main CFD solve. It is worth noting that the pressure is set to be a zero-gradient condition (zeroGradient) at the walls. As is seen in the results, this likely causes issues with the pressure distribution in the domain, but OpenFOAM does not provide an adequate alternative as of the time of authorship. An interesting extension of this project would include a custom boundary condition for the wall-normal pressure gradient that is dependent on the wall-normal Laplacian viscous behavior instead of a zeroGradient condition. Additionally, even though the CFD analysis uses the SIMPLE algorithm, a time step is required for its pseudo-steady solve. The time step was calculated for an equivalent CFL of 1, or whatever round number just below that. This was left in instead of time step sizes of 1 so that others could more easily modify these cases to be transient conditions for later use.

3.4.1 Inlet Duct Analysis

Free Development Inlet Duct

Patrick describes the inlet duct as a duct with a 0.63cmx0.63cm trip bar. The purpose appears to be to control the boundary layer as it enters the test section to create a controlled inlet condition for a measurable and repeatable experiment. In the context of this study, software can synthesize an extended inlet section to find where in the natural development of the boundary layer provides the conditions that Patrick measured in the 1987 experiment. Rather than including the trip bar, which would create a complex mesh, the boundary layer develops naturally, and the desired location to

recycle the profile from will be found to match Patrick's prescribed inlet conditions. Additionally, the length is increased to $100\delta_{ref}$ from $32.8\delta_{ref}$, where Patrick's measured boundary layer thickness is δ_{ref}. One may notice that the opposing wall is a slip wall, and thus has zero boundary layer height. This will have minimal effect on the fidelity of the simulation. Patrick's duct length of $2.47m$ results in a displacement boundary layer height of $2.09mm$ according to the Blausius solution [45], which only changes the effective flow area of 1.07%, which should have minimal effect on the flow profile for a low-turbulence freestream condition. There is more uncertainty that comes from some combination of the models and the experimental data. Additionally, the behavior will deviate from a true flat plate some with the duct behavior. The calculated freestream velocity for Patrick's measured displacement boundary layer height is $28.1m/s$, from $27.0m/s$, resulting in a 4.09% acceleration of flow.

Figure 3.1: Illustration of Inlet Duct Domain. Not to scale. Top surface is developing boundary layer shear surface with inlet slip surface.

Boundary	Velocity	Pressure	ν_t	Turbulence Scalar	Turbulence Dissipation
Inlet	Fixed Value	Zero Gradient	Calculated Value	Uniform Value	Zero Gradient
Outlet	Zero Gradient	Fixed Value - Value 0	Zero Gradient	Zero Gradient	Zero Gradient
Leading Wall	Slip	Zero Gradient	Wall Function - Value 0	Wall Function - Value 0	Wall Function - Calculated Value
Flat Plate	No Slip	Zero Gradient	Wall Function - Value 0	Wall Function - Value 0	Wall Function - Calculated Value
Opposing Wall	Slip	Zero Gradient	Wall Function - Value 0	Wall Function - Value 0	Wall Function - Calculated Value

Table 3.2: Patrick Inlet Duct Boundary Conditions

Figure 3.1 shows the set up for the CFD on the inlet duct. There is only one surface that has shear, the top no-slip wall. The boundary layer develops along this surface. There is a preceding slip wall to extend the domain 100 elements to allow a region for the CFD analysis to resolve plug-to-shear changes. Additionally, the opposing wall to the shear wall is a no-slip wall to allow for no development of a boundary layer, described in more detail in Table 3.2 as this will be absorbed by the scoop early in the test section, and thus more calculation than would be returned in results. In Table 3.2, the Turbulence Scalar can be either $\tilde{\nu}$ or turbulent kinetic energy, k, for the Spalart-Allmaras or $k-\omega$ SST turbulence model, respectively. The dissipation in this case only pertains to the $k-\omega$ SST turbulence model as specific dissipation, ω. For the flat plate and opposing walls, the plate will dissipate the turbulence, but the leading wall avoids dissipation to preserve the inlet turbulence conditions up to the flat plate.

At the inlet, the turbulent kinetic energy is calculated from the expected turbulence intensity, which Patrick measured to be 0.25% at the inlet of inlet duct [31] and calculated via a Root Mean Square (RMS) estimate, seen in equation 3.1.

$$k = \frac{3}{2}(IU_{\text{inf}})^2 \tag{3.1}$$

At the inlet, ω, or specific dissipation is zero-gradient, and allowed to float according to the model itself. To provide an initialization for the interior of the domain, the conditions of a freestream corresponding to the turbulence intensity are calculated via the formula that Menter suggests in [26], seen in equation 3.2 where L is the characteristic length of the domain. However, this did result in an initial dissipation much higher than the steady-state values. Wilcox, on the other hand offers a similar calculation with a different coefficient [46], seen in equation 3.3. From some experimentation, a much better value is roughly 1.3 rather than 10 or 1 from Menter and Wilcox, respectively.

$$\omega = 10U_{inf}/L \tag{3.2}$$

$$\omega = 1U_{inf}/L \tag{3.3}$$

The $k - \omega$ model produces a value of turbulent viscosity without requiring SST due to a zero pressure gradient condition at the inlet, simply calculated by Equation 3.4. The CFD naturally calculates this from the boundary condition and turbulence model.

$$\nu_t = \frac{k}{\omega} \tag{3.4}$$

For the Spalart-Allmaras model, the turbulent viscosity comes from this calculation, and the modified viscosity comes from the simple definition of this modified viscosity, seen in Equation 3.5. In this case, the value for χ converged to about 1.86, which seems within the range that Spalart and Rumsey would suggest is a good turbulently quiet freestream in [43].

$$\nu_t = \tilde{\nu} f_{v1} \tag{3.5}$$

In the same vein for calculating ω values, at the wall, Menter in [26] provides a calculation for the ω at the wall based on the first element size, seen in equation 3.6, where 0.075 is a constant of

the turbulence model, Δy_0 is the first element resolution, and 10 is the constant value selected by Menter to reportedly give more accurate results.

$$\omega = 10\frac{6\nu}{0.075\Delta y_0^2} \tag{3.6}$$

This provides the CFD with an initial value for ω near the wall, but the wall function will rapidly change the value to the proper one [6].

On the subject of wall functions, k is calculated via the kqRWallFunction, which allows for the resolution of the inner region of the boundary layer, unlike the kLowReWallFunction [6]. Additionally, the value of turbulent viscosity comes from the nutkWallFunction. Theoretically, one can use fixed values rather than wall functions, but it was found that this resulted in unstable solves, and thus the wall functions were left in to provide stability, with a need to validate the results.

With this setup, the OpenFOAM splits the domain across the specified threads to allow for parallel processing of the CFD, which provides faster computation, at the cost of some efficiency of those resources.

To solve the analysis, OpenFOAM is solving a steady state condition for the incompressibleFluid solver, which uses the SIMPLE algorithm, which originated from [21]. The finite volume schemes are:

1. **Gradient Scheme:** Gauss linear
2. **Divergence Schemes:** See Table 3.3.
3. **Laplacian Scheme:** Gauss linear corrected
4. **Interpolation Scheme:** Linear
5. **Surface Normal Gradient Schemes:** Corrected
6. **Wall Distance Calculation:** meshWave

Furthermore, the calculation will target the convergences, tolerances, and residuals in Table 3.3. These values provided for a steady-state solution that allowed for either a solution that continues to develop through the domain or provides the best solution the mesh can allow. During experimentation, it was found that the relaxation factors provide a high degree of influence on how converged the solution can become. The divergence scheme for the flat plate cases with the $k-\omega$ model did work for the linear upwind scheme, however, not so with the test sections. In the interest of using the flat plate analyses to assess the use of the turbulence models, the divergence schemes were kept consistent.

Flow Parameter	Divergence Scheme	Tolerance	Residual	Relaxation Factor
P		1e-6	1e-9	0.3
U	Gauss linear upwind ∇U	1e-6	1e-9	0.5
$\tilde{\nu}$	Gauss linear upwind ∇U	1e-6	1e-9	0.3
k	Gauss limited linear 1	1e-6	1e-9	0.3
ω	Gauss limited linear 1	1e-6	1e-9	0.3

Table 3.3: Patrick Inlet Duct Solve Settings

The analysis is repeated over three (3x) different mesh refinement levels, which are defined by their first cell off the wall height. Seen in Table 3.4, this is done by the wall height in wall coordinates relative to the reference boundary layer conditions Patrick measures at station 0.

Refinment	$\Delta y^+_{0,ref}$	$\Delta t\ [s]$
Coarse	1.00	$75e-6$
Medium	0.50	$37.5e-6$
Fine	0.33	$25e-6$

Table 3.4: Refinement Levels for Free Development Inlet Duct

Injected Boundary Layer Inlet Duct

This analysis is similar to the Free Development Inlet Duct, but instead of having a longer domain with a uniform inlet profile, Anser produces a synthetic boundary layer profile from canonical boundary layer trends and wall functions, and the domain is only $32.8\delta_{ref}$ long.

In the end, with some experimentation, this did not turn out to be a viable method since the

profile did not match exactly would it needed to be. More will be discussed in the results chapter.

3.4.2 Patrick Test Section

Patrick provides the coordinates for a streamline that is calculated to be two-dimensional projection of the surface that represents where no mass flux normal to that surface occurs. Given Patrick's short description of the curve, it is unclear what to do with these coordinates and the curve.

When the points are used to create a standard spline, as in Figure 3.2, the spline clearly does not line up with the geometry of the test section that is explicitly described by Patrick. After the scoop and prior to the exit duct, there are sections of the spline that are outside of the fluid region.

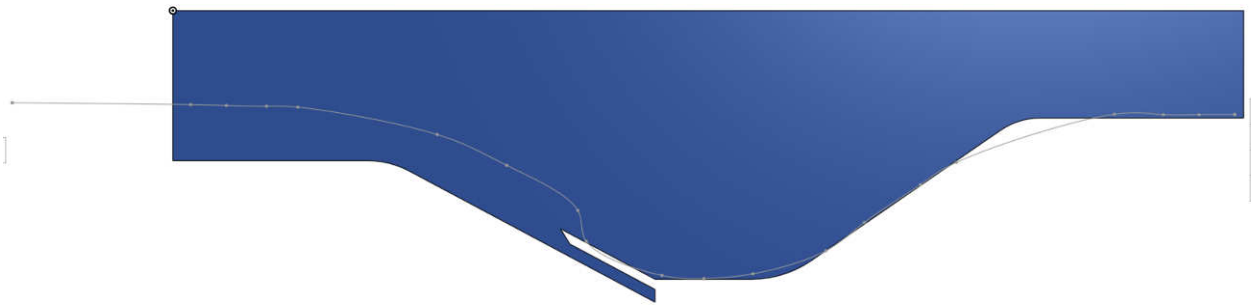

Figure 3.2: Spline Created from Zero Flux Coordinates Against Patrick Test Section Geometry

When the points are used to create a Bezier spline, as in Figure 3.3, where the points serve as end points for tangent lines, the spline is more reasonably matched to the test section geometry Patrick describes. There are some regions of negative or zero-thickness between the spline and the geometry's boundaries, but much closer. The main issue with this approach is that it does not capture the scooping of the flow from the region farther from the flat plate, including the stagnation effects.

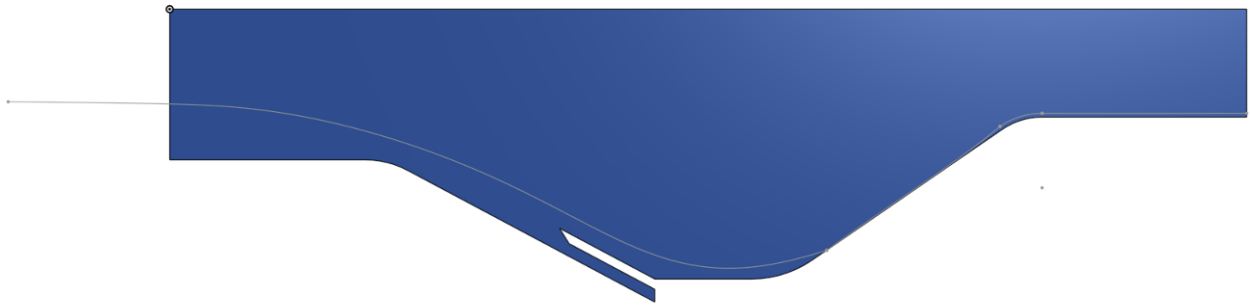

Figure 3.3: Bezier Spline Created from Zero Flux Coordinates Against Patrick Test Section Geometry

A compromise between the splines and the geometry places a series of curves and lines offset from the wall to capture the effects of a heavily favorable pressure gradient, seen in Figure 3.4. It will not be a direct comparison, but does provide what appears to be a similar surface to what Patrick illustrates by showing the streamlines that come from smoke injection.

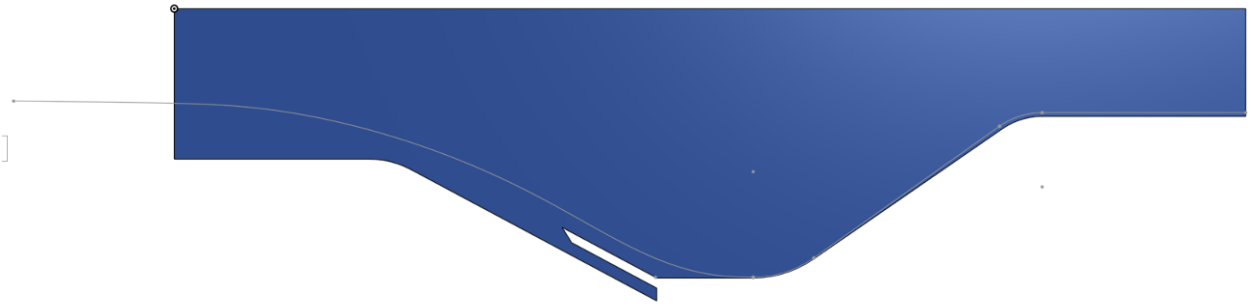

Figure 3.4: Synthetic Zero Flux Surface Against Patrick Test Section Geometry

Splitting the geometry up into blocks for OpenFOAM's blockMesh mesher, the resulting split compared to the test section geometry is in Figure 3.5.

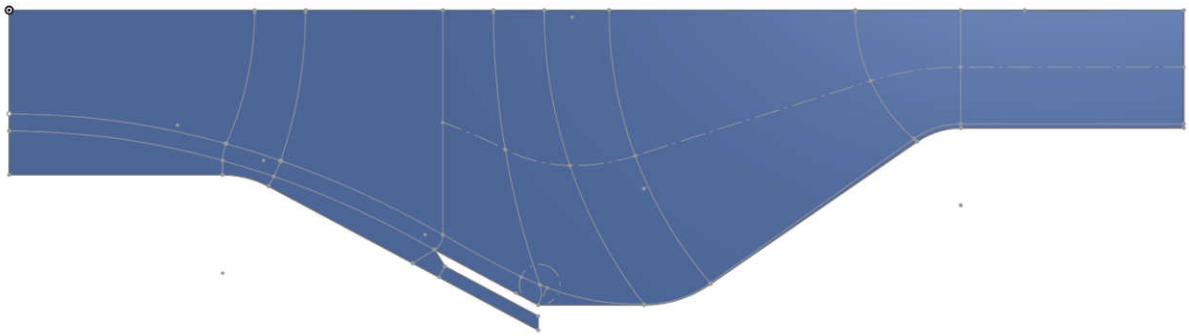

Figure 3.5: Blocks Based on Original Splines.

However, as the development progressed, the small blocks near the wall where the heavily FPG is present caused consistent floating point errors. Thus, the offset is equalized to allow for following the spline for the inlet region, but allowing for a more relaxed offset from the walls of the test section with strong FPG, reducing the floating point error risk. This new block set is in Figure 3.6.

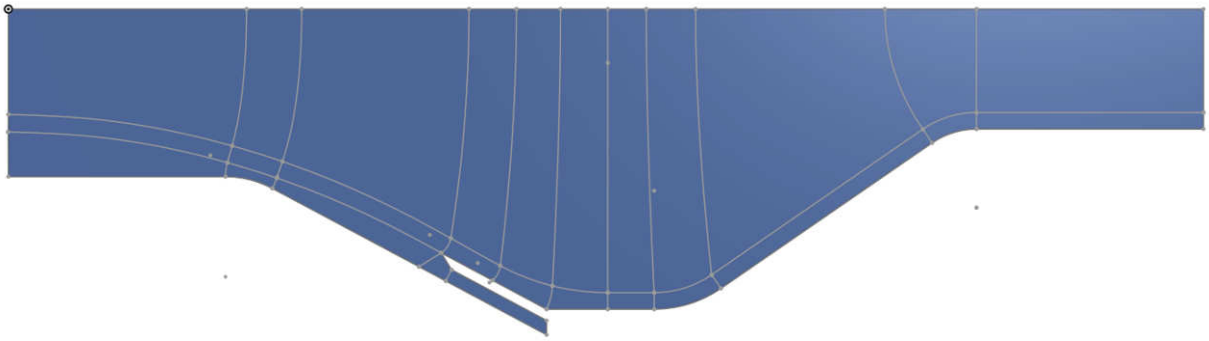

Figure 3.6: Blocks Based on Equalized Offsets.

The inlet conditions for this analysis come from the Inlet Duct Analyses. A vertical plane samples the profile that produces the closest profile to what Patrick reported.

To find the best vertical sampling plane, Anser takes a series of planes and calculates the following parameters to determine the best location:

1. Boundary layer height (δ)

2. Displacement boundary layer height (δ^*)

3. Momentum boundary layer height (θ)

4. Shape factor (H)

5. Skin friction coefficient (C_f)

6. Shear velocity (u_τ)

7. Unit length Reynolds number (Re/x)

8. Momentum thickness Reynolds number (Re_θ)

9. Shear velocity Reynolds number (Re_τ)

Anser takes these calculated values from the CFD and calculates the error relative to the reported conditions Patrick had at the inlet of the test section along the lines of Equation 3.7, where i is the index of the sampling plane. These errors are then normalized via Equation 3.8, where W_i is a weighting factor to take into account the error of the experiment and value to the calculation, to produce a net error for the plane.

$$\epsilon_i = \frac{\phi_{CFD,i}}{\phi_{PatrickInlet}} - 1 \tag{3.7}$$

$$\epsilon_{L2} = \frac{1}{N}\sqrt{\sum_{i=0}^{N} W_i \epsilon_i^2} \tag{3.8}$$

The location that Patrick provides for a flow profile is upstream of the inlet of the test section, at $24.1cm$ upstream of the test section inlet. The error calculation provides the best location of Patrick's profile measurement location. Given a viable boundary layer development, the flow will develop to the proper profile within that lead-in distance. Using this recycled boundary layer makes the inlet condition insensitive to issues with the boundary layer development that could propagate into this analysis since the inlet conditions are essentially forced to be what Patrick measured.

The outlet boundary is set to zero pressure to allow the whole simulation to be in gauge pressure. Additionally, this allows for easier calculation of the scoop outlet. Patrick specifically measures a difference in pressure (dP) between the outlet and the inlet plenum to the filters to be $22.9cmH_2O$, which comes to be about $2.24kPa$. This dP can be assumed valid from the outlet to the scoop outlet since there should be no significant dP between the scoop outlet and the inlet plenum of the filters. Since OpenFOAM uses a kinematic pressure, or P/ρ, the value for the pressure at the scoop outlet becomes $-1.83e3m^2/s^s$.

Only the flat plate is simulated as a no-slip condition in the CFD. It is expected that the opposing walls will not provide any significant contribution to the behavior within the duct other than dissipating some turbulence in the freestream. Thus, the boundary conditions in this analysis are as described in Table 3.5.

Boundary	Velocity	Pressure	ν_t	Turbulence Scalar	Turbulence Dissipation
Inlet	Recycled Profile	Zero Gradient	Recycled Profile	Recycled Profile	Zero Gradient
Outlet	Zero Gradient	Fixed Value - Value 0	Zero Gradient	Zero Gradient	Zero Gradient
Scoop Outlet	Zero Gradient	Fixed Value - Value -1.83e3	Zero Gradient	Zero Gradient	Zero Gradient
Flat Plate	No Slip	Zero Gradient	Wall Function - Value 0	Wall Function - Value 0	Wall Function - Calculated Value
Opposing Walls	Slip	Zero Gradient	Wall Function - Value 0	Wall Function - Value 0	Wall Function - Calculated Value

Table 3.5: Patrick Test Duct Boundary Conditions

The wall functions remain the same as used in the flat plate study, since the results chapters will show that these wall functions produce the correct results at least for a ZPG flat plate.

To solve the analysis, OpenFOAM is solving a steady state condition for the incompressibleFluid solver, which uses the SIMPLE algorithm, more is originated from [21]. The finite volume schemes are:

1. **Gradient Scheme:** Gauss linear

2. **Divergence Schemes:** See Table 3.6.

3. **Laplacian Scheme:** Gauss linear corrected

4. **Interpolation Scheme:** Linear

5. **Surface Normal Gradient Schemes:** Corrected

6. **Wall Distance Calculation:** meshWave

Furthermore, the calculation will target the convergences, tolerances, and residuals in Table 3.6. These values provided for a steady state solution that allowed for either a solution that continues to develop through the domain or provides the best solution the mesh can allow. During experimentation, it was found that the relaxation factors provide a high degree of influence of how converged the solution can become. The divergence schemes for the $k-\omega$ turbulence model were backed off of the second-order accurate Gauss linear upwind schemes for the more stable Gauss limited linear scheme due to instabilities that cropped up during the solve. The relaxation factors are already low

Flow Parameter	Divergence Scheme	Tolerance	Residual	Relaxation Factor
P		1e-6	1e-9	0.3
U	Gauss linear upwind ∇U	1e-6	1e-9	0.5
$\tilde{\nu}$	Gauss linear upwind ∇U	1e-6	1e-9	0.3
k	Gauss limited linear 1	1e-6	1e-9	0.3
ω	Gauss limited linear 1	1e-6	1e-9	0.3

Table 3.6: Patrick Test Duct Solve Settings

Like with the inlet ducts, there are three (3x) levels of refinement for the test section. However, there are a few differences. First, the resolution is the maximum off wall resolution, rather than the one at the inlet that corresponds to the inlet section analysis. Thus, the test section will inherently be finer than the inlet section analysis, but guarantees an acceptable resolution for the separation section. This will mean OpenFOAM will be doing some interpolation as it is recycling the inlet duct conditions to the test duct. Second, the refinement level steps have uniform increments of two

(2) to allow for a simpler convergence analysis. Third, this also means that the reference point is for a smaller boundary layer than the test section duct will experience. The refinement levels can be seen in Table 3.7.

Refinment	$\Delta y^+_{0,ref}$	$\Delta t\ [s]$
Coarse	1.00	$60e-6$
Medium	0.50	$50e-6$
Fine	0.25	$40e-6$

Table 3.7: Refinement Levels for Patrick Test Duct

3.4.3 So and Mellor Test

Unlike with the Patrick study, the So and Mellor study is best performed as a single section. This does produce a larger analysis, but given the natural development of the boundary layer in the study, the same natural development can be replicated in the CFD.

The geometry was taken from the measurements and scale drawings So and Mellor provide in Figure 3 from [41]. A simple tracing with dimensions produces the curves that represent the original test geometry comes from CAD software, and then the points are exported to BlockMesh. The comparison of the geometry is illustrated in Figure 3.7.

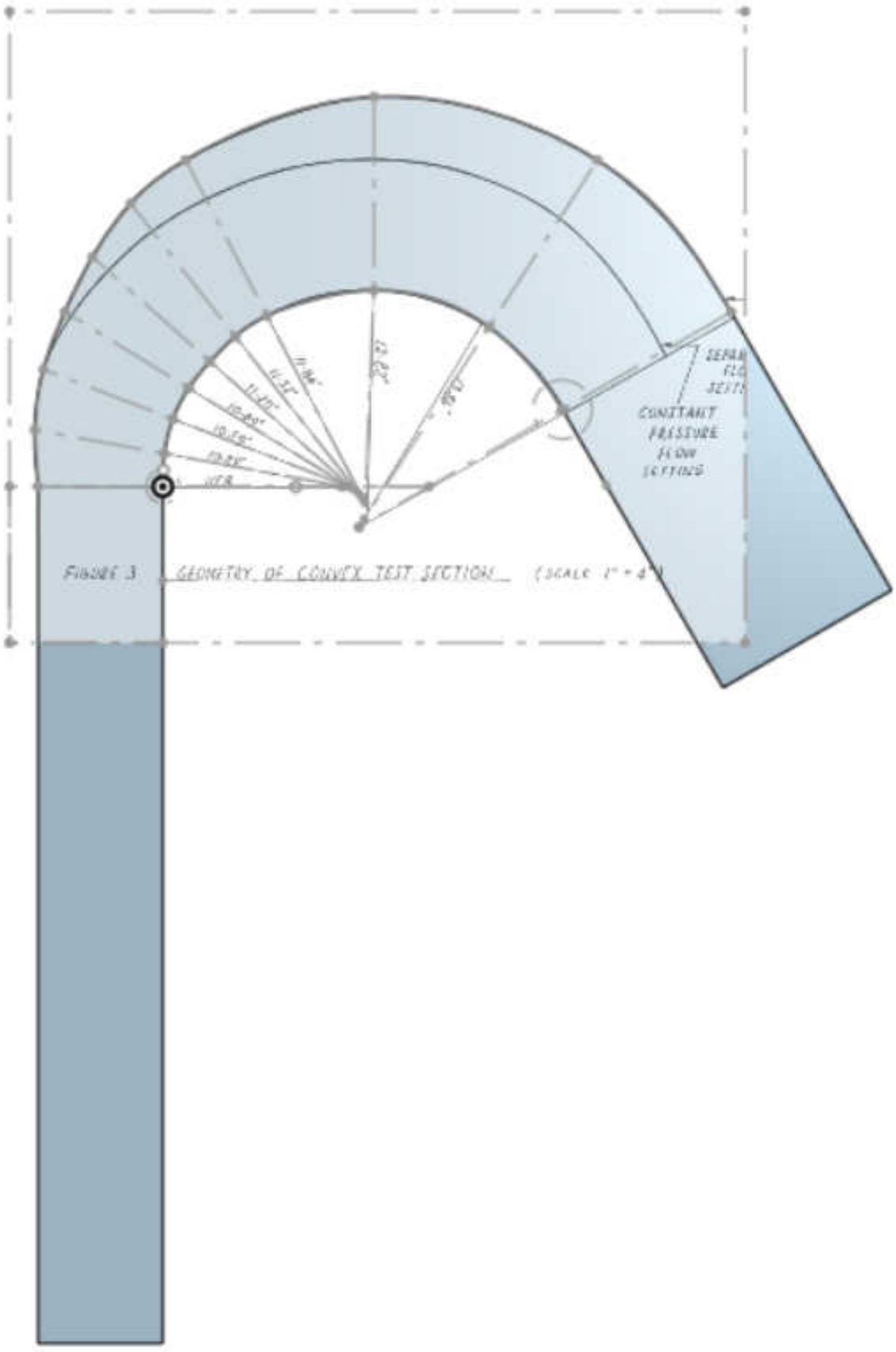

Figure 3.7: Comparison of Used Geometry and Reported Geometry from So and Mellor [41].

The inlet condition for the CFD is a uniform flow velocity since this is theoretically where the boundary layer begins as the flow is collimated coming into this section. So and Mellor provide a station downstream of the inlet, $24in$ from the inlet, where the measured freestream velocity is $70.3ft/s$. According to the Blausius solution for a laminar boundary layer development [45], the displacement boundary layer thickness is $1.14mm$. Based on having two (2x) identical boundary layers, this results in a uniform flow velocity of $21.7m/s$ at the inlet. This inlet should have minimal if any turbulence, but So and Mellor measured a turbulence intensity in the freestream at the first station of 0.5%, and is thus used at the inlet.

The outlet is a zero gradient for all values to allow the upstream effects to determine the outlet section flow. The pressure is set to zero here to allow for calculating gauge pressure from the outlet.

Based on the summation of the midstream arc length and the length of the inlet and outlet ducts, the length of the test section comes to be about $2.89m$, and thus provides a point to initialize the dissipation from using Menter's recommended value from Equation 3.2. Biasing towards the higher dissipation forces the analysis to dissipate dissipation rather than turbulence, which leads to a more stable solve.

All walls are no-slip in this analysis as all walls are expected to contribute to some turbulent behavior that the current study is interested in. The turbulence intensity at the walls will be zero, with k using the kqRWallFunction, ν_t using the nutkWallFunction, and ω using the omegaWallFunction with an initial value calculated from Equation 3.6. All the boundary conditions are described in Table 3.8.

Boundary	Velocity	Pressure	ν_t	Turbulence Scalar	Turbulence Dissipation
Inlet	Fixed Value	Zero Gradient	Calculated Value	Uniform Value	Zero Gradient
Outlet	Zero Gradient	Fixed Value - Value 0	Zero Gradient	Zero Gradient	Zero Gradient
Inlet Walls	No Slip	Zero Gradient	Wall Function - Value 0	Wall Function - Value 0	Wall Function - Calculated Value
Convex Walls	No Slip	Zero Gradient	Wall Function - Value 0	Wall Function - Value 0	Wall Function - Calculated Value
Concave Walls	No Slip	Zero Gradient	Wall Function - Value 0	Wall Function - Value 0	Wall Function - Calculated Value
Outlet Walls	No Slip	Zero Gradient	Wall Function - Value 0	Wall Function - Value 0	Wall Function - Calculated Value

Table 3.8: Patrick Test Duct Boundary Conditions

To solve the analysis, OpenFOAM is solving a steady state condition for the incompressible-Fluid solver, which uses the SIMPLE algorithm, more is originated from [21]. The finite volume schemes are:

1. **Gradient Scheme:** Gauss linear

2. **Divergence Schemes:** See Table 3.9.

3. **Laplacian Scheme:** Gauss linear corrected

4. **Interpolation Scheme:** Linear

5. **Surface Normal Gradient Schemes:** Corrected

6. **Wall Distance Calculation:** meshWave

Furthermore, the calculation will target the convergences, tolerances, and residuals in Table 3.9. These values provided for a steady state solution that allowed for either a solution that continues to develop through the domain or provides the best solution the mesh can allow. During

experimentation, it was found that the relaxation factors provide a high degree of influence of how converged the solution can become.

Flow Parameter	Divergence Scheme	Tolerance	Residual	Relaxation Factor
P		1e-6	1e-9	0.3
U	Gauss linear upwind ∇U	1e-6	1e-9	0.5
$\tilde{\nu}$	Gauss linear upwind ∇U	1e-6	1e-9	0.3
k	Gauss linear upwind ∇U	1e-6	1e-9	0.3
ω	Gauss linear upwind ∇U	1e-6	1e-9	0.3

Table 3.9: So and Mellor Duct Solve Settings

Like the other analyses, the So and Mellor test duct has three (3x) levels of refinement. The reference point is the first measurement point, which is halfway through the inlet straight section. This boundary layer is not nearly as developed as the one entering the curved section, as one would expect, and thus the mesh is going to be well-refined for these conditions. The refinement levels are described in Table 3.10.

Refinment	$\Delta y^+_{0,ref}$	$\Delta t\ [s]$
Coarse	1.00	$50e-6$
Medium	0.50	$25e-6$
Fine	0.25	$10e-6$

Table 3.10: Refinement Levels for So and Mellor Test Duct

3.4.4 Passive Scalar Transport

The passive scalar transport was set up to use Equation 3.9 as the diffusion. In the solution, $\alpha = 1.40$, which corresponds to $Pr = 0.714$, and $\alpha_t = 1.10$, which corresponds to $Pr_t = 0.909$.

$$\alpha_{eff} = \nu\alpha + \nu_t\alpha_t \tag{3.9}$$

OpenFOAM solves the scalar transport via a user function, which iterates after the velocity field is solved via the *incompressibleFluid* solver iterations. All walls are set to $T = 290$, and the inlet is set to $T = 300$, allowing an adiabatic temperature difference of $\Theta_{aw} = (T_\infty - T_{aw}) = 10$, which will make post-processing easier.

CHAPTER 4: FLAT PLATE RESULTS

4.1 Inlet Duct

The Inlet Duct analyses are led by six (6x) cases that are outlined in Table 4.1.

Refinement	SA Model Cases	$k-\omega$ SST Model Cases
Coarse	14	15
Medium	16	17
Fine	18	19

Table 4.1: Cases Used for the Free Development Flat Plate Analyses.

4.1.1 Residuals

Residuals are the difference in the field values vs the calculated values for the convergent solve, which allows for the study to have a sense of how well the problem was set up and an overview of where potential issues in the setup of the CFD analysis may be.

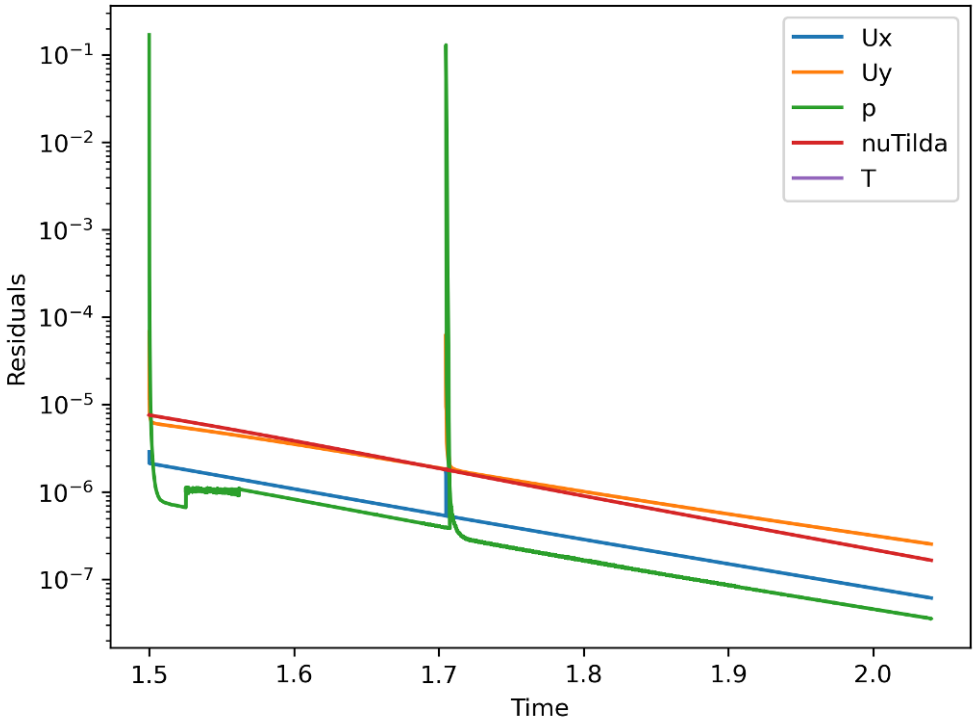

Figure 4.1: Residuals for Case 14

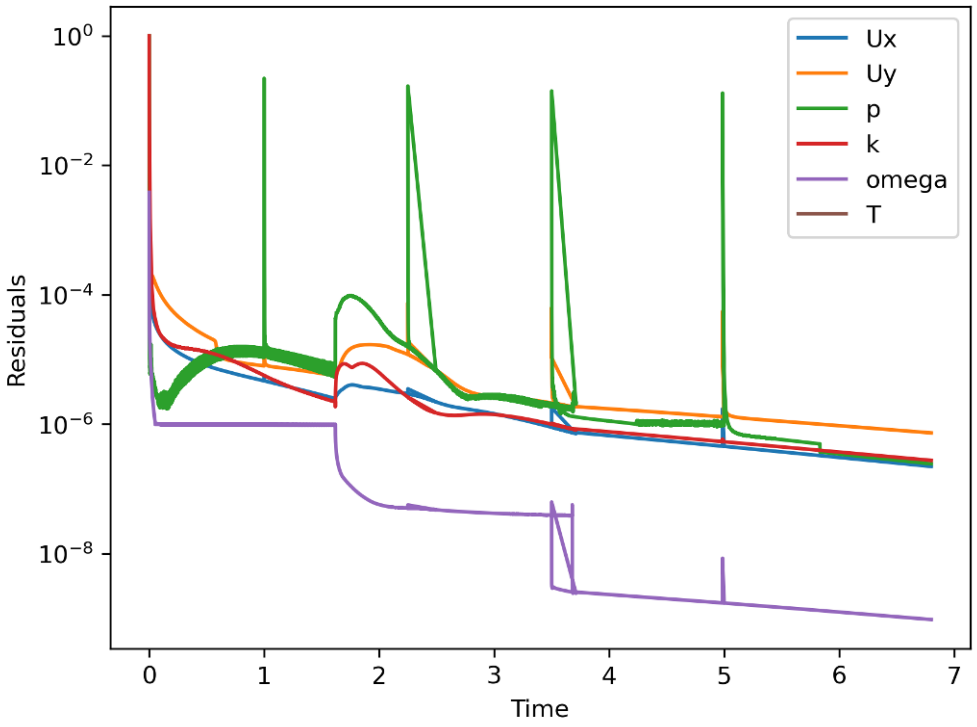

Figure 4.2: Residuals for Case 15

The residuals for the flat plate cases are displayed in Figure 4.1 and 4.2 for Case 14 and 15, respectively. The sharp peaks are caused by restarts, as the CFD solve is never completed in one session. In all cases, the residuals have come down to $1e-6$ at the end of the solve with the other values continuing to iterate, showing a well-set up analysis. In the specific case of Case 15, it is obvious where the minimum iteration control was set up, as ω stops flat-lining and continues to iterate. For these coarse cases, the problem looks well set up, although it does take a large amount of iterations to come to a solution for a residual of $1e-6$, $227e3$ and $226e3$ iterations for Case 14 and 15, respectively.

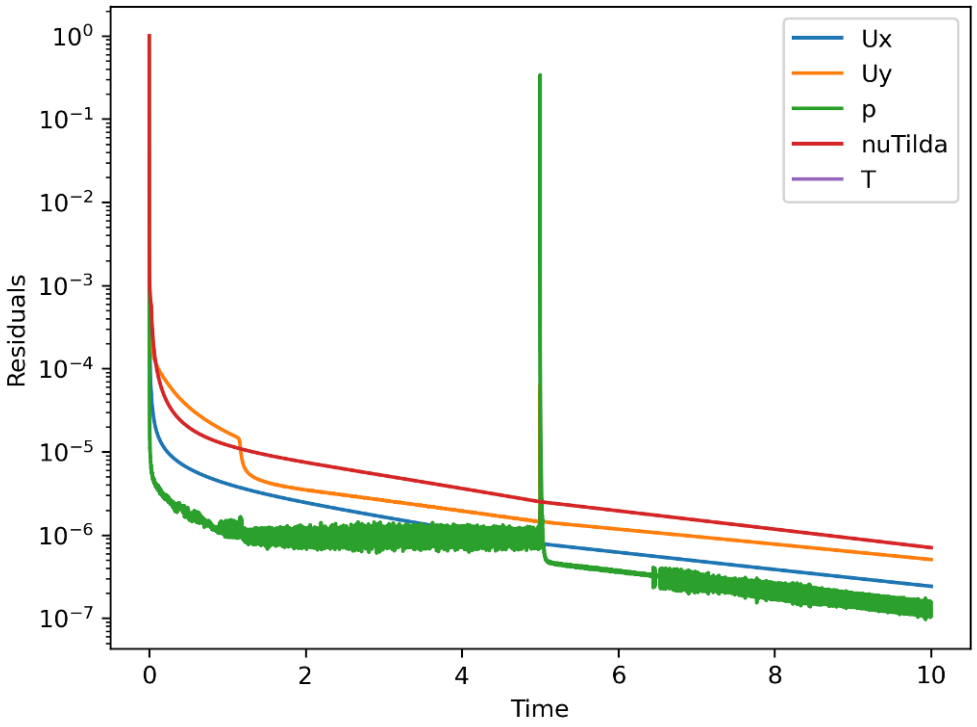

Figure 4.3: Residuals for Case 16

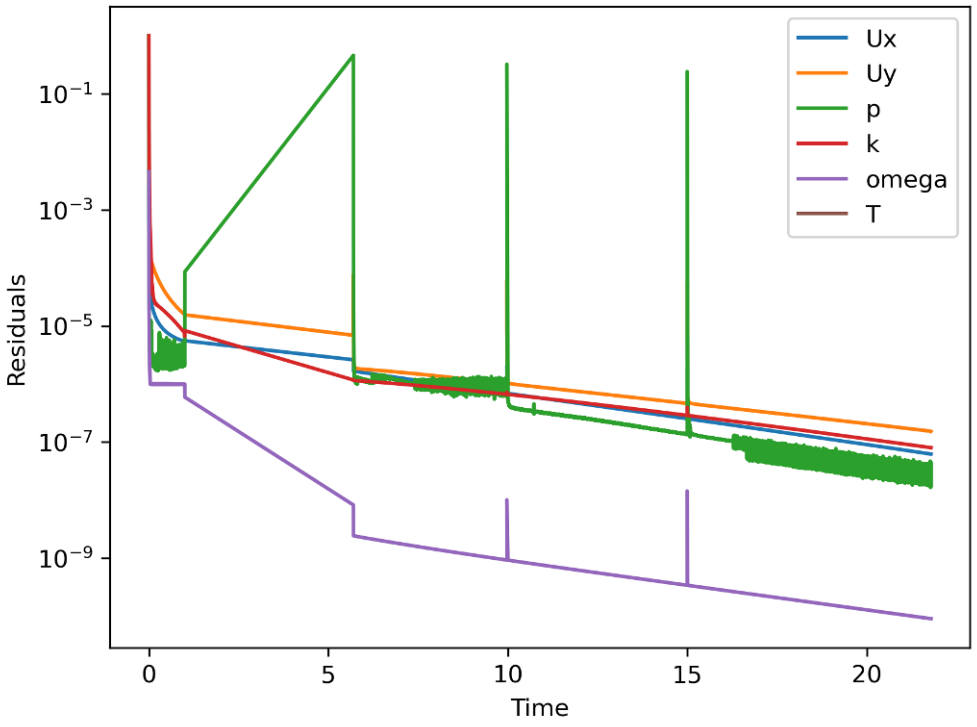

Figure 4.4: Residuals for Case 17

For the medium mesh refinement, it appears that the problem is still well set up, and the problem should reach a tight convergence $1e-9$ eventually, seen in Figure 4.3 and 4.4. The time constraint only allowed a solution to $1e-6$. However, this is till after $333e3$ and $605e3$ iterations for Case 16 and 17, respectively. Going for tighter residuals would be a higher price.

The trend of eventually reaching a convergence continues in the fine mesh refinement for both models, residuals seen in Figures 4.5 and 4.6. Case 19 may potentially stall after some extra iteration, but if that occurs, the order can be increased in the divergence scheme. The solution can keep going as Case 18 represents $500e3$ iterations, and $379e3$ iterations for Case 19.

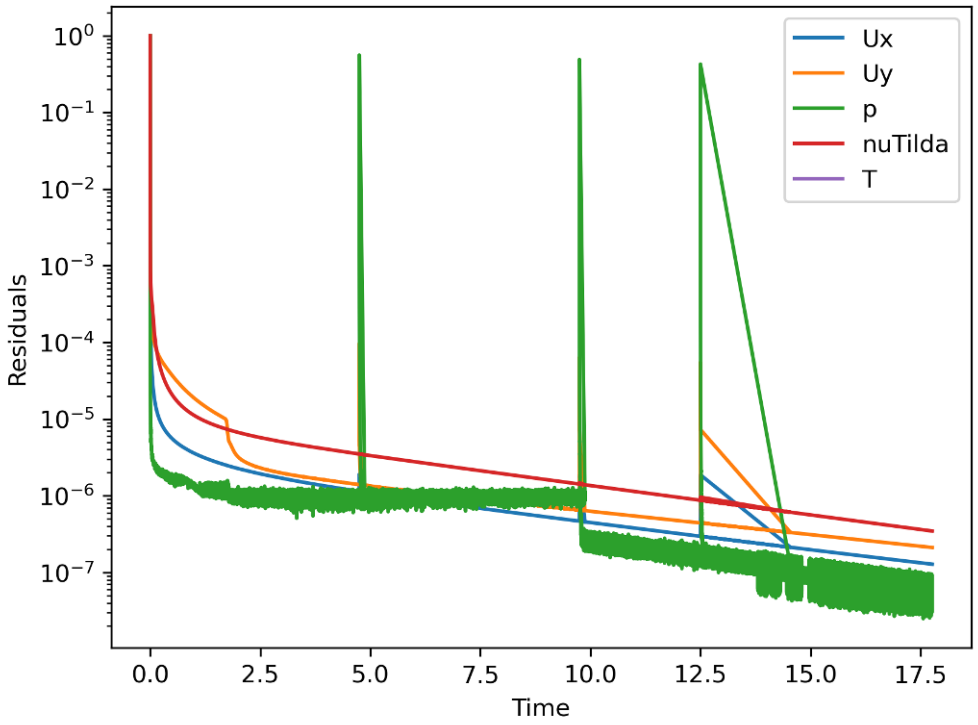

Figure 4.5: Residuals for Case 18

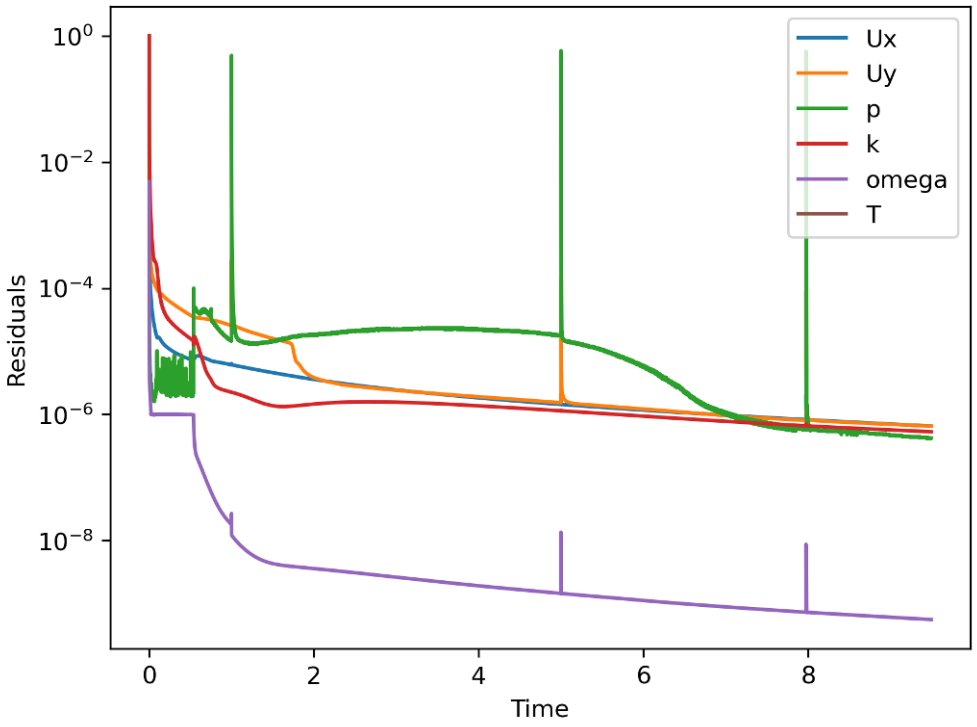

Figure 4.6: Residuals for Case 19

4.1.2 Contour Plots

Contour plots give a qualitative way to see what the data is to better understand the trends from quantitative data later on. The contours for the SA and $k-\omega$ models are present in Figures 4.7 and 4.8, respectively. In (a) for both, the velocity magnitude looks roughly the same and more information will be gained from the quantitative trends. The turbulent viscosity, ν_t, trend reveals some interesting differences. The SA model boundary layers show a subdued core of turbulent viscosity as the mesh refinement increases, but this may be due to needing more iteration. The freestream values for ν_t in the $k-\omega$ model vary greatly as the CFD calculates this value. Looking forwards to the quantitative trends, this does not appear to affect the boundary layer behavior. The SA model has large changes in the $\tilde{\nu}$ profile with mesh refinement. What causes this is unclear, but may suggest the SA model has less authority over the solve as the mesh refines, as $\tilde{\nu}$ is the only parameter the turbulence model has to transport. Looking at the scalars for the $k-\omega$ model, the k contours look about how one would expect, excepting Case 19, which appears to have an

underdeveloped boundary layer. This case likely needs to be iterated on more. The ω profiles are about how one would expect, with very strong dissipation near the wall, and heavy drop off away from the wall. Finally, the temperature profile is following the behavior that one expects with heavy mixing near the wall where the turbulence is strong, and strong deterioration without turbulence. Overall, most of these profiles look viable to use for recycling, maybe the fine mesh refinement cases need more iteration.

4.1.3 Boundary Layer Trend Plots

Contour plots are a decent qualitative way to view the behavior within the CFD, but lack the quantitative advantage of many of the boundary layer parameters that provide a better view as to what the flow is doing in the analysis. To set up the comparison of trends, there is a little background that needs to be explained. First, Kays and Crawford [19] provide some boundary layer trends relative to the momentum boundary layer thickness that are helpful. There is a good comparison between their regressions of boundary layer behaviors and ones set by White and Majdalani [45] for Prandtl's data. White and Majdalani took Prandtl's 1927 experimental data and found relations of unit length Reynolds number, Re_x, and development of the boundary layer. These relations match Kays and Crawford's trends well. However, White and Majdalani updated some of the input values of the boundary layer to match Coles' 1956 [13] data, there is an alternative trend that includes the wake behavior of the boundary layer. These are the canonical trends that are displayed in the figures.

(a) Velocity Magnitude Contours

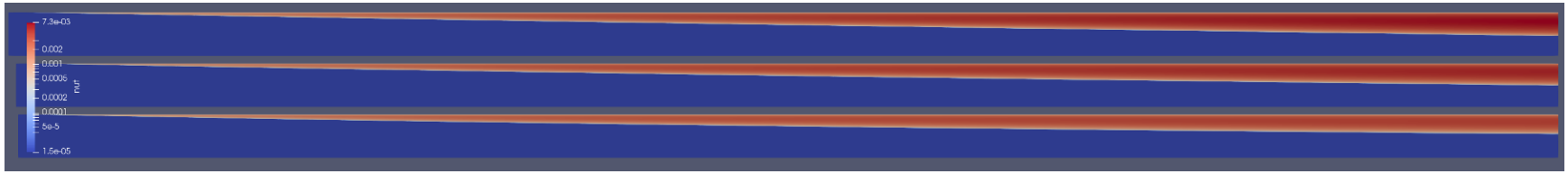

(b) ν_t Countours

(c) $\tilde{\nu}$ Contours

(d) Temperature Contours

Figure 4.7: Contour plots for SA Model RANS Flat Plate Simulation. Plots are for Cases 14, 16, and 18 , in that order.

(a) Velocity Magnitude Contours

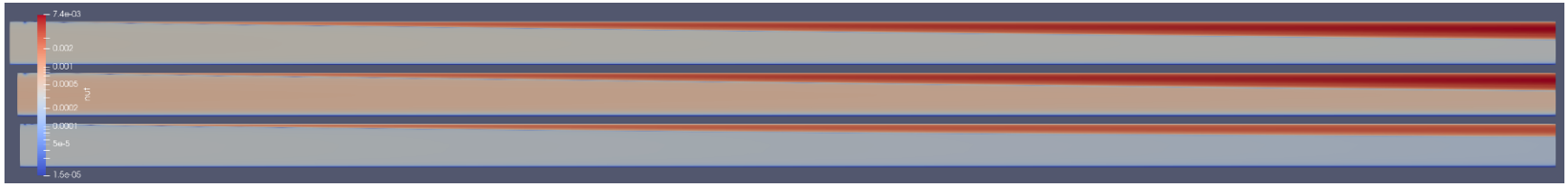

(b) ν_t Countours

(c) k Contours

(d) ω Contours

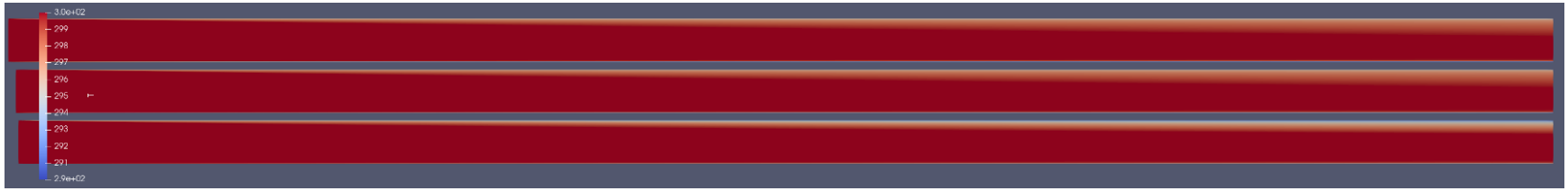

(e) Temperature Contours

Figure 4.8: Contour plots for $k-\omega$ SST Model RANS Flat Plate Simulation. Plots are for Cases 15, 17, and 19 , in that order.

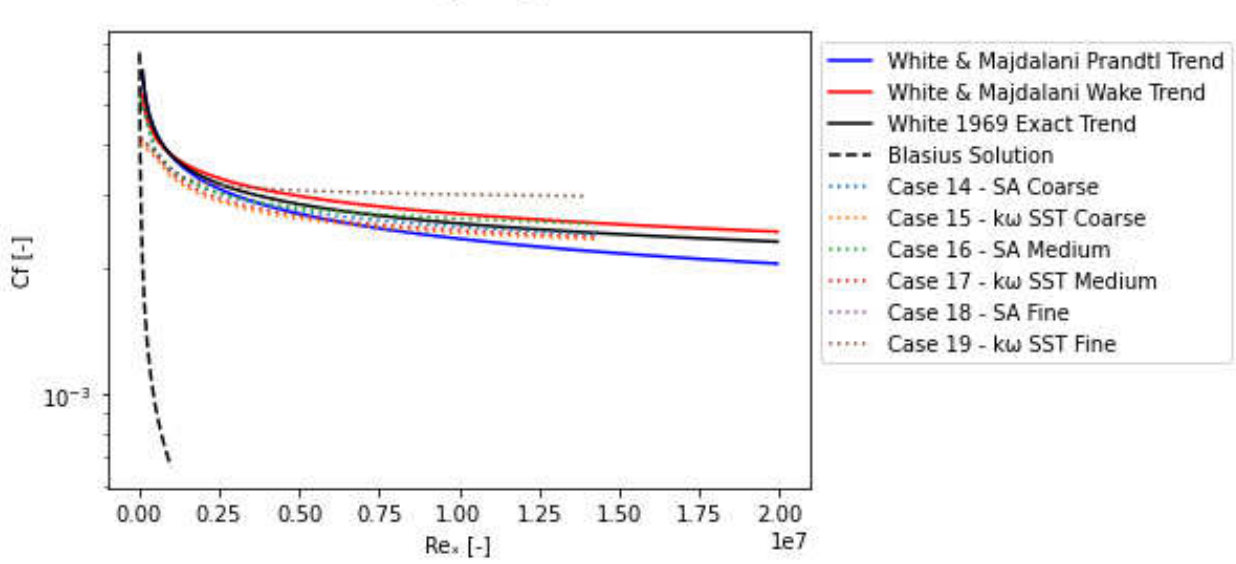

Figure 4.9: Skin Friction Trend vs Unit Length Reynolds Number.

The first parameter that is helpful to understand if the boundary layer is behaving correctly is skin friction coefficient, or C_f, which non-dimensionalizes the shear relative to the freestream flow. The trend for the cases is shown in Figure 4.9. Before discussing anything else, the boundary layer data comes to good agreement with the expected behavior within $Re_x = 5.0e6$, which is early in the turbulence development, with the exception of Case 19. All RANS models are within the different datasets. Case 19, however, needs more iteration to develop into the proper trend, which is evident in its residual plot. With this plot, the difference in expected trends needs discussion. First, White's 1969 paper provides a relation, seen in Equation 4.1 that is acceptable as an exact solution to the skin friction trend that White and Majdalani emphasize [45]. Second, there is a difference for these higher Reynolds numbers between the trends produced by Prandtl's 1927 data and the trends using Coles' 1956 wake data, the fit equations seen in Equations 4.2 and 4.3, respectively. The data for the wake trend matches the exact solution better for higher Reynolds numbers, and thus this study will accept it as the canonical trend over Prandtl's data. However, when comparing to momentum boundary layer thickness, the Prandtl-based data is acceptable since this should be less affected by the wake behavior, which leads to the Kays and Crawford trends [19]. Kays' and Crawford's trend lines up with the Prandtl-based trends White and Majdalani suggest, by comparing Equations 4.4

and 4.2, respectively.

$$C_f = \frac{0.455}{ln^2(0.06Re_x)} \tag{4.1}$$

$$C_f = 0.0593Re_x^{-1/5} \tag{4.2}$$

$$C_f = 0.0271Re_x^{-1/7} \tag{4.3}$$

$$C_f = 0.0574Re_x^{-1/5} \tag{4.4}$$

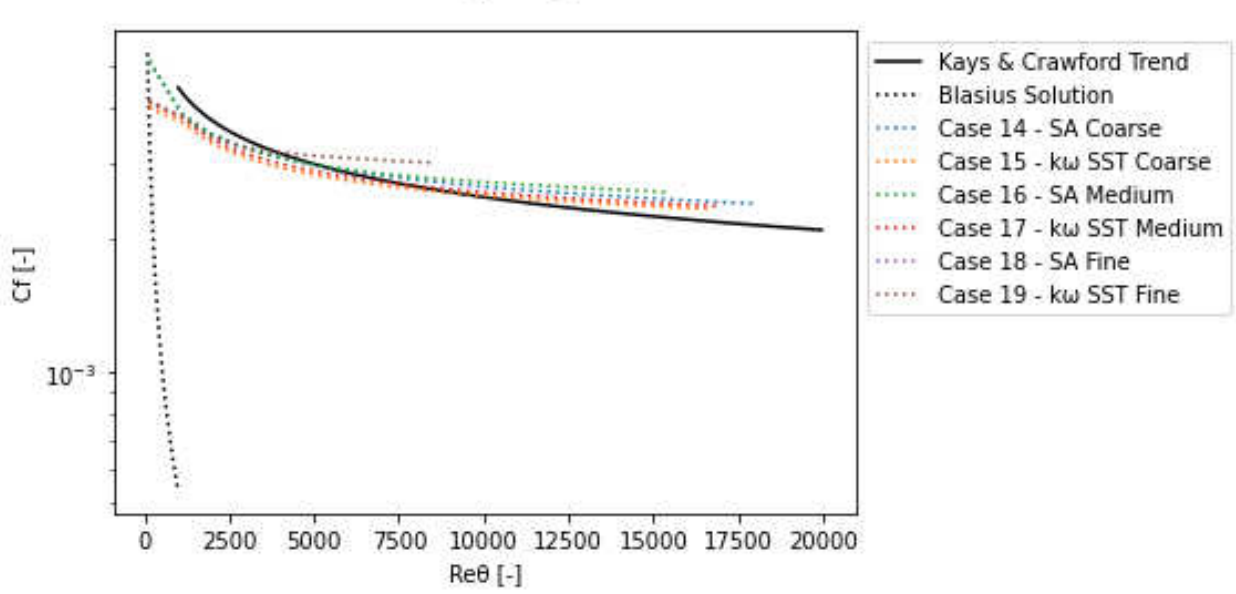

Figure 4.10: Skin Friction Trend vs. Momentum Boundary Layer Thickness Reynolds Number.

Seen in Figure 4.10, the comparison of skin friction coefficient against the momentum boundary layer thickness Reynolds number shows good agreement between the expected trend and the RANS data. This indicates that the boundary layer is developing roughly correctly. The expected trend follows Equation 4.5. The $k - \omega$ model cases, with the exception of Case 19, are showing good agreement between the mesh refinement levels.

$$C_f = 0.025 Re_\theta^{-1/4} \tag{4.5}$$

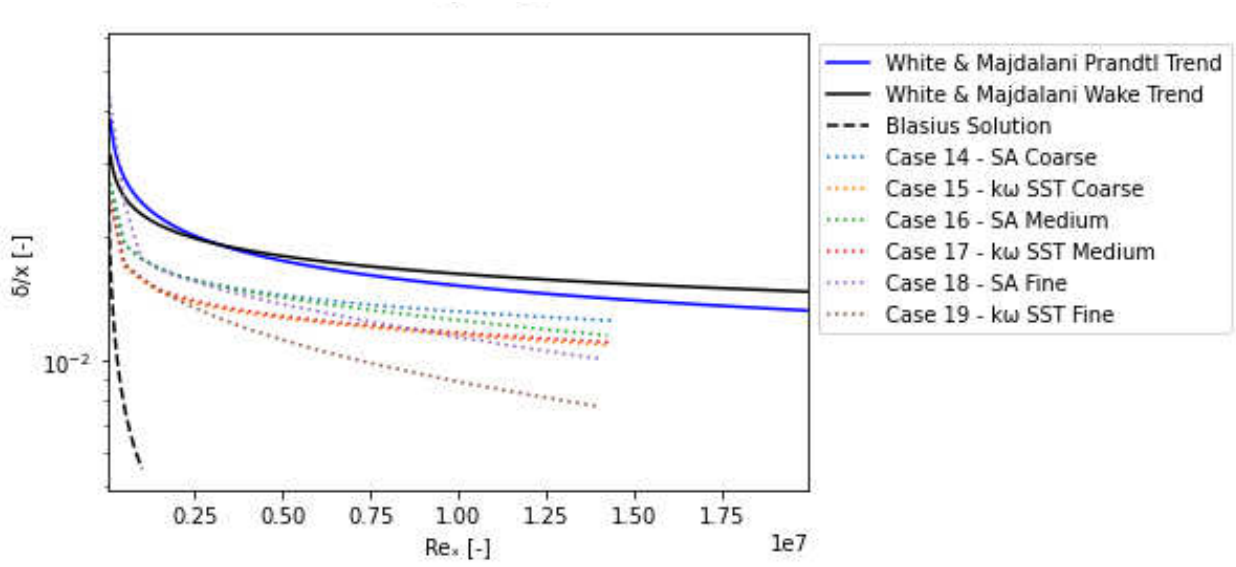

Figure 4.11: Boundary Layer Development Trend vs Unit Length Reynolds Number.

Comparing the development of the boundary layer height shows that the boundary layer is underdeveloping down the length of the flat plate, as seen in Figure 4.11. This, however, seems to be an offset and the rate of change appears to follow the wake data trend closely, described in Equation 4.7. As discussed in the methods section, the flow does increase in velocity by 4.1%, which only accounts for either a 0.805% or 0.574% deviation in trend, depending on the preferred exact solution. Thus, this is likely not due to the duct behavior rather than a true flat plate. It is more likely that the offset is due to the under-resolution at the beginning of the boundary layer as it starts from uniform flow. The under-resolution will alter the development trend as the CFD has too few points to resolve the wall-bounded behavior. Also in Figure 4.11, Cases 18 and 19 are deviating from the expected behavior. This indicates that the analysis needs more iteration to come to a proper resolution. The finer cases may be more sensitive due to more of the wall-bounded behavior being resolved by the Navier-Stokes equations and less modeled by the turbulence models. For the rest of the discussion on the Inlet Duct, Cases 18 and 19 are ignored for this reason.

$$\delta/x = 0.381 Re_x^{-1/5} \tag{4.6}$$

$$\delta/x = 0.162 Re_x^{-1/7} \tag{4.7}$$

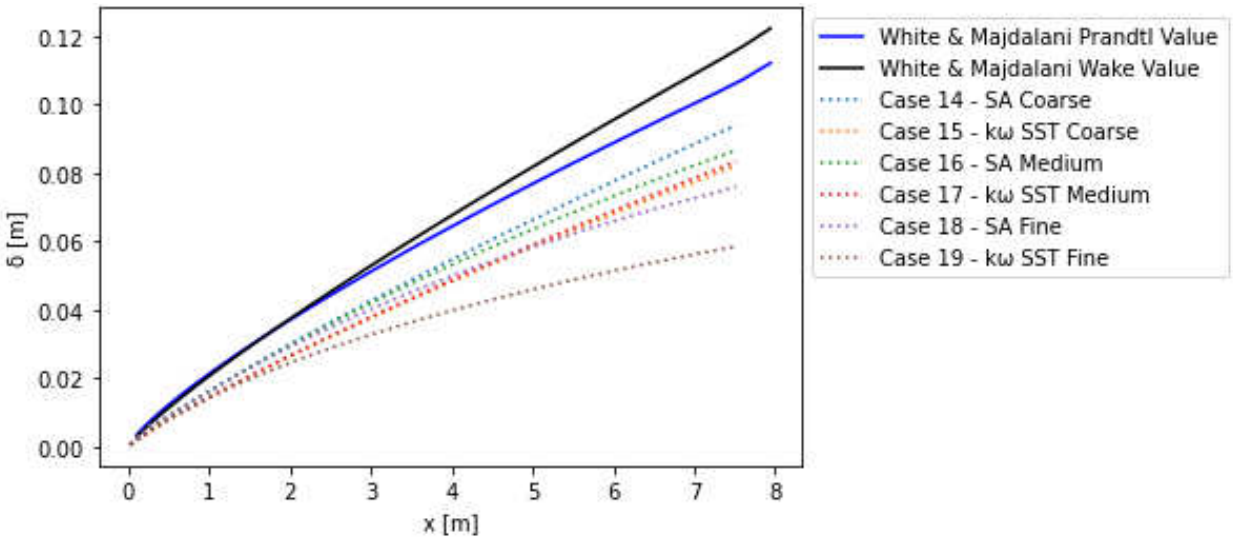

Figure 4.12: Boundary Layer Development

The results of this development trend is quite clear when comparing the boundary layer height to the expected trend, as in Figure 4.12. It is interesting that for the boundary layer height, the wake value does produce a taller boundary layer, which is understandable considering the wake includes an additional shelf above the law of the wall behavior. In either case, the boundary layer height appears to be noticeably less than the expected, owing to the deficient trend seen in Figure 4.11.

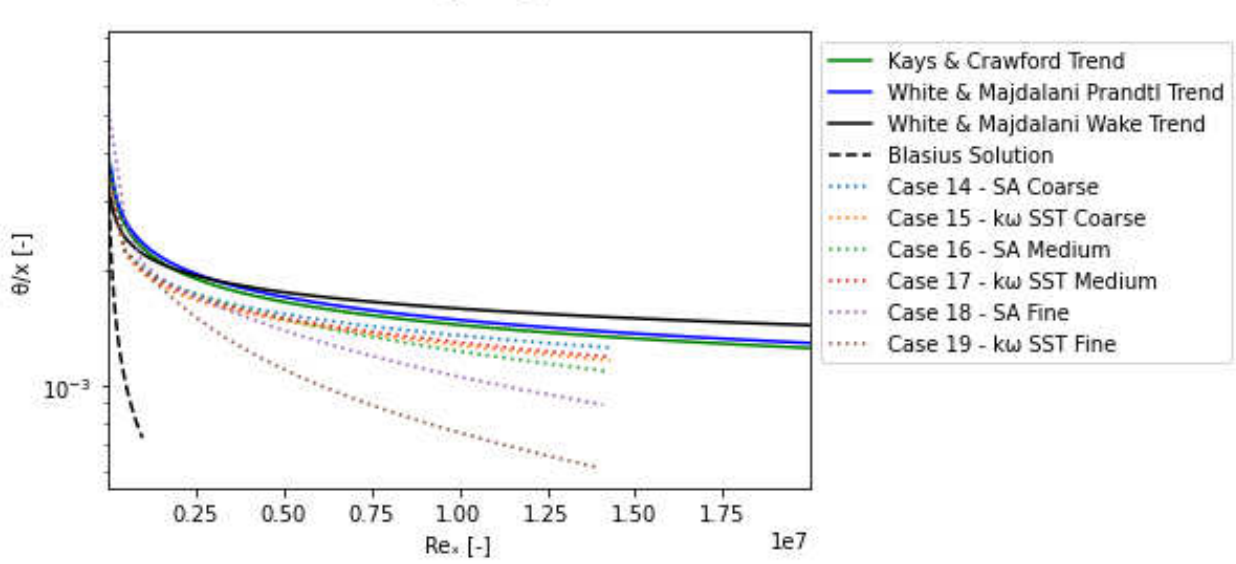

Figure 4.13: Momentum Boundary Layer Development Trend vs Unit Length Reynolds Number.

Changing the trend comparison to the momentum boundary layer thickness, θ, the RANS data follows the expected trend much closer than the boundary layer height, as seen in Figure 4.13. Interestingly, the data follows the Prandtl-data based trends, as in Equations 4.8 and 4.9, more than the wake law-based trend, as described by Equation 4.10. Additionally, Kays & Crawford, Equation 4.8, have much closer agreement with White & Majdalani, Equation 4.9, for this trend. This would make sense as a bulk of the flow would be determined by the self-similar Log Law of the Wall for θ. Here, the insensitivity to mesh refinement for the $k-\omega$ model is well illustrated, excepting the odd Case 19. It is interesting that the SA model shows a sensitivity. Following the previous hypothesis on model vs NS equations, this may indicate that the SA model has a more significant floor to resolution vs required iteration than the $k-\omega$ model. Also, the logarithmic scale of the y-axis for this plot may allow us to be more critical than may be necessary for this trend.

$$\theta/x = 0.036 Re_x^{-1/5} \tag{4.8}$$

$$\theta/x = 0.0371 Re_x^{-1/5} \tag{4.9}$$

$$\theta/x = 0.0158 Re_x^{-1/7} \tag{4.10}$$

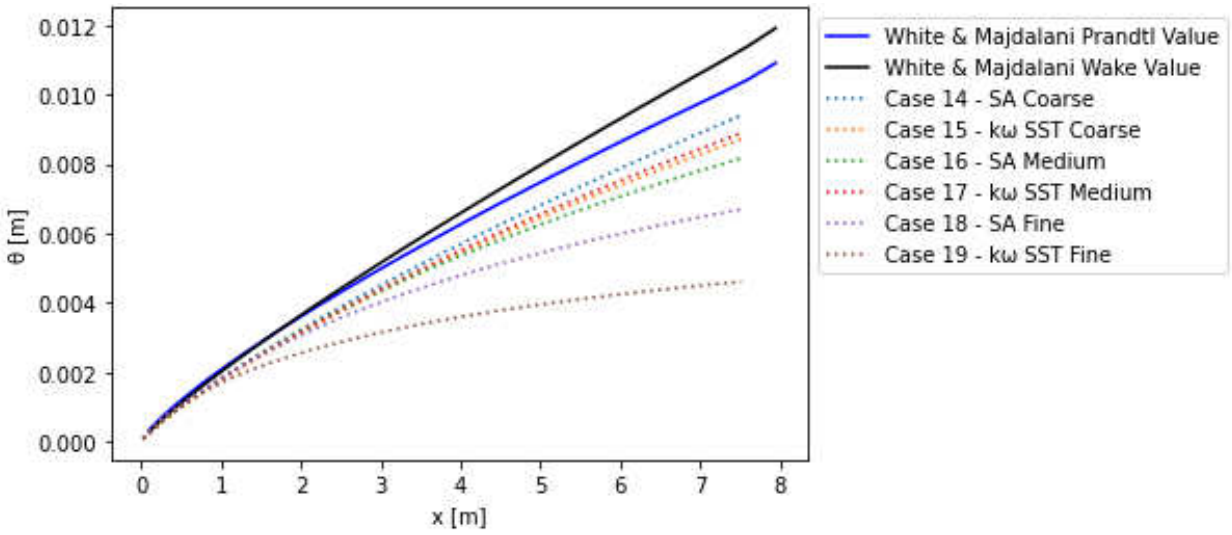

Figure 4.14: Momentum Boundary Layer Development

The results of this development trend are clearly present in the development of the momentum boundary layer, as seen in Figure 4.14. The momentum boundary layer heights for the RANS data is underpredicted to an extent, but generally shows good agreement with the expected trends.

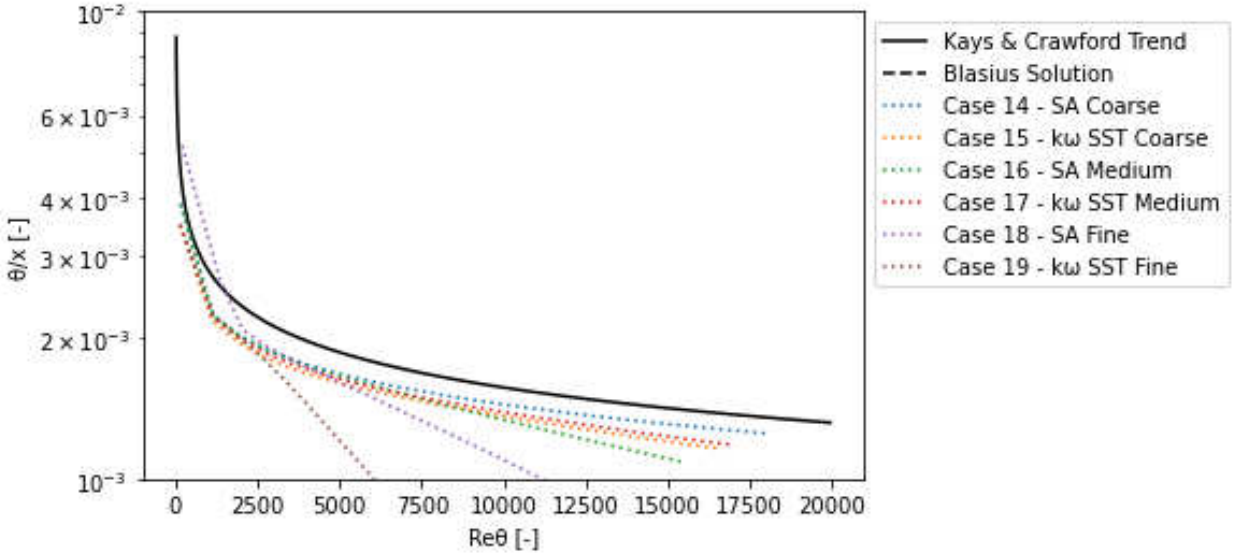

Figure 4.15: Momentum Boundary Layer Development Trend vs. Momentum Boundary Layer Thickness Reynolds Number.

The development trend for momentum thickness boundary layer is displayed in Figure 4.15 follows the expected trend, described in Equation 4.11 that was derived from Kays & Crawford trends, closely. This would indicate that some of the seen deviation does exist from some offset in the development, and there is some caused by the solving of the RANS analysis. It appears that Case 16 by this trend has some iteration required to converge to a proper downstream solution.

$$\theta/x = 0.036 \left((Re_\theta/0.036)^{5/4} \right)^{-1/5} \tag{4.11}$$

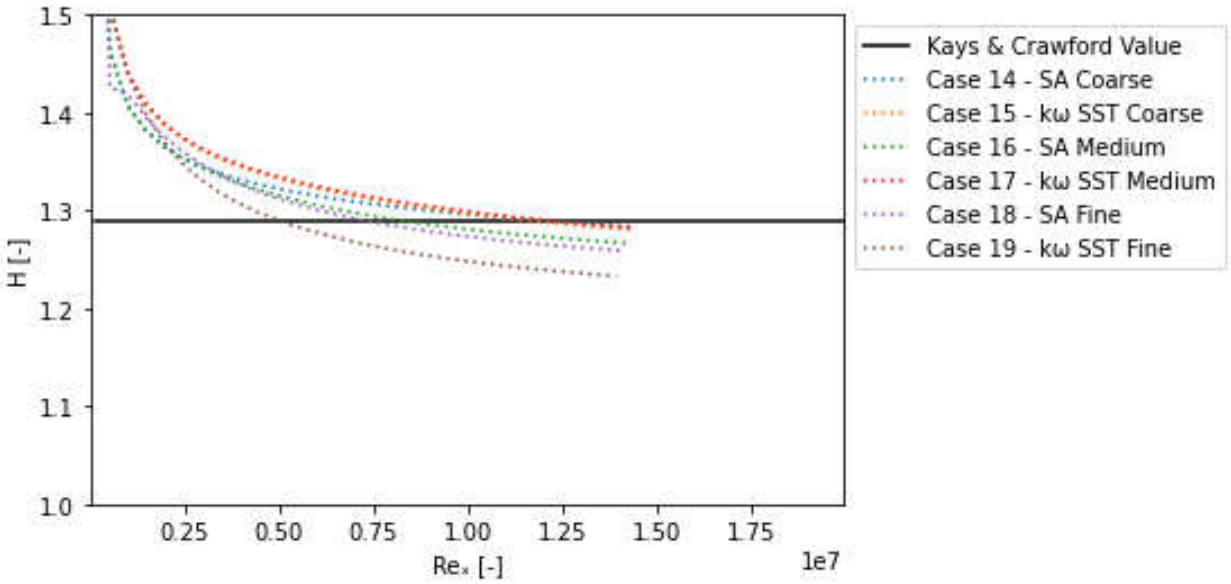

Figure 4.16: Shape Factor vs Unit Length Reynolds Number

Finally, the shape factor allows an assessment of if the boundary layer is structured correctly. Kays & Crawford offer a value of 1.29, which is in agreement with White & Majdalani's $9/7$, and somewhat close to Coles' 1.32 [31]. The RANS data converges near these values as the boundary layer develops, seen in Figure 4.16, and for higher Reynolds numbers, $5.0e6$ and above, the RANS models show good agreement with the expected trend and to each other.

Comparing these trends through quantification helps determine how much uncertainty there is from the RANS models against the exact solutions. To do this, the data is limited to the regions where the streamwise gradient of shape factor is less than 0.50% of the shape factor at a given

point. This should limit the data to the boundary layer that has developed to turbulent. This data is then calculated in an L2 error norm calculation, as in Equation 4.12. The values for each of the flow parameters considered are in 4.2. In the last row is the uncertainty associated with the acceleration of the flow vs if this was a true flat plate case, calculated via the ratio of velocities in the exact solution. A few things immediately stick out. First, the skin friction coefficient generally outperforms the uncertainty from the duct, which indicates that the shear normalized by the freestream conditions are insensitive to the freestream conditions. Second, the momentum boundary layer thickness development normalized by the momentum boundary layer thickness fits within the associated uncertainty. The boundary layer development by streamwise length is likely due to the under-resolution issues discussed earlier. Finally, the shape factor has a tight uncertainty bounds.

Case	C_f by x	C_f by θ	H	δ/x	θ/x by x	θ/x by θ
14	0.538%	1.64%	0.342%	3.99%	2.96%	1.67%
16	0.653%	2.25%	0.280%	4.92%	4.70%	3.77%
18	-	-	0.333%	6.51%	7.18%	6.90%
15	1.26%	0.842%	0.379%	6.30%	4.17%	3.07%
17	0.964%	1.17%	0.404%	6.11%	3.87%	2.67%
19	3.87%	2.75%	0.707%	10.2%	11.7%	12.3%
Duct	7.70%	1.01%	-	0.574%	0.574%	4.30%

Table 4.2: L2 Norm Error for Inlet Duct Free Development

$$\epsilon_{L2} = \frac{1}{N}\sqrt{\Sigma\left(\frac{\phi}{\phi_{exact}} - 1\right)} \tag{4.12}$$

Ideally, a true flat plate case should be used to compare the flat plate data, but this became impractical with the exponentially rising queue times for the HPC partitions.

CHAPTER 5: PATRICK TEST SECTION

The Test Duct analyses are done in six (6x) cases that are outlined in Table 6.1.

Refinement	SA Model Cases	$k-\omega$ SST Model Cases
Coarse	0	1
Medium	2	3
Fine	4	5

Table 5.1: Cases Used for the Patrick Duct Analyses.

5.1 Residuals

The residuals for the coarser mesh cases show are seen in Figures 5.1 and 5.2. The coarse SA case, Case 0 is clearly well set up with no hindrances towards convergence. The coarse $k-\omega$ case, Case 1, appears to level off the pressure residual at about $5e-7$. It appears the limiting factor is the k iteration, and perhaps changing the divergence scheme to a higher order scheme could solve this issue. However, the other residuals come down to $1e-9$ for Case 1. Case 0 and 1 represent $250e3$ and $337e3$ iterations, respectively.

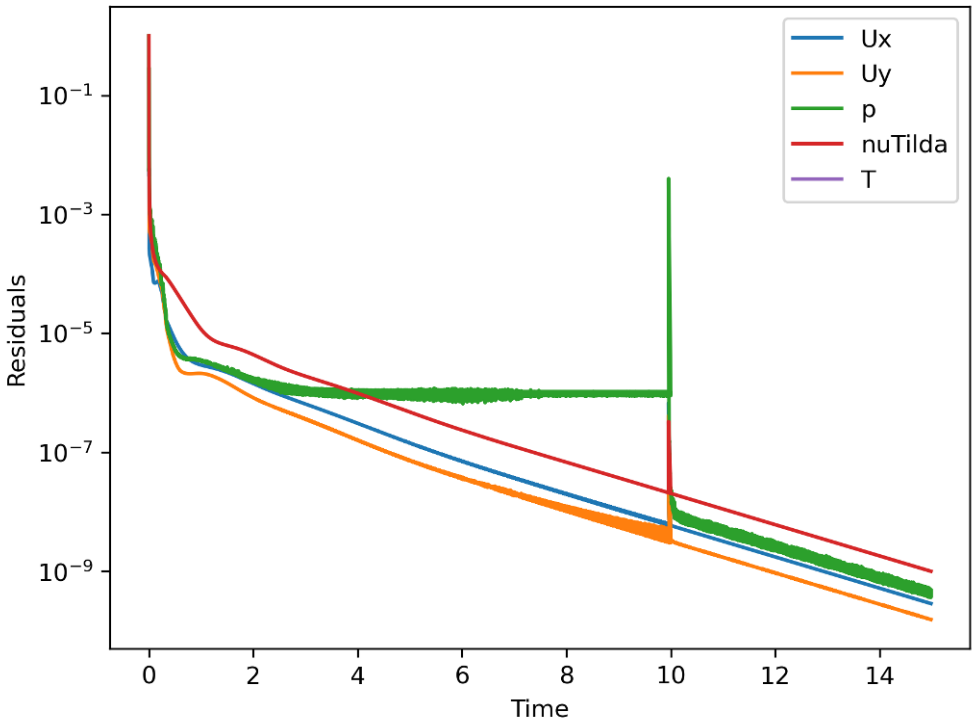

Figure 5.1: Residuals for Case 0

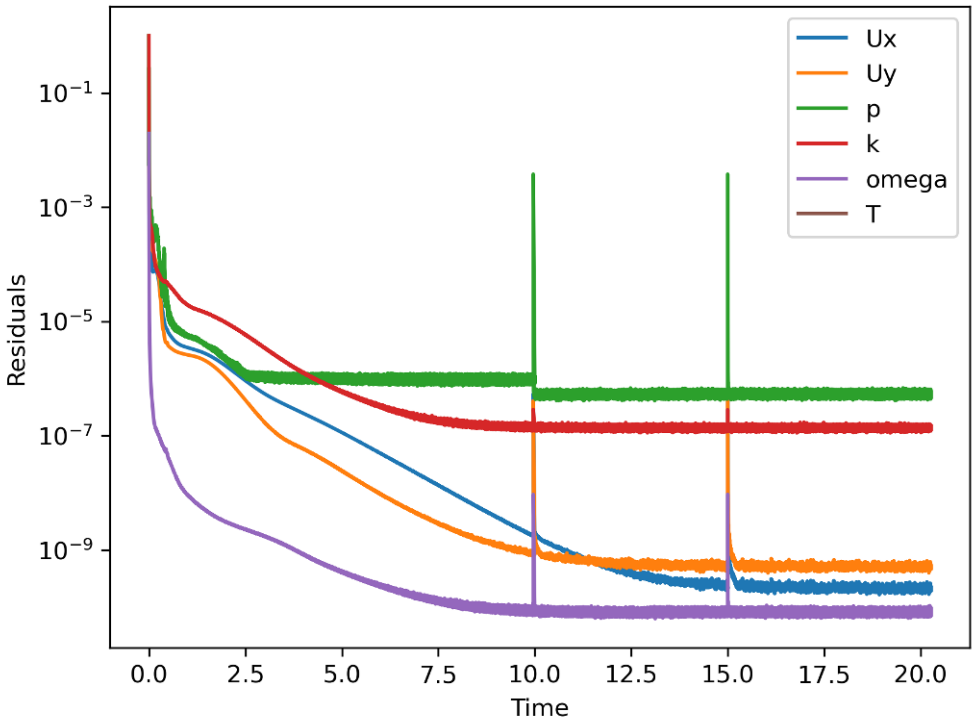

Figure 5.2: Residuals for Case 1

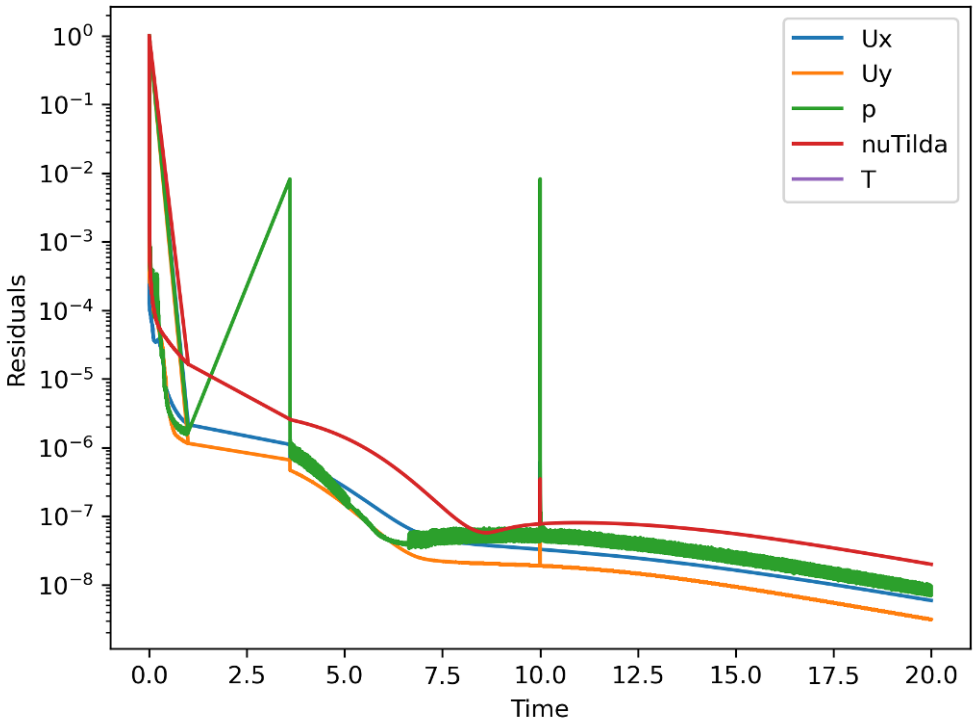

Figure 5.3: Residuals for Case 2

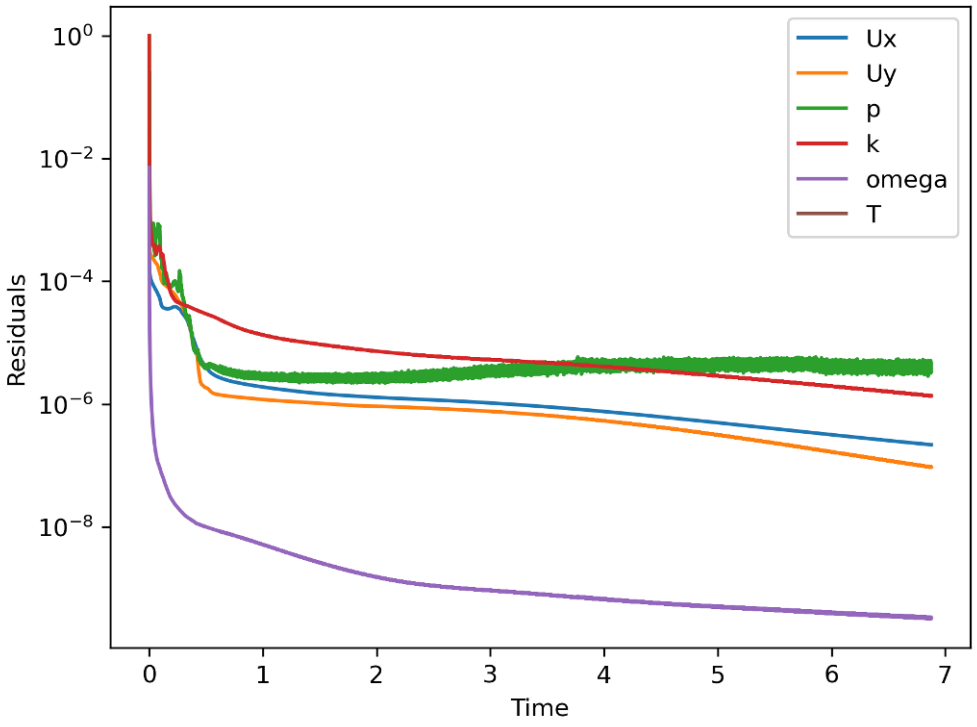

Figure 5.4: Residuals for Case 3

The residuals for the medium case are similar to the coarse case. Case 2, residuals in Figure 5.3, is a well-set up problem that will converge, given enough iterations. Case 2 is already at $500e3$ iterations in these results. Case 3, residuals in Figure 5.4, is unclear if it would converge, or if it would stagnate like Case 1. Most likely it would stagnate, and it would need a similar number of iterations to reach this, with Case 3 already being at $171e3$ iterations.

5.2 Contour Plots

The contour plots match the expected data that Patrick at least from a qualitative comparison. As seen in Figure 5.5, there is a separation bubble on the flat test surface. As seen in Figure 5.6, within the bubble, the flow profile reverses. In both of these sets of figures, there is clearly a difference between the two cases and turbulence models. The structure of the separation effect is displayed in Figure 5.8 that shows the turbulent viscosity of the separation bubble. There is clearly a more local and striated effect in the $k-\omega$ case of Case 1 than the SA case of Case 0, where the turbulent viscosity forms a smooth bubble. The different scalars, seen in Figure 5.9, also show a different behavior between the turbulence models. The $\tilde{\nu}$ contours for Case 0 follow the distribution of turbulent viscosity closely. But, there is clearly a tail of turbulent kinetic energy, k, for the $k-\omega$ model that follows the rim of the separation bubble. It is also interesting that the dissipation, seen in Figure 5.10, leads the separation and disappears following the separation. However, these two cases show agreement in the pressure distribution, seen in Figure 5.11. One notices that the final turn into the outlet of the test duct produces a strong low-pressure zone that drops the pressure of the flow profile going into this duct. Looking at the data Patrick presents, this does not seem physical and may be an issue with the zero-gradient wall conditions that may not be valid for this set of conditions. Finally, it also appears that the scalar transport behavior is in good agreement between the models, seen in Figure 5.12. There is some discrepancy as to the inlet conditions, but discounting this, that does appear to be the case.

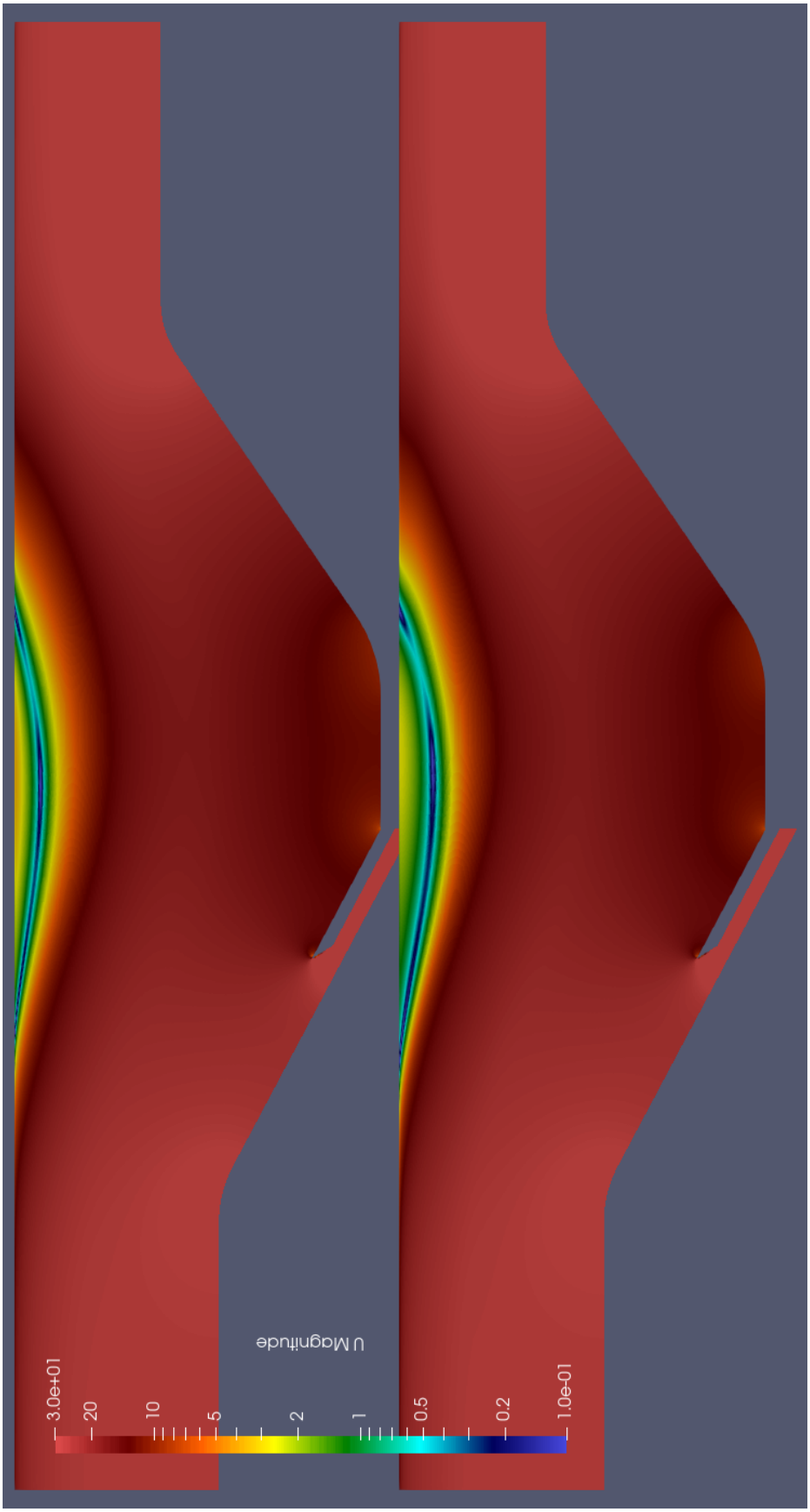

Figure 5.5: Contours of Velocity Magnitude for Cases 0 and 1

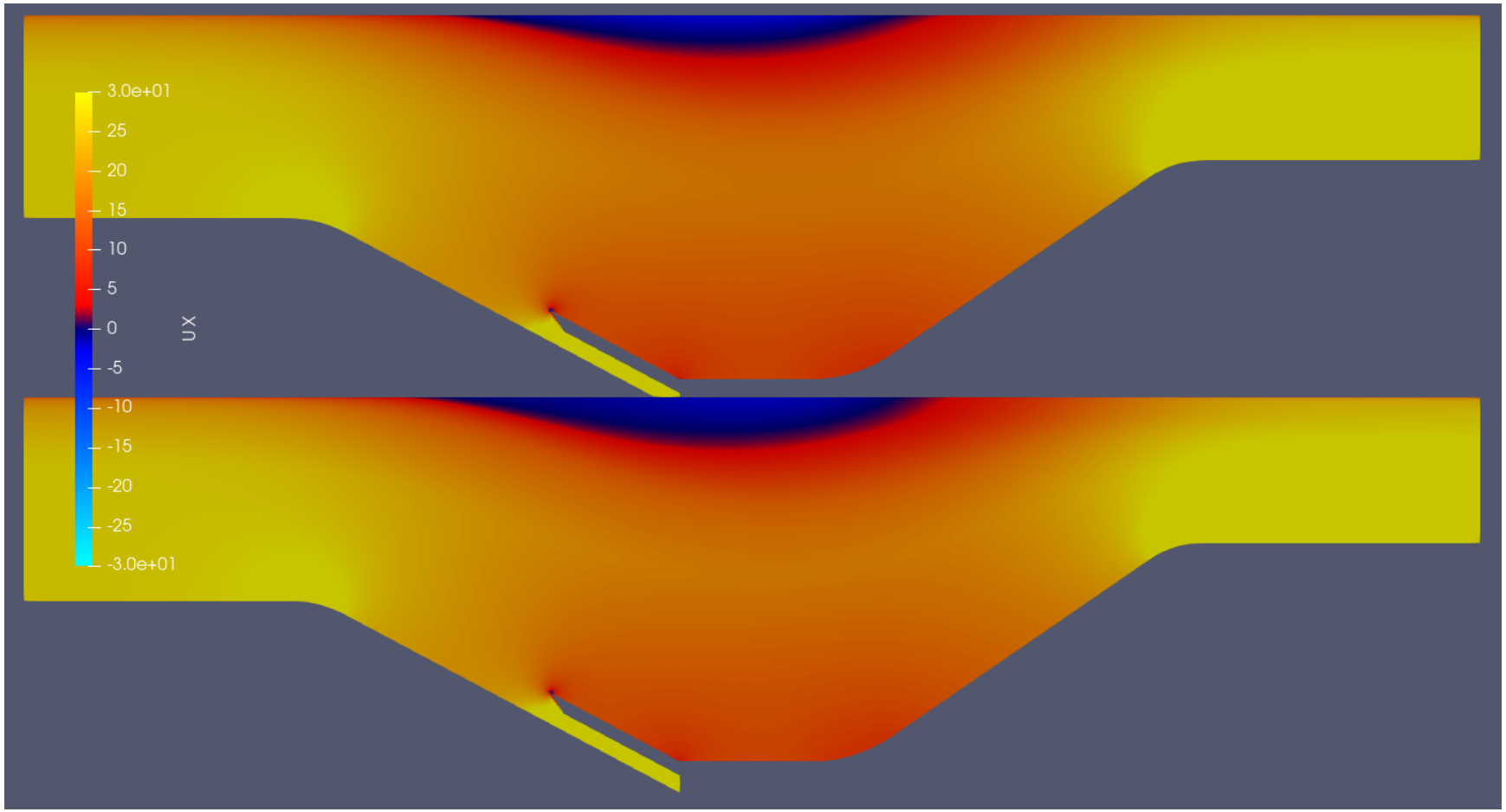

Figure 5.6: Contours of x-Velocity for Cases 0 and 1

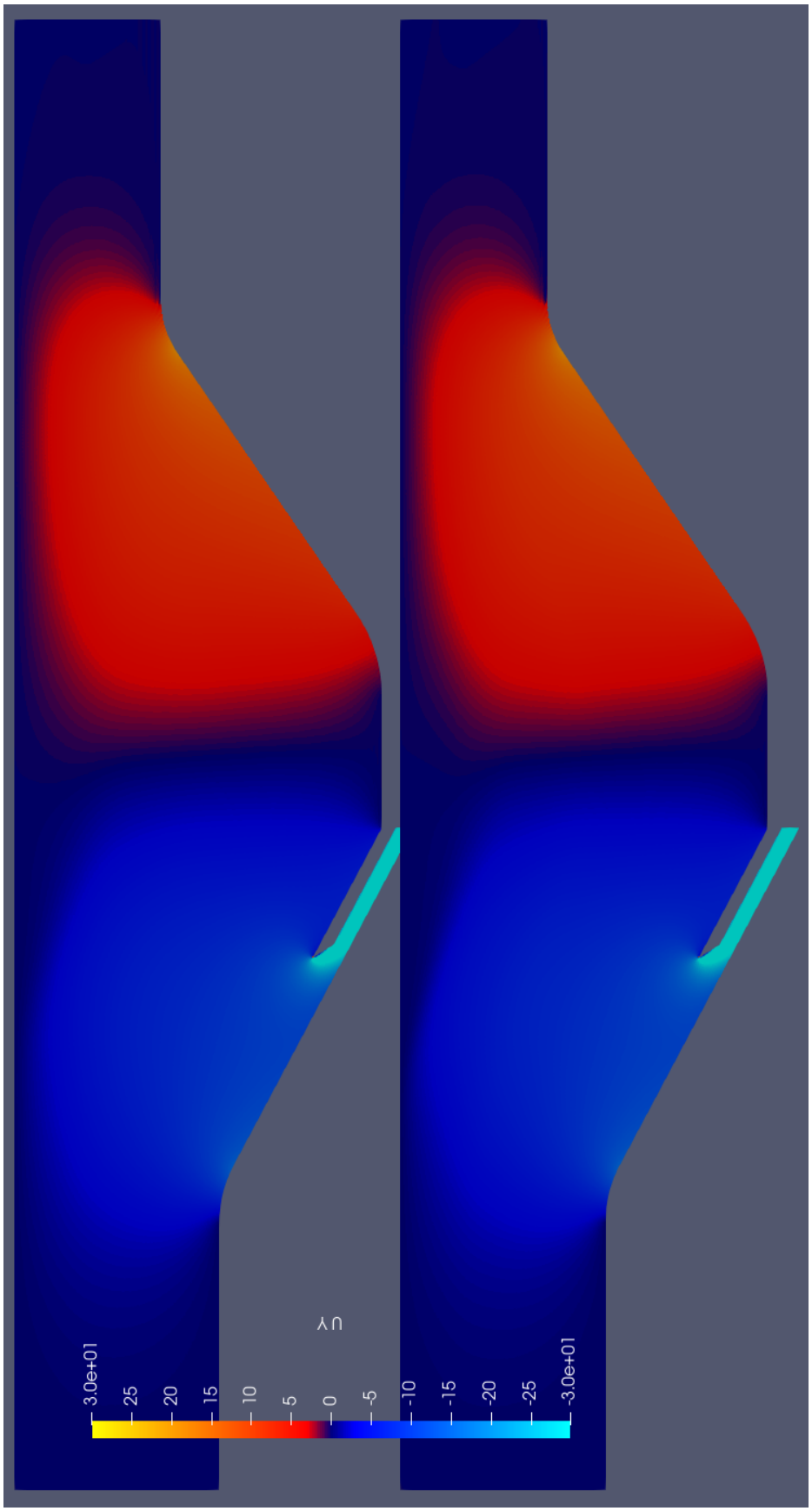

Figure 5.7: Contours of y-Velocity for Cases 0 and 1

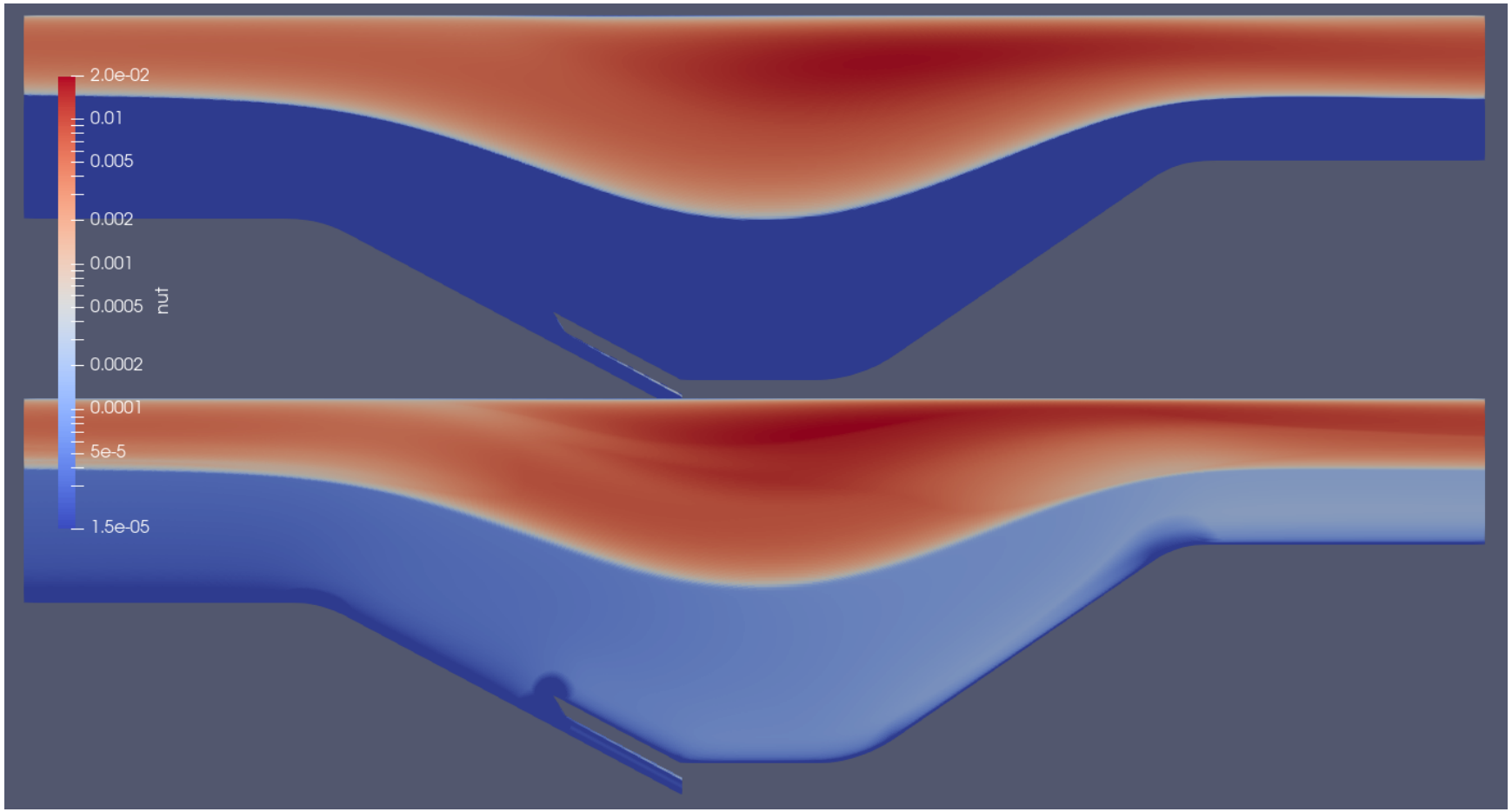

Figure 5.8: Contours of Turbulent Viscosity for Cases 0 and 1

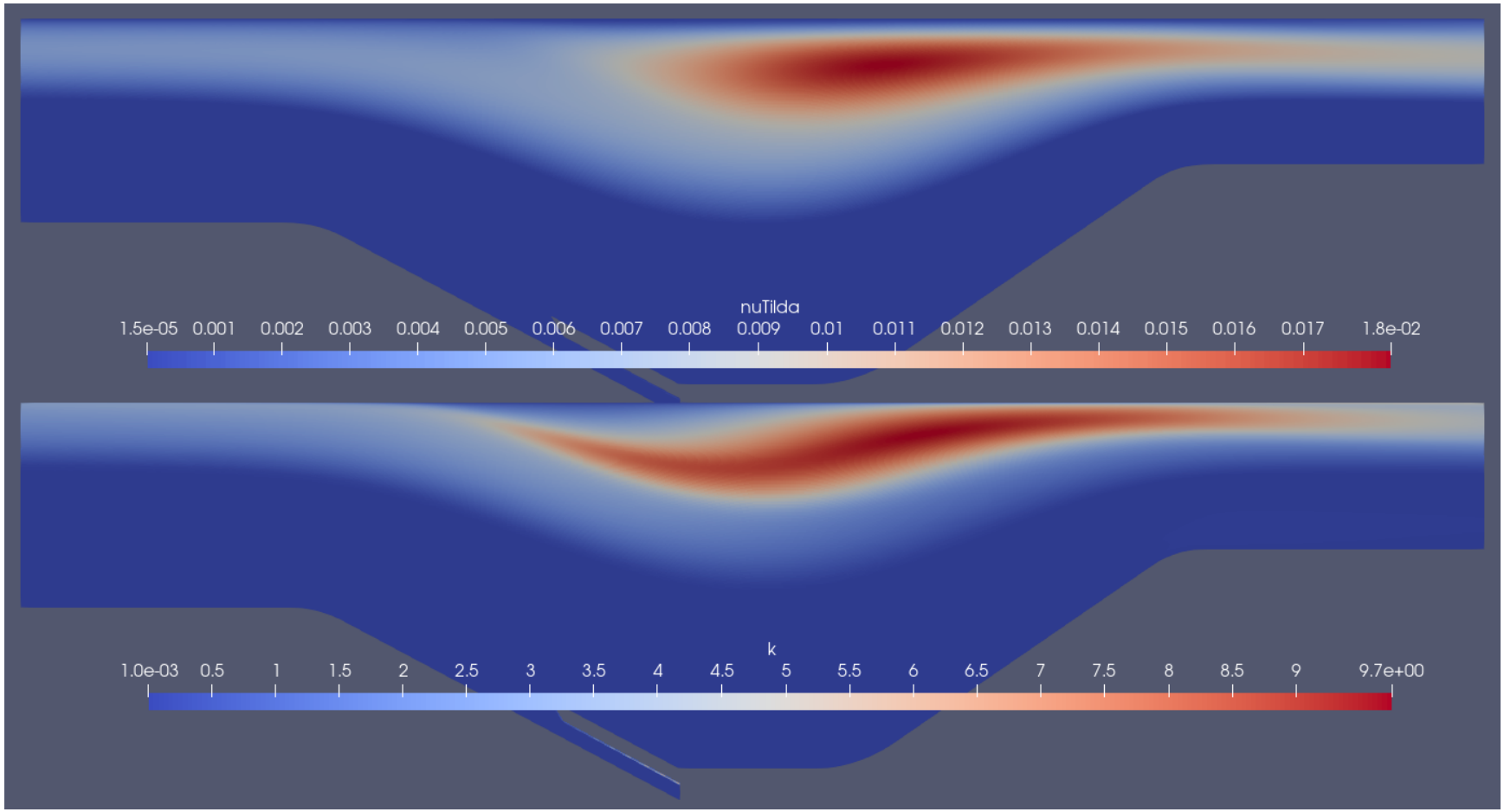

Figure 5.9: Contours of Respective Turbulent Scalar for Cases 0 and 1

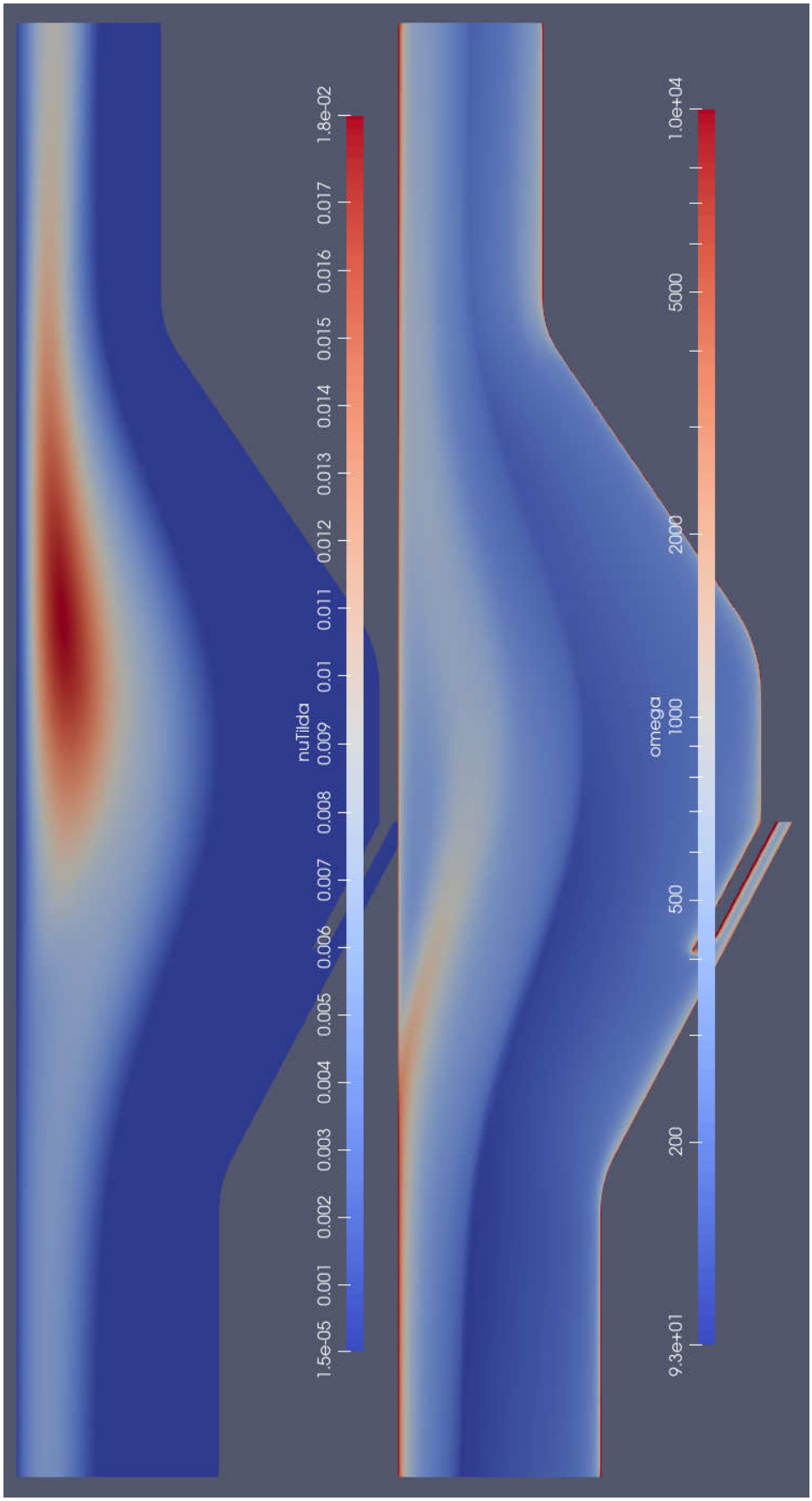

Figure 5.10: Contours of Turbulent Dissipation for Cases 0 and 1

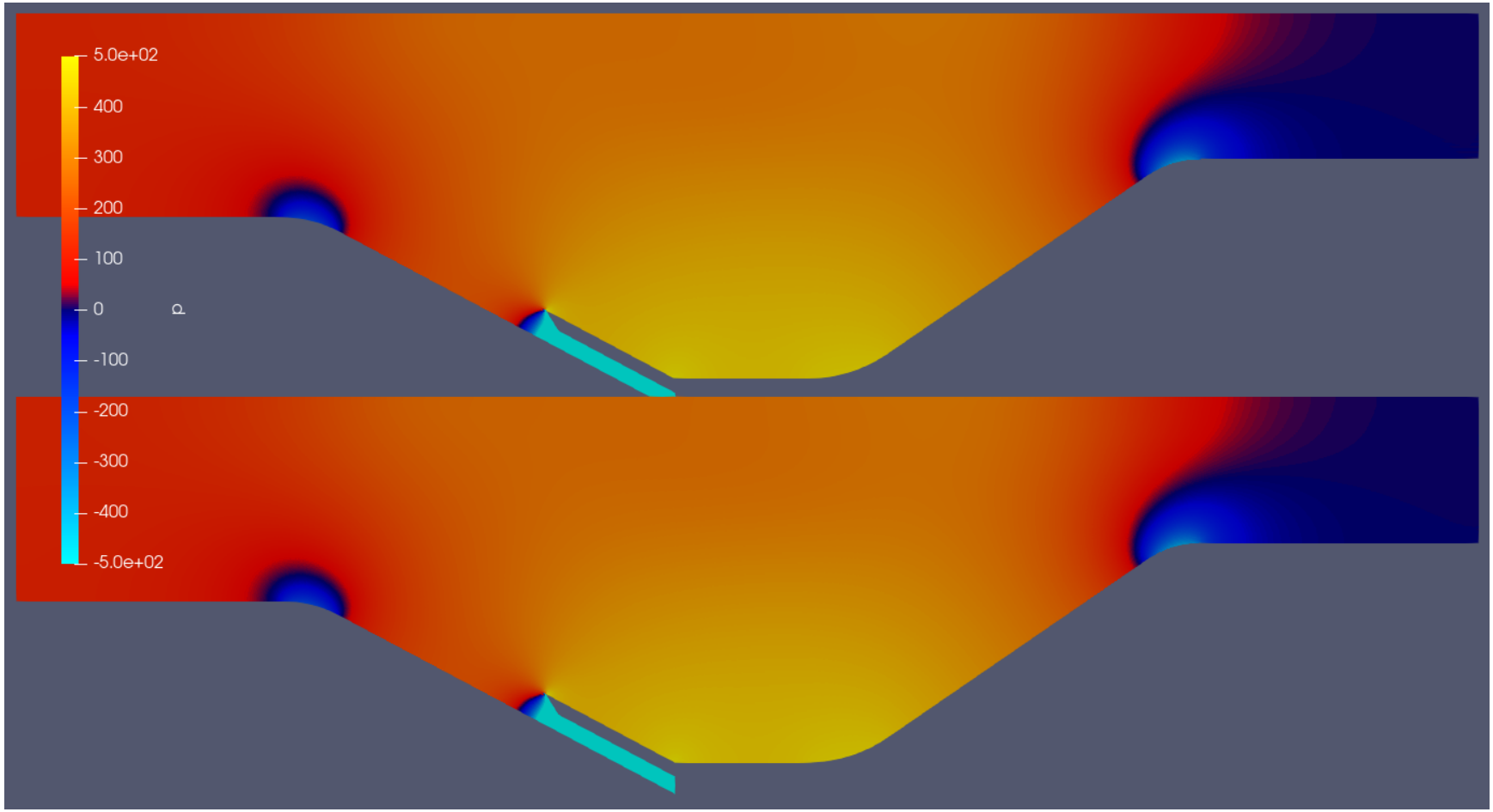

Figure 5.11: Contours of Pressure Distribution for Cases 0 and 1

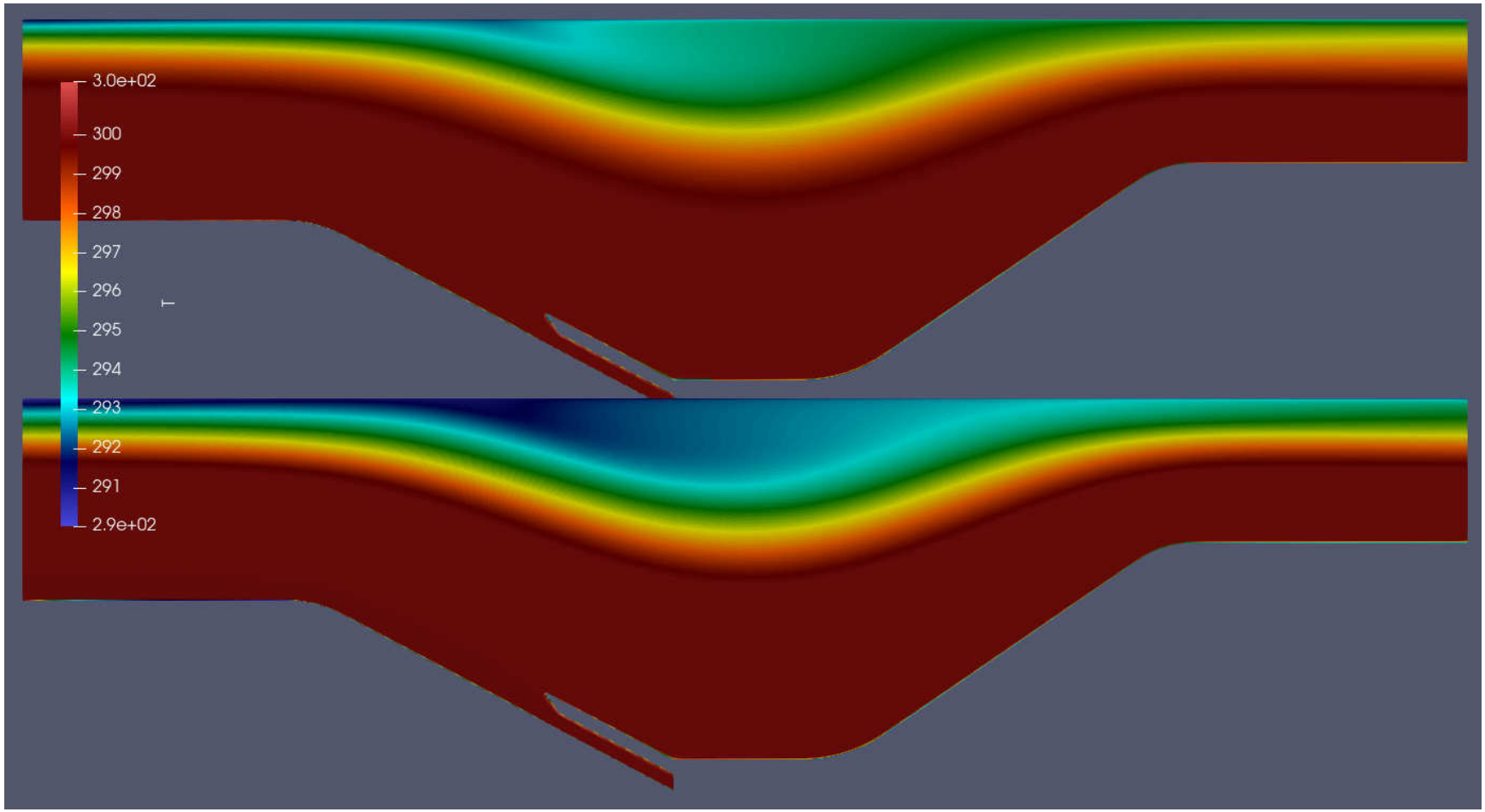

Figure 5.12: Contours of Temperature Distribution for Cases 0 and 1

5.3 Data Comparison Plots

Another way to look at the data is comparing the results from the CFD analyses to the data Patrick gathered directly via the plots Patrick produced.

First, the inlet profile of the flow needs to be correct. Patrick measured upstream of the inlet of the test section by about $0.23m$, and the comparison is drawn for the inlet of the CFD domain, which should have the difference of a slightly stronger wake, which can be seen in Figure 5.13. In a quantitative comparison of inlet conditions, the skin friction coefficient is appreciably lower than both the Patrick and Coles measured values, roughly 4%, seen in Table 5.2. However, when compared to the expected exact solution, described by Equation 4.5 from Kays & Crawsford [19], the calculated value is above what would be expected, $2.35e-3$, which differs by 4.59%. Comparing the shape factor at the inlet to the measured values from Patrck and Coles, there is strong agreement between the values, as seen in Table 5.3.

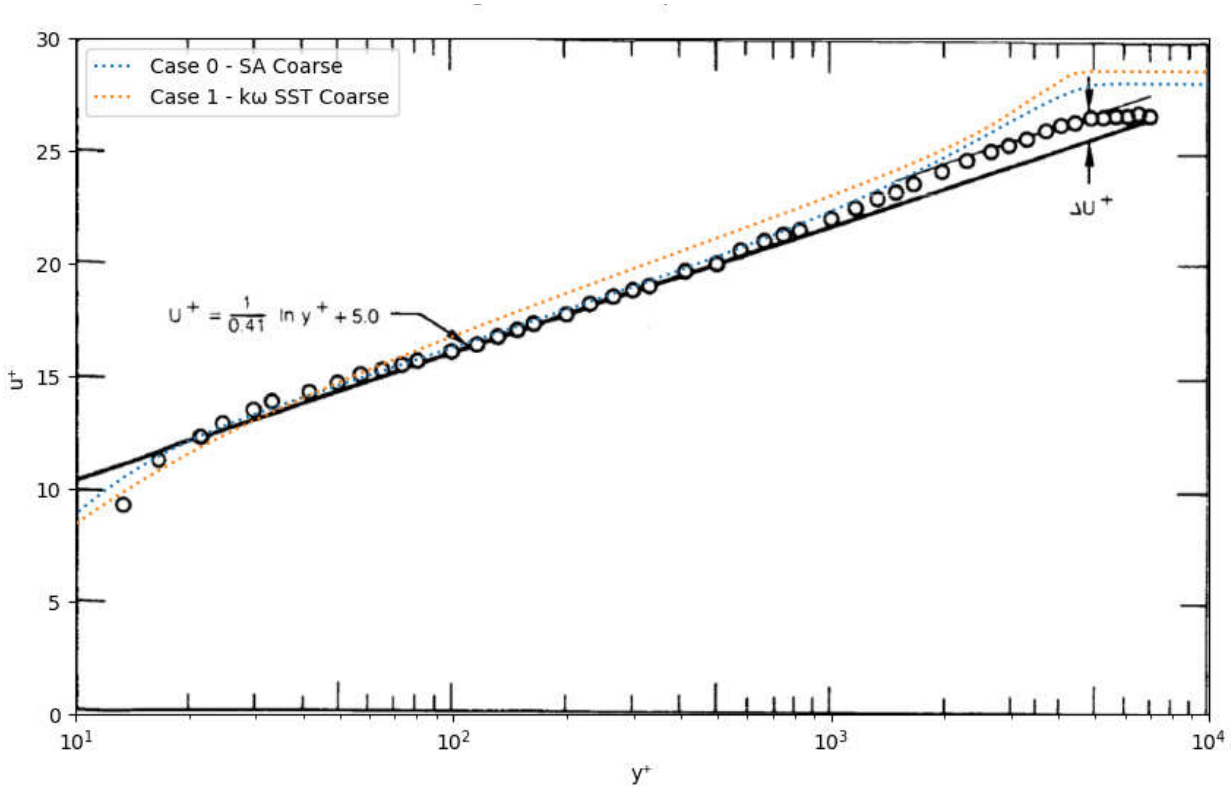

Figure 5.13: Inlet Flow Profile Comparison. Patrick data, shown in circles, used from Figure 4-2a of [31]

Case No	C_f	% Difference from Patrick	% Difference from Coles
0	$2.56e-3$	-4.26	-0.14
1	$2.46e-3$	-7.96	-4.00

Table 5.2: CFD Inlet Case Skin Friction Coefficients and Comparison to Patrick's Measured Data and Coles' Theoretical Data

Case No	H	% Difference from Patrick	% Difference from Coles
0	1.29	2.05	-1.82
1	1.30	1.49	-2.36

Table 5.3: CFD Inlet Case Shape Factor and Comparison to Patrick's Measured Data and Coles' Theoretical Data

Next, the mean behavior of the flow can be expressed by the coefficient of pressure at the wall, displayed in Figure 5.14. During the separation bubble, the RANS models diverge from each other as to what the pressure distribution should be. Given that in Case 1, the $k-\omega$ SST model case, the pressure distribution is more correct, this represents an improvement that the SST formulation provides the model. Both models show differences in the separation and re-attachment. The separation pressure distribution difference is not significant, only being premature and having the same slope, but the re-attachment is extremely different. The RANS cases show a premature re-attachment and then negative pressure value. It is possible, but also unlikely, that the outlet pressure boundary conditions could be causing this, but even with errors in the methods, it should not result in this drastic of behavior. Instead, it is more likely, going back to Figure 5.11, that the pressure behavior going into the outlet section of the duct is not well-formulated and results in this behavior, if it is due to the pressure behavior. The pressure boundary condition should be formulated as in Appendix C to compensate. Additionally, and most likely, this is a 2D steady CFD, where as turbulence is a 3D unsteady phenomena, with turbulent structures have 3D shapes. There is a simple test to prove the transient contribution. The same CFD analysis can be done with an unsteady method. If the separation/reattachment behavior is time-dependent, the distribution of location for separation/reattachment throughout time should have a non-Gaussian distribution, potentially with some skew. It is almost inevitable that the spanwise dimension, not represented

here, strongly affects the behavior, but this contribution is not strongly captured by the RANS models. To this end, there is nothing left to do but perform a 3D simulation.

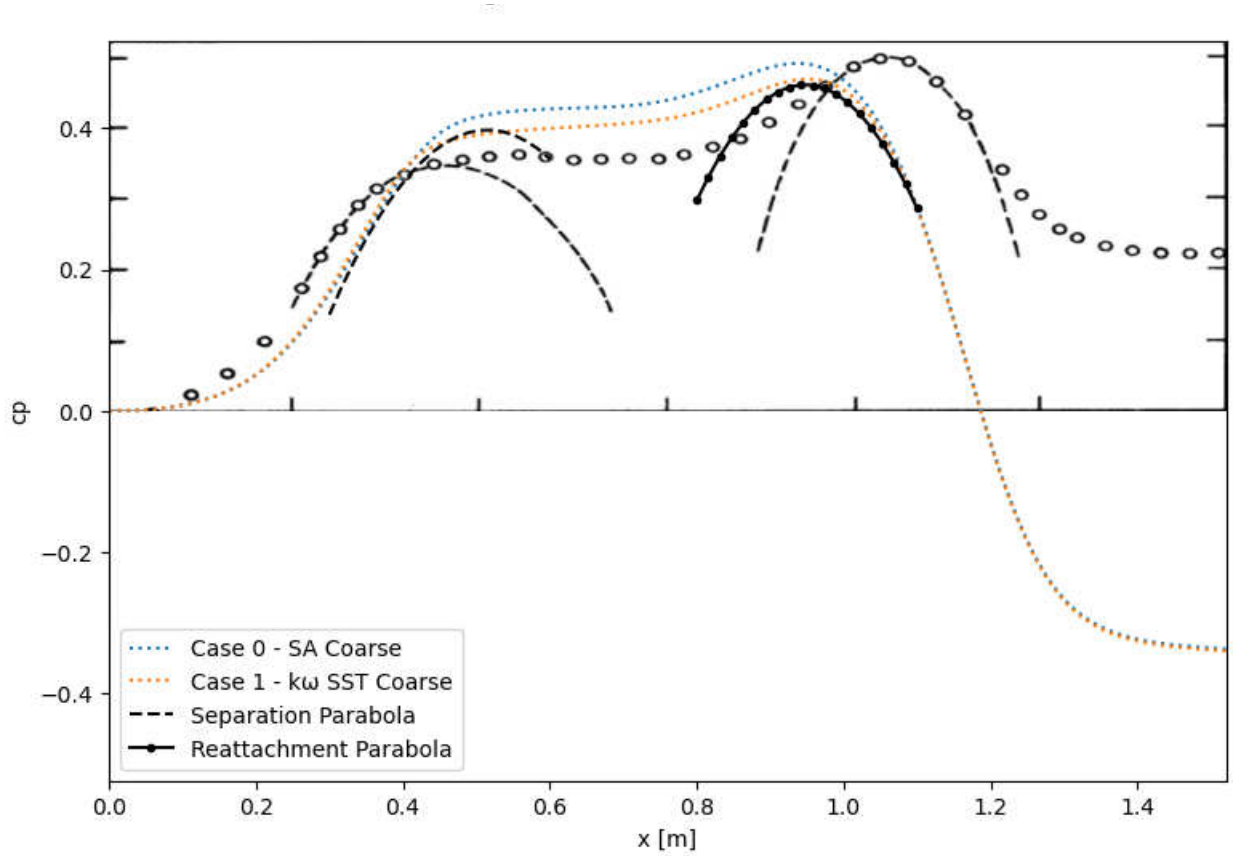

Figure 5.14: Flat Plate Pressure Coefficient Comparison. Patrick data used from Figure 4-7 from [31].

The shear behavior of the wall is also important, and emphasizes the issues with the reattachment, as seen in Figure 5.15. The two RANS cases are in strong agreement into the separation bubble with the experimental data, then as it reattaches, the discrepancy begins. The reattachment is premature, and exaggerated troughs and peaks. Given the agreement between the RANS models, it is likely not a model issue, but the application of the models. Additionally, this is more evidence that the RANS models model leading to and beginning separation.

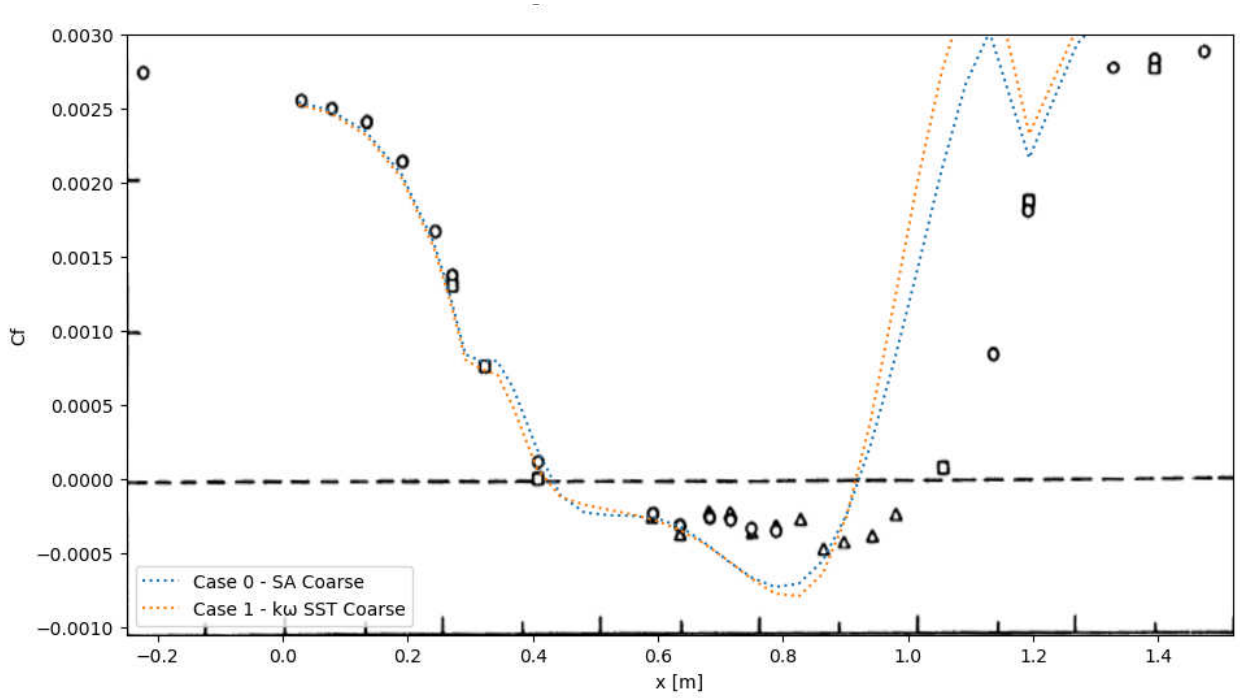

Figure 5.15: Flat Plate Skin Friction Coefficient Comparison. Patrick data used from Figure 5-7a from [31]

One of the largest behaviors of separation that is of interest is the separation bubble and the velocity profiles as they pass through the separation bubble. A selection of rakes that show the velocity profile are in Figure 5.16. The first thing that stands out is that the curve of zero-streamwise velocity is more subdued than Patrick's measured data would suggest. This is odd since the initial separation is in good agreement with Patrick's data. Moving out from the plate, the other observation is that the peak velocity is much closer to the plate than in Patrick's data. In Patrick's data the maximum velocity is very close to the opposing walls rather than the center of the flow profile. Given that the velocity profiles are in good agreement in the regions where viscosity dominates the behavior, this would indicate that there is a behavior in the CFD models that is causing the wake region to deviate from the proper behavior.

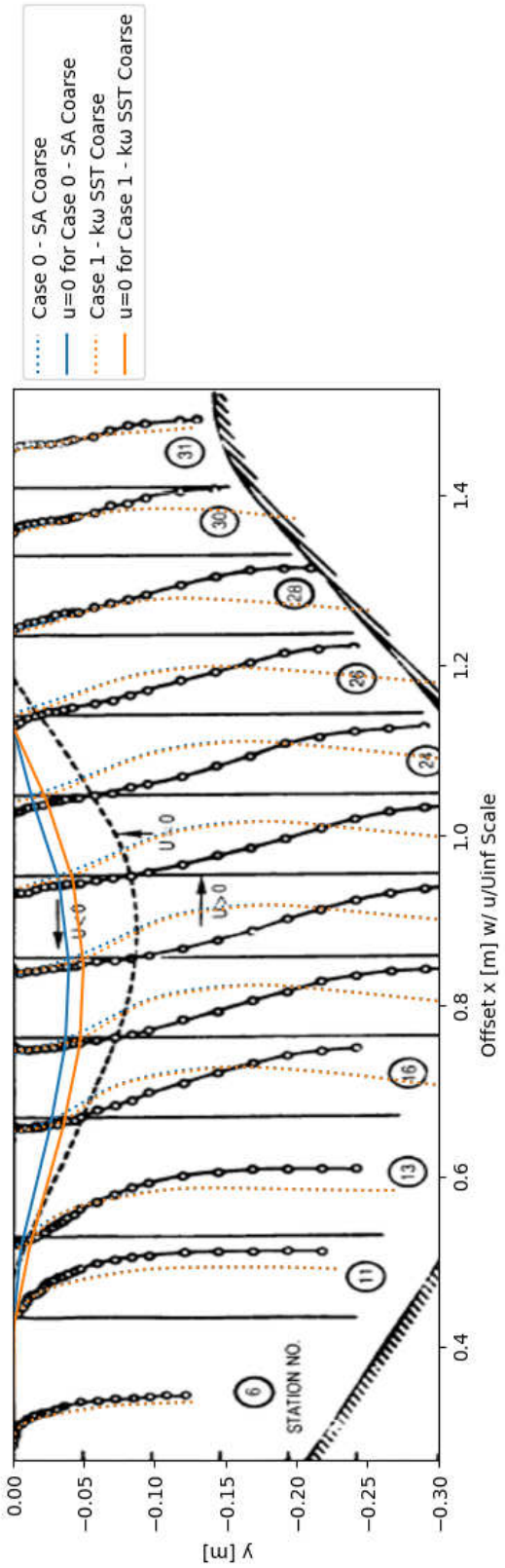

Figure 5.16: Flow Profiles Comparison for Rakes 6, 11, 13, 16, 18, 20, 22, 24, 26, 28, 30, and 31. Patrick data used from Figure 5-4 from [31].

The most helpful figure that describes what is happening is Figure 5.17. The relation of the two shape factors is what Patrick uses to compare the separation phenomena. The separation follows the previous data well, but stops short of the full separation, limited by the top curve that is well-supported by other experimental data. This indicates that the RANS modeling is not leading to the full separation behavior that would be expected.

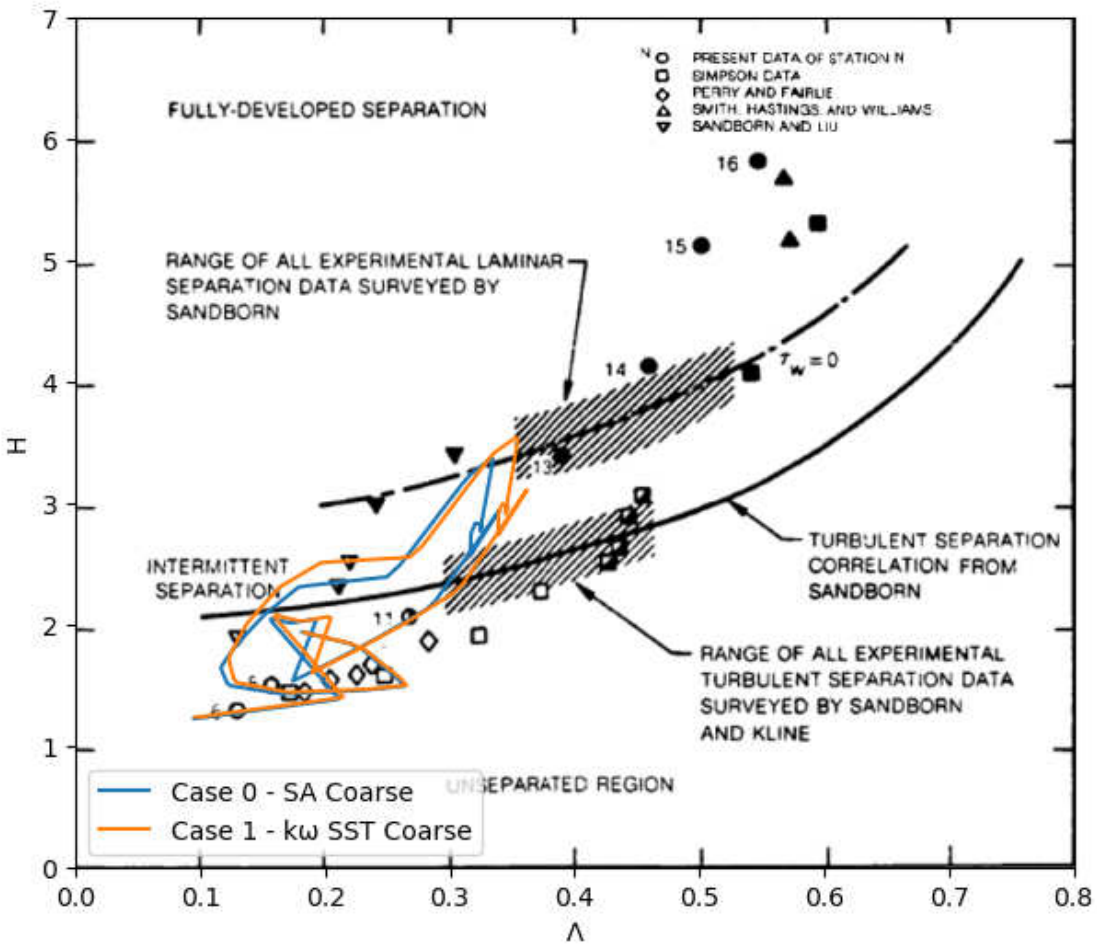

Figure 5.17: Comparison of Shape Factors as Correlated with Separation & Reattachment Phenomena

The transverse velocity profiles, as in Figure 5.18, reveal more issues with the behavior. The profile near the wall does not agree with the experimental data going into separation, but does during and after the premature reattachment.

Finally, it is helpful to see where the strength of the mechanisms behind separation are. The

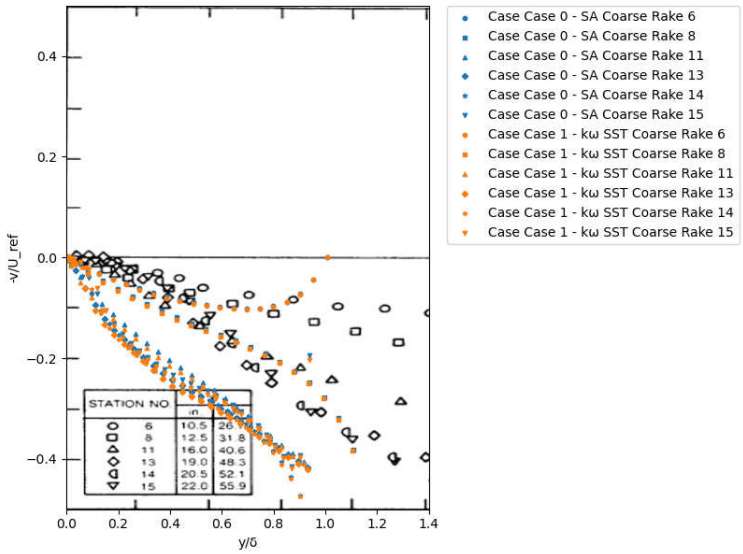

(a) Into Separation. Patrick data used from Figure 4-11a from [31]

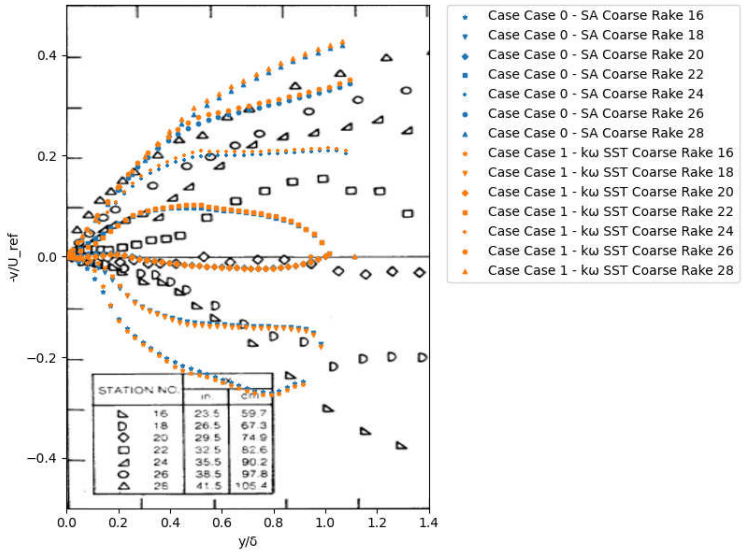

(b) During and After Separation. Patrick data used from Figure 4-11b from [31]

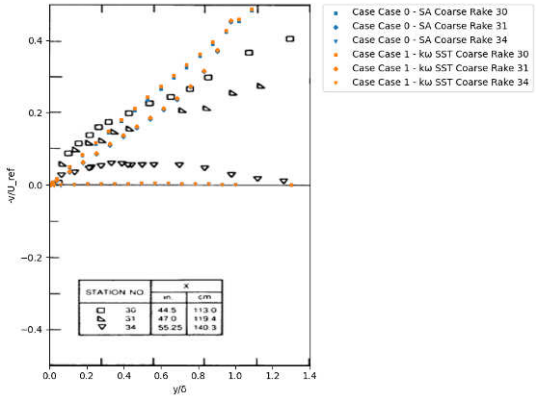

(c) After Separation. Patrick data used from Figure 4-11c from [31]

Figure 5.18: Transverse Velocity Profile Comparisons for Selected Measurement Stations

Clauser parameter is plotted for the streamwise direction in Figure 5.19. Prior to separation, the Clauser parameter is very strong. A reliable peak, based on the smoothed trend with a 20-span averaging filter, is about 100-200, which means that thus study produces Clauser parameters much larger than the literature studied previously.

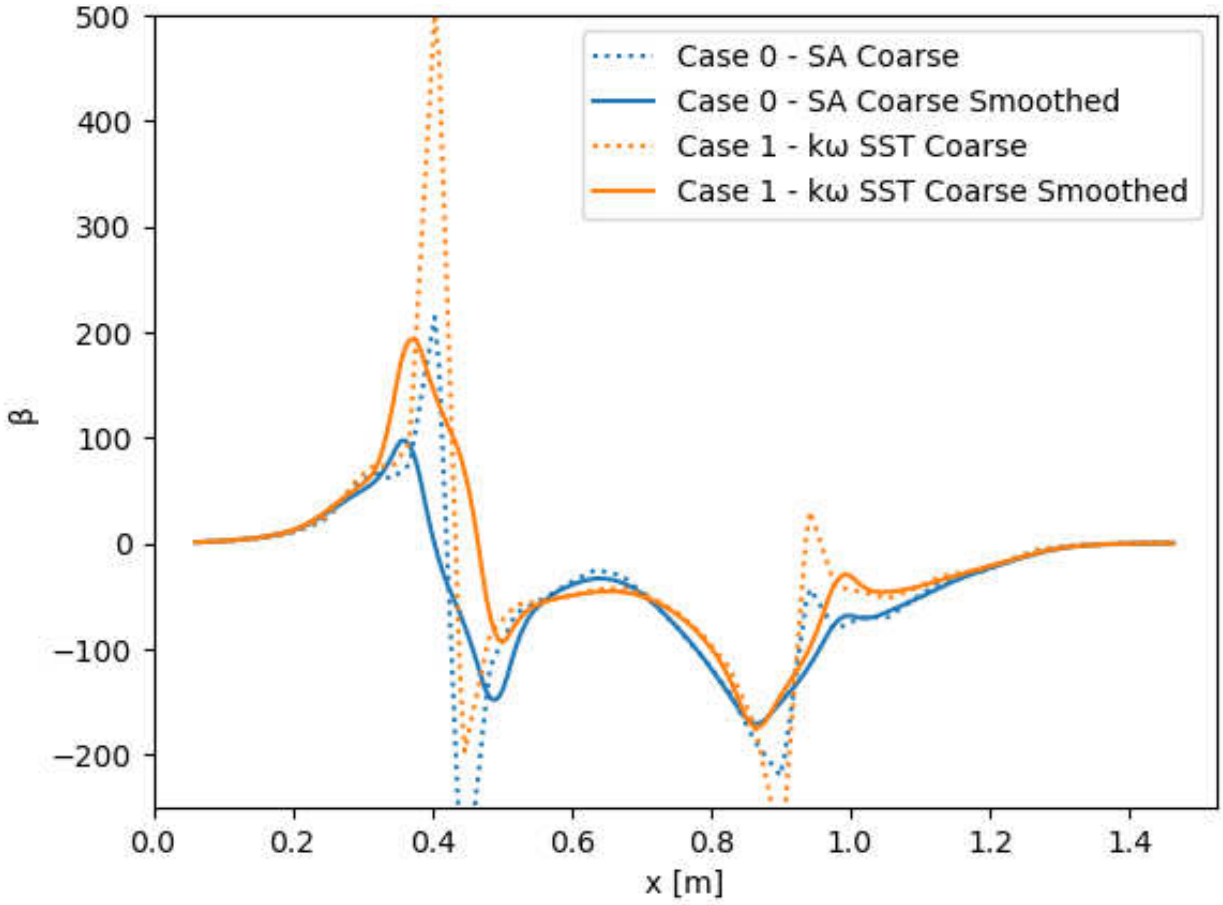

Figure 5.19: Clauser Parameter Profile Down Streamwise Direction

CHAPTER 6: SO AND MELLOR TEST SECTION

The Curved Duct analyses are done in six (6x) cases that are outlined in Table 6.1.

Refinement	SA Model Cases	$k-\omega$ SST Model Cases
Coarse	0	1
Medium	2	3
Fine	4	5

Table 6.1: Cases Used for the Patrick Duct Analyses.

6.1 Residuals

The residuals indicate that for all mesh refinement levels, the 2D steady RANS model is struggling to come to a resolution on the model. For the SA model cases, in Figures 6.1, 6.2, and 6.3, the model is working on resolving the pressure field as the turbulence model is solving quickly alongside the velocity and momentum. For the $k-\omega$ model cases, in Figures 6.4, 6.5, and 6.6, it is a similar issue, although it appears that for these cases, the residuals may level out before a solution.

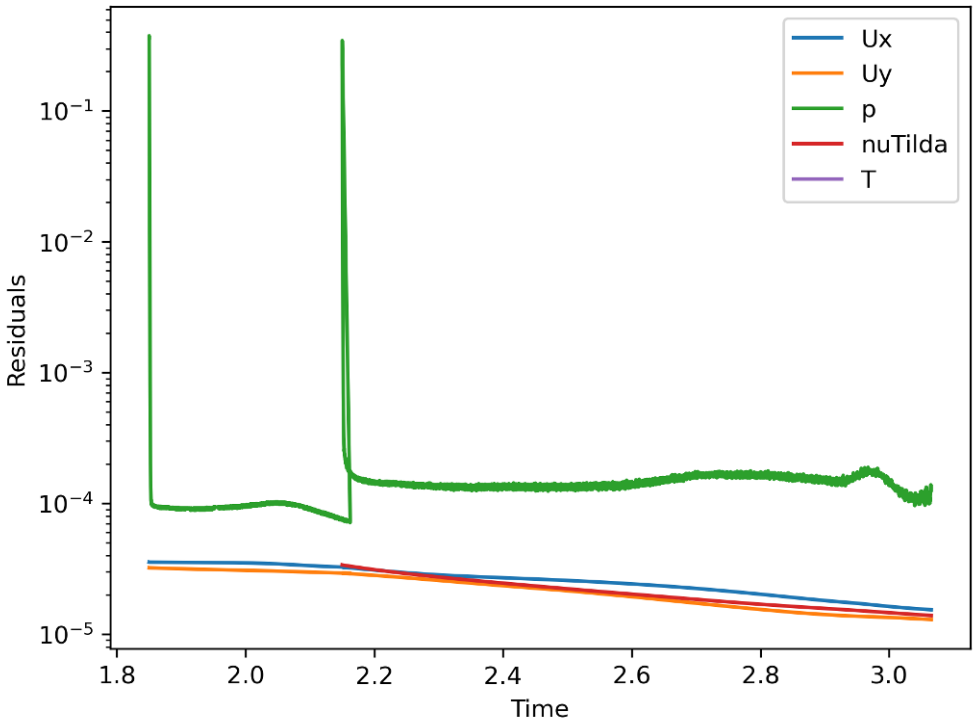

Figure 6.1: Residuals for Case 0

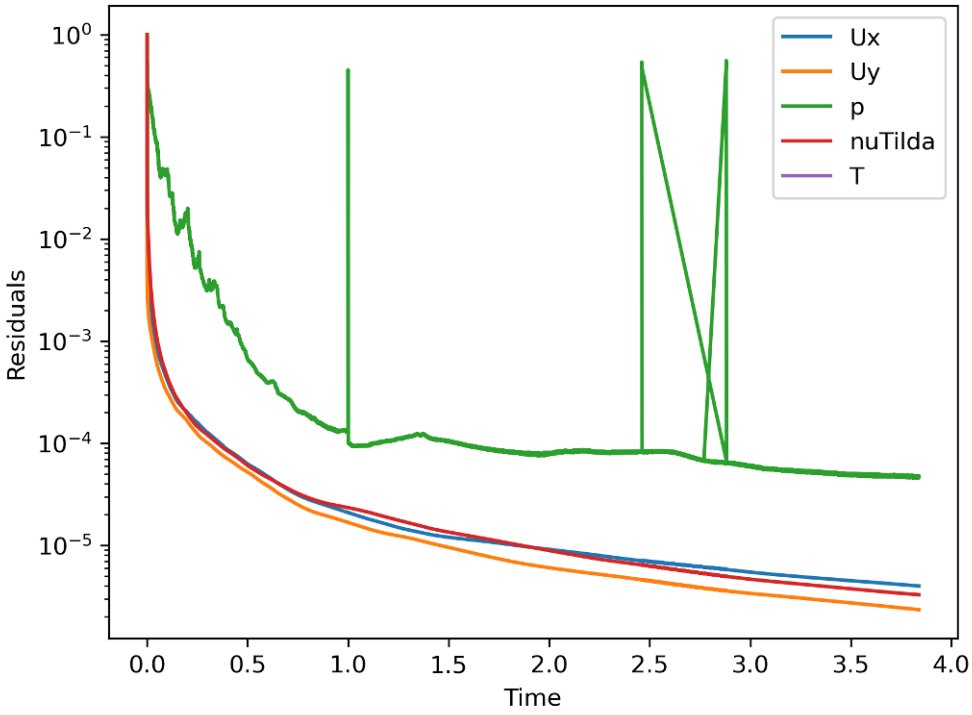

Figure 6.2: Residuals for Case 2

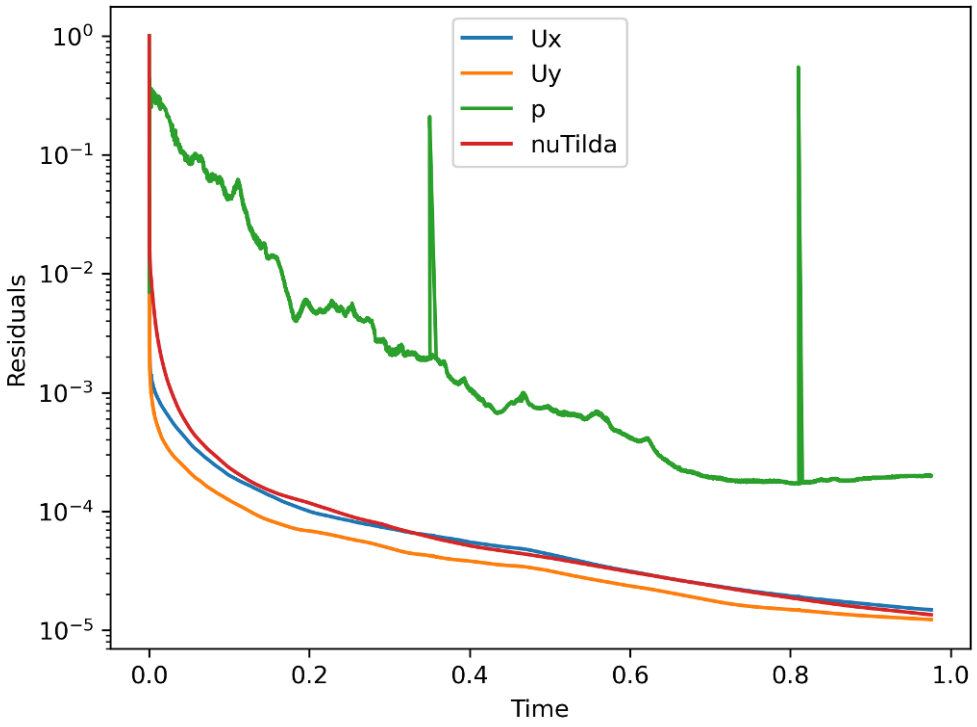

Figure 6.3: Residuals for Case 4

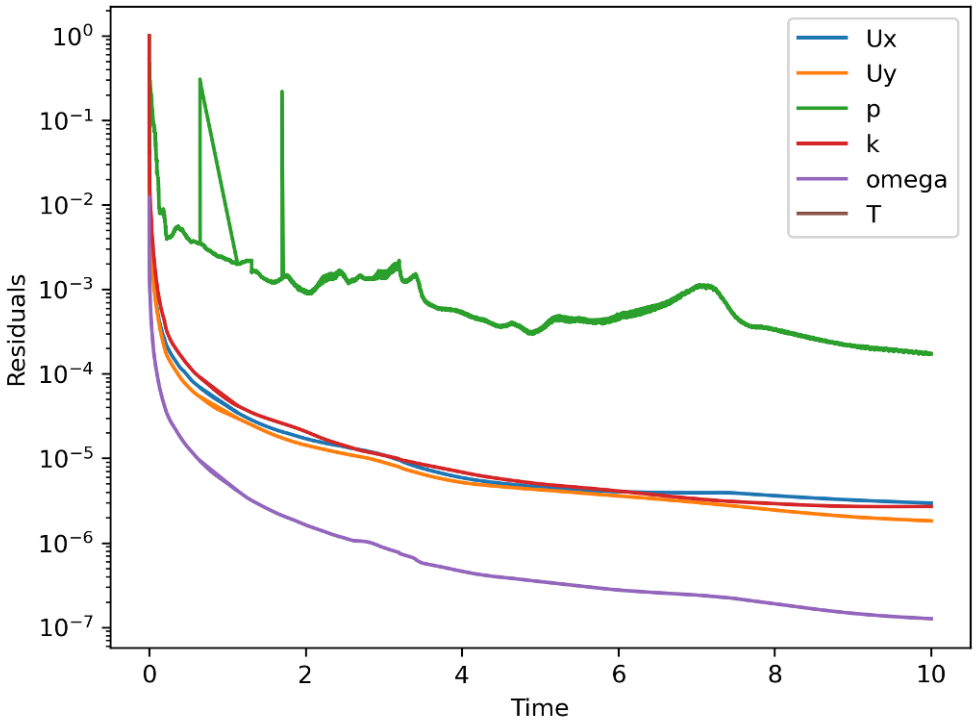

Figure 6.4: Residuals for Case 1

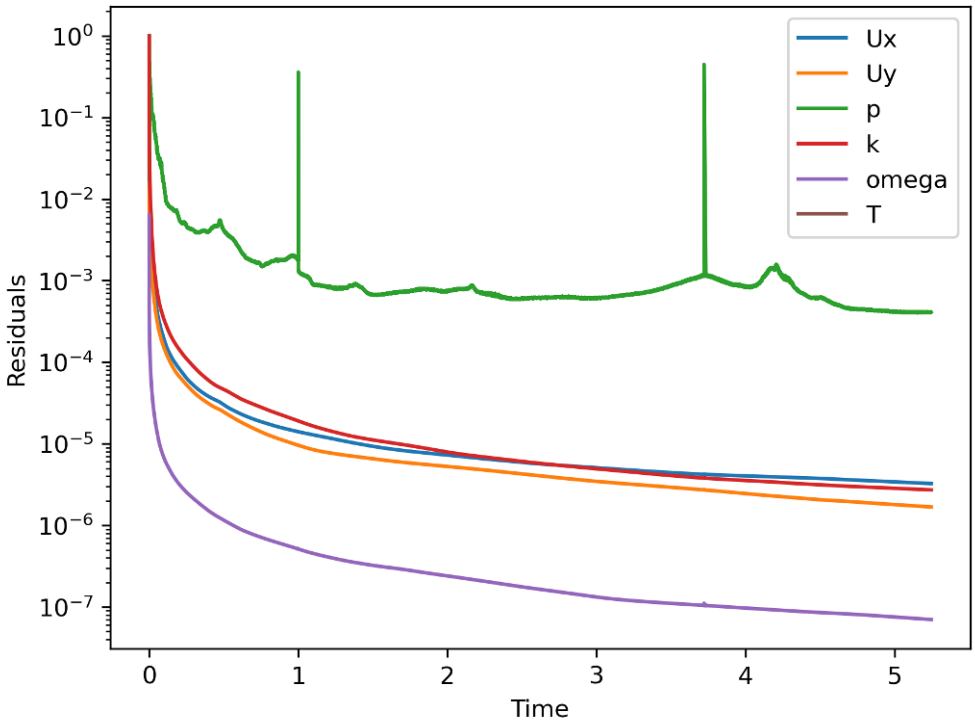

Figure 6.5: Residuals for Case 3

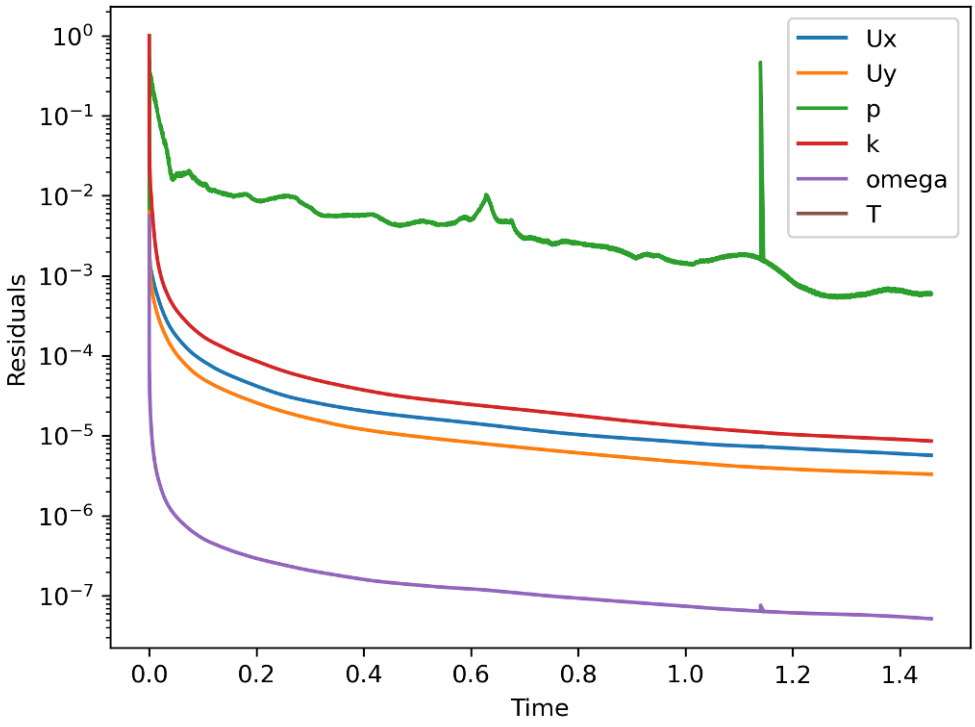

Figure 6.6: Residuals for Case 5

6.2 Contour Plots

Note that the following cases have not been completed yet. The strong effect of curvature on a separating boundary layer is apparent in this geometry. The boundary layer is well-attached to the walls up to a point as it travels over the curve, where it separates, which can be seen in Figure 6.7. After separation, there are clearly strong eddies that form as the flow exits the duct. This is where the CFD is still creating a solution.

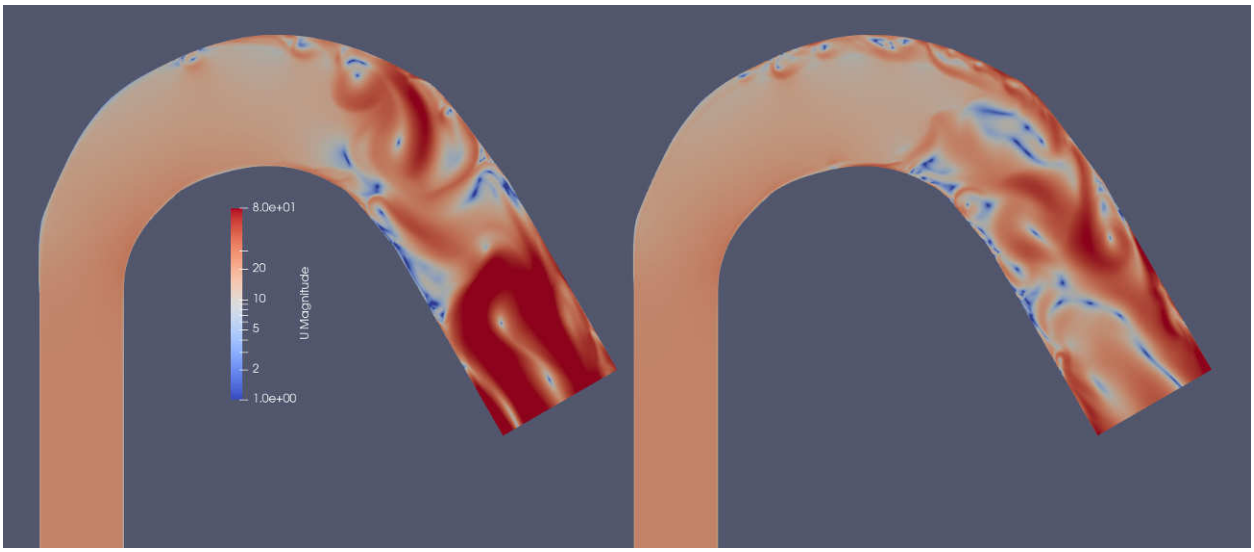

Figure 6.7: Velocity Magnitude for Cases 0 and 1.

Looking at the pressure field, it is apparent that the CFD is still working on a solution, as seen in Figure 6.8. There is a strong negative pressure zone or zones near the outlet of the duct.

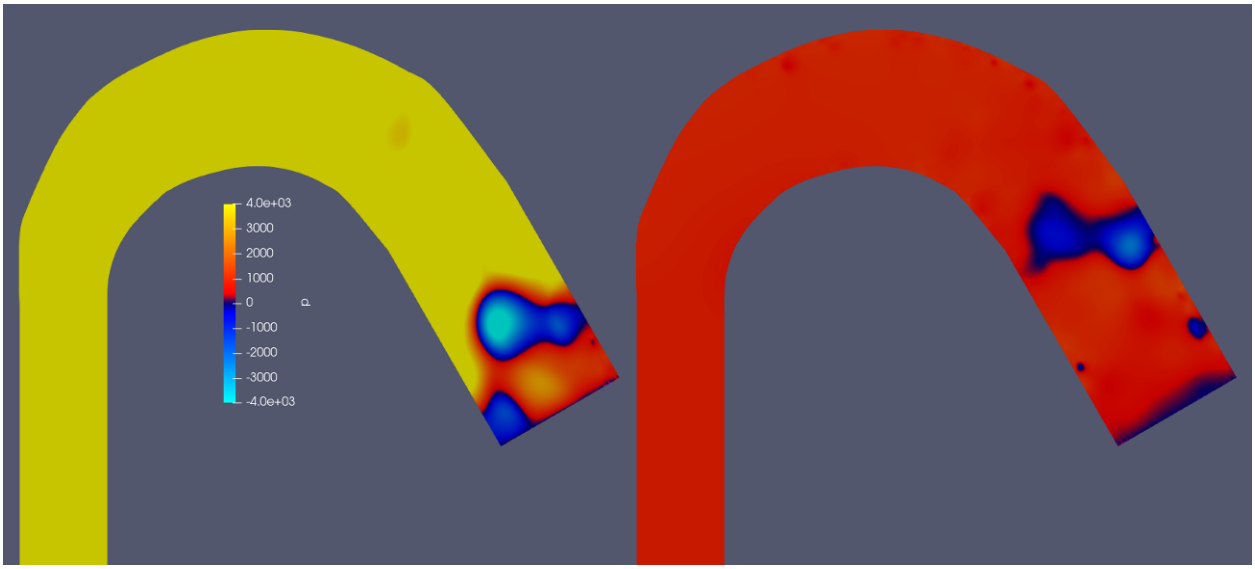

Figure 6.8: Pressure for Cases 0 and 1.

The turbulence picks up as the flow passes over the curved surfaces, as is shown in Figure 6.9. The turbulence then advects towards the outlet. The generation appears to be very strong compared to the dissipation, shown for Case 1 in Figure 6.10 alongside the modified viscosity for Case 0.

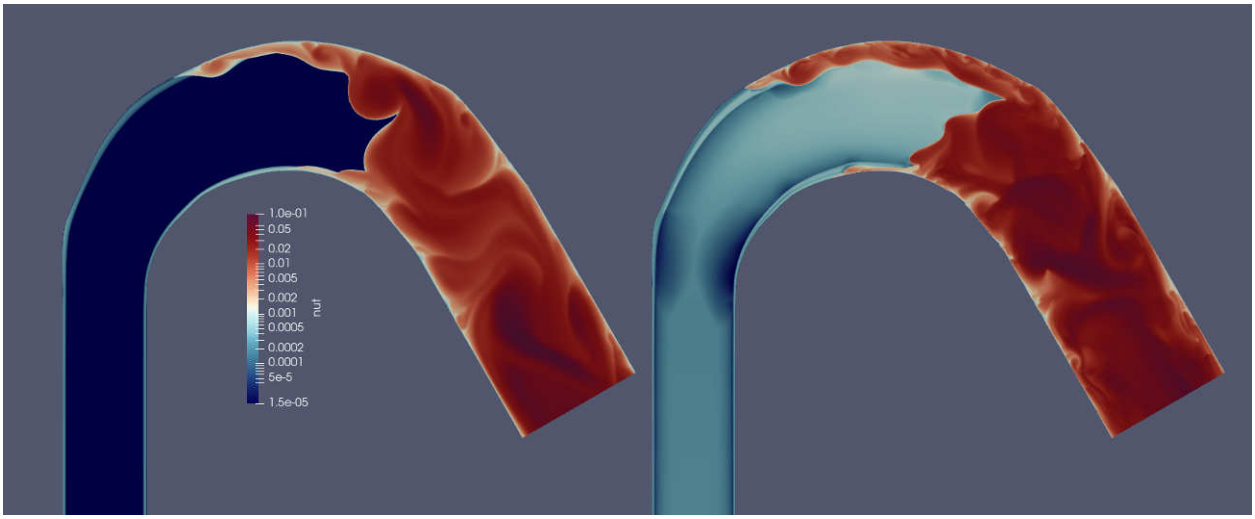

Figure 6.9: Turbulent Viscosity for Cases 0 and 1.

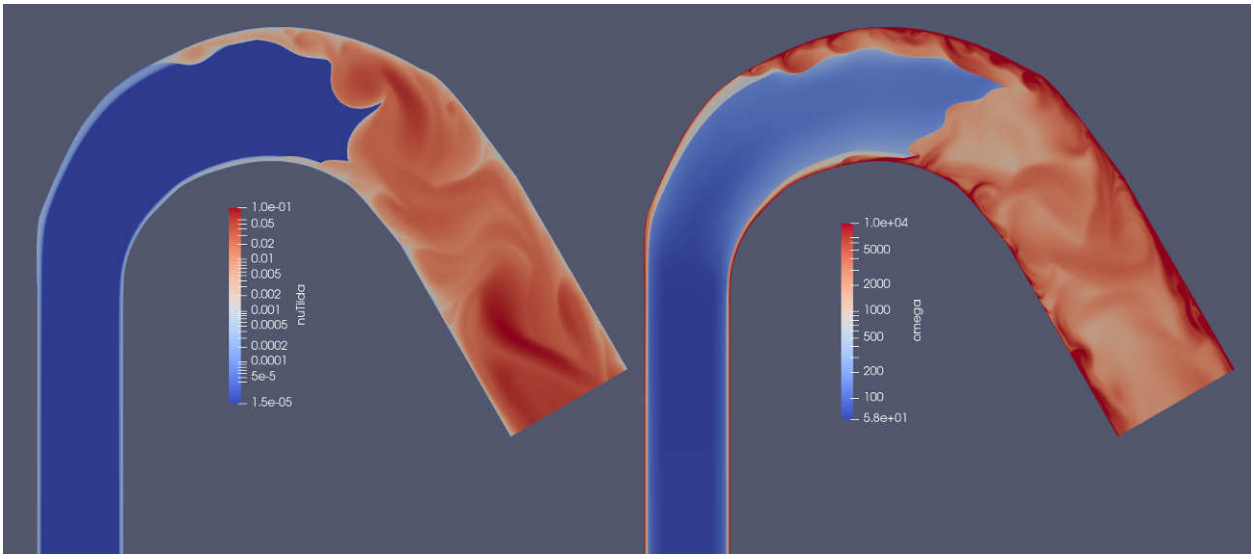

Figure 6.10: Turbulence Dissipation for Case 1 on the Right.

Finally, it appears that the turbulence generation is impeding the transport of the passive scalar, shown by temperature in Figure 6.11. This is likely that the scalar has dissipated, thus the wall temperature is dominating.

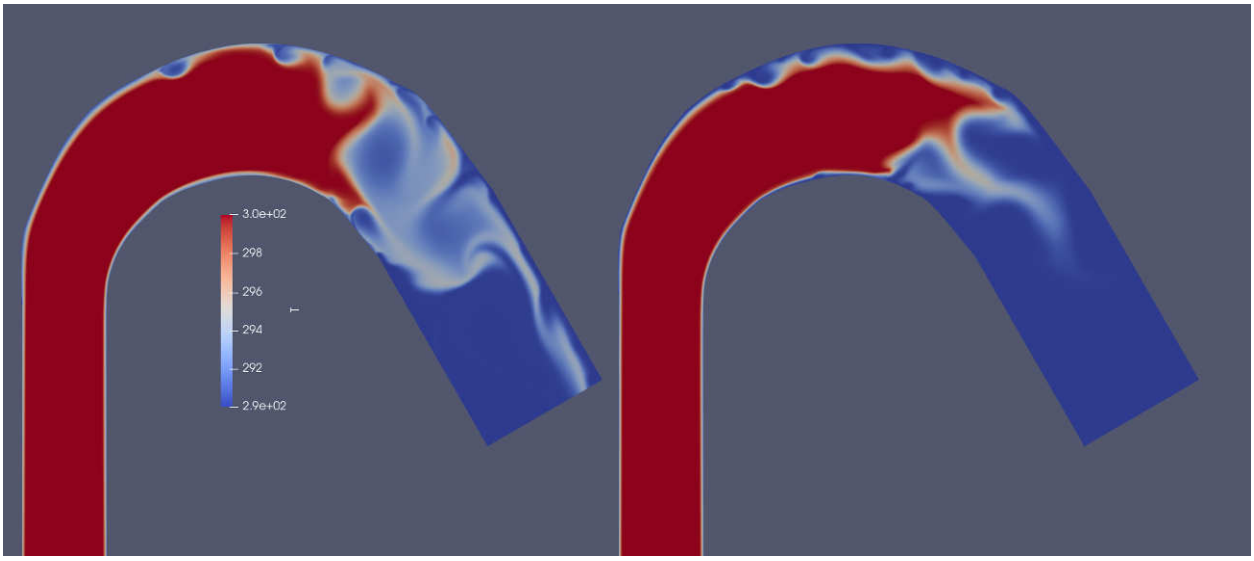

Figure 6.11: Temperature for Cases 0 and 1.

CHAPTER 7: CONCLUSIONS AND FUTURE WORK

7.1 From the Setup and Methods

Overall, OpenFOAM is shown to scale well. The optimum target is 100,000 points per MPI rank for performance, but there are issues with scaling to large analyses since the decomposition and reconstruction are serial processes. OpenFOAM overall provides a variety of options to flexibly study PDE's, or ODE's, in domains to a variety of applications. The built-in CFD solver could do with some external patches and improved order of accuracy, but provides a good baseline for this project.

In general, the passive scalar transport works as expected,

7.2 From the Flat Plates

In the case of the smooth, ZPG conditions, the turbulence models generally follow a good boundary layer development trend that is expected based on canonical data. Across data from multiple sources and experiments, the CFD as set up is producing a good boundary layer to draw data from. The outer regions for RANS do appear to behave differently than expected, which results in what appears to be an underdeveloped boundary layer height relative to the momentum boundary layer height. However, this may be due to the analysis being a duct rather than a true flat plate. Finally, the inner regions of the boundary layer are verified to behave as expected and the mean flow has a high degree of accuracy to the canonical data.

7.3 From the Patrick Duct

The diverging-converging duct did separate the boundary layer on the flat plate as Patrick's 1987 study would suggest. The initial separation is in good agreement with the experimental data. However, the wake of the outer region of the boundary layer deviates from what is expected from the experiment and the separation bubble collapses early in the stream. The maximum velocity of

the profile is closer to the flat plate than the experimental data would suggest. When the flow recombines into the following near-ZPG condition, the velocity profile agrees with the experimental data better. Comparing the shape of the boundary layer, it became clear that this separation bubble never reaches a full separation and the 2D steady RANS only allows it to reach an initial separation state.

7.4 From the So and Mellor Duct

The 2D steady RANS models struggle to form a solution to the So & Mellor geometry and conditions. Based on this, strong normal stresses on the RANS models likely prevent a solution from forming for 2D steady analyses, and this may require a 3D or unsteady analysis to better understand the behavior.

This said, the results leading up to separation look promising, as the Patrick study also indicates that RANS models are sufficient for these conditions.

7.5 Future Work

There are a few next steps that are obvious. First, improving the pressure boundary condition via a better patch, as in Appendix C would help remove some of the inherent assumptions about pressure in the model. Second, moving to an unsteady analysis would indicate the influence of transient behavior on separation. Looking at the distribution of separation point and angle would indicate this influence. Third, it is advisable to look at a 3D geometry as turbulence is well-known to be a 3D phenomena with structures that take shape in the spanwise direction, as well as wall-normal and streamwise.

With this success, then better conculsions can be drawn from separation behavior. This would improve understanding of turbulent behavior by drawing correlations to things like mixing length to pressure gradient conditions. It is unlikely that it is the RANS models themselves that are causing issues, but the context they are used in.

APPENDIX A: EXPERIMENTAL DATA FOR RANS VALIDATION - ADDITIONAL SETUP INFORMATION

A.1 Original Studies

A.1.1 Patrick (1987)

One of the test RANS cases in this study corresponds to a wind tunnel test over a flat plate and an opposite diverging-converging wall. The wind tunnel was owned and operated by the United Technologies Research Center in East Hartford, Connecticut, and supported by NASA's Lewis Research Center, now the Glenn Research Center. Rather than going into depth on the tunnel that is illustrated in A.1 and described in detail in [31]. Some highlights of the design:

1. The temperature and air quality are controlled by the heat exchanger and HEPA filter, respectively.

2. The boundary layer is tripped from a laminar state to a developing turbulent state by the bar shown in Detail A. This will control the boundary layer as it travels into the test section.

3. The lower diverging wall is adjustable and has a boundary layer scoop to remove the effects of a duct flow to study purely the boundary layer on the top surface. The second scoop section was not used.

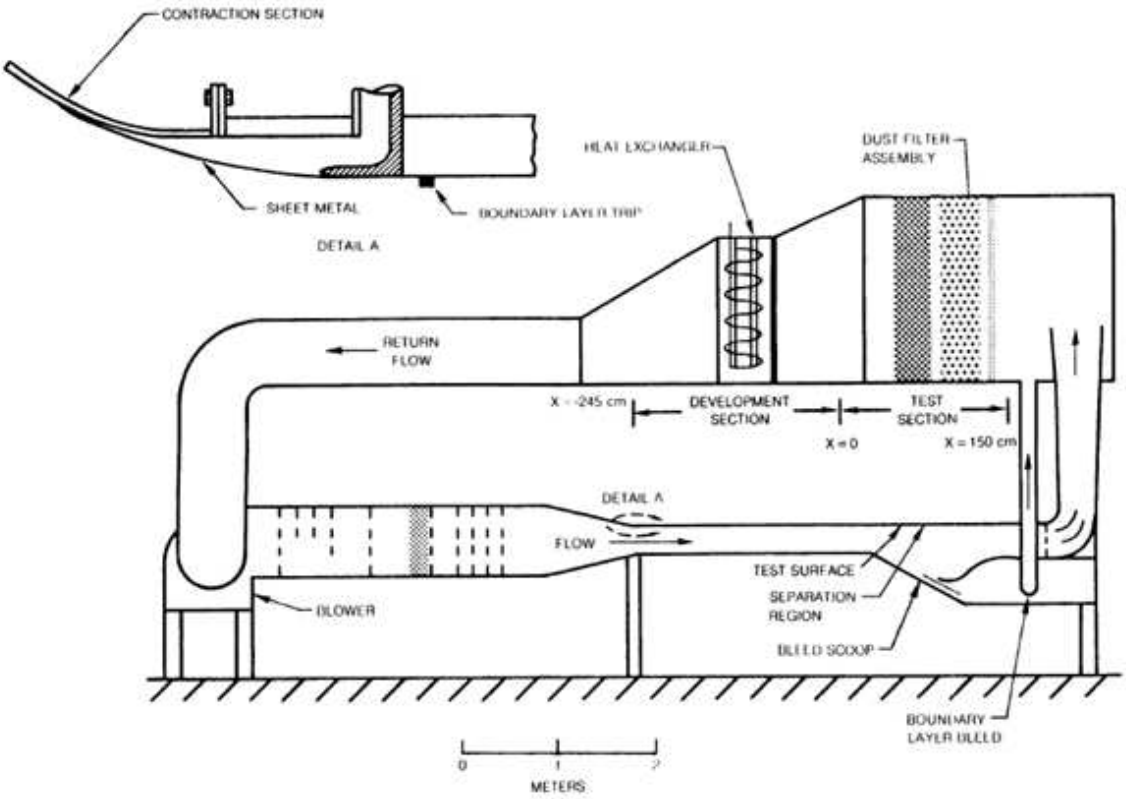

Figure A.1: Wind Tunnel Diagram. Originally Figure 3-2 from [31].

4. The test section is equipped with the following instrumentation:

Quantity	Instrumentation
120	Static Pressure Taps
55	0.63cm dia Probe Ports

Table A.1: The Test Section Top Surface Instrumentation.

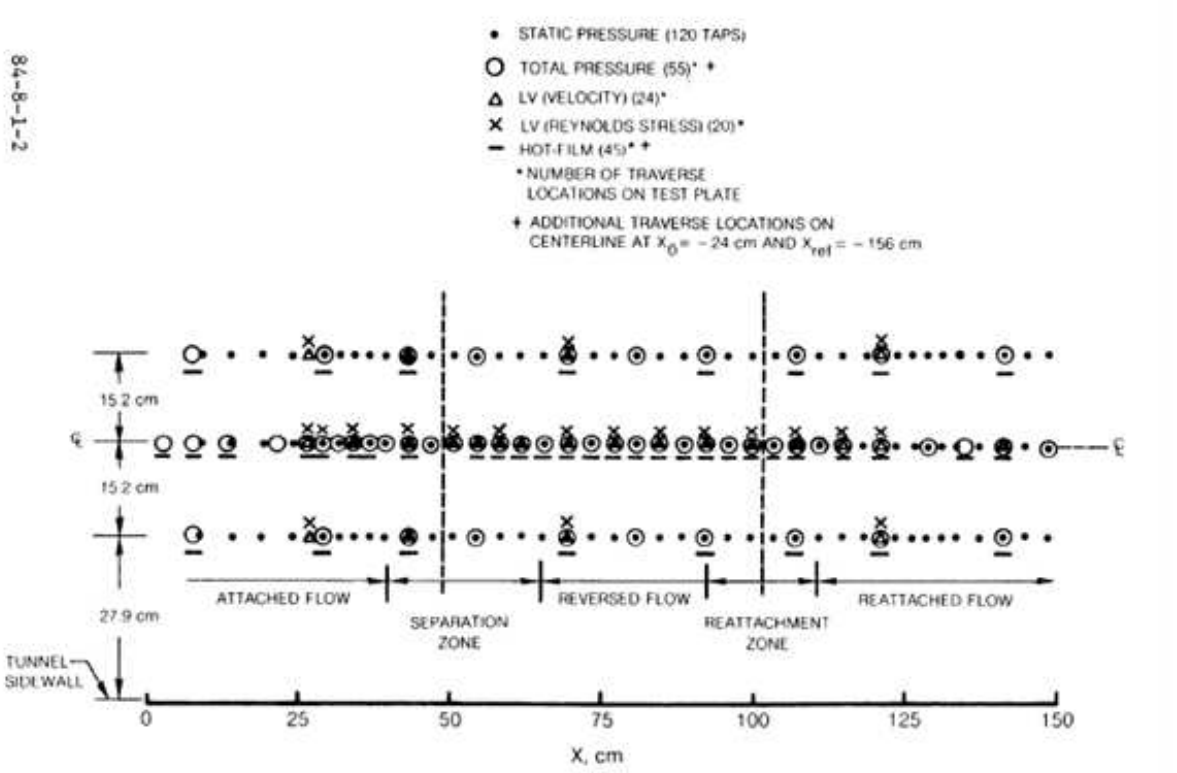

Figure A.2: Top Plate Instrumentation Placement. Originally Figure 3-7 from [31].

Quantity	Instrumentation
20	Static Pressure Taps
20	0.63cm dia Probe Ports

Table A.2: The Test Section Bottom Surface Instrumentation.

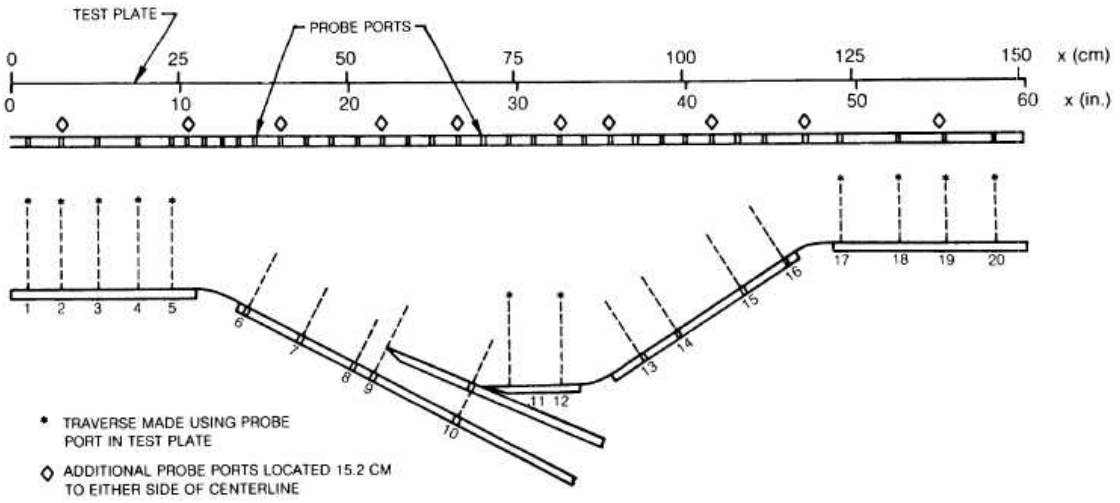

Figure 3-6 Probe Port and Lower Wall Traverse Locations (Test Section Centerline)

Figure A.3: Diverging Duct Instrumentation Placement. Originally Figure 3-6 from [31]. Probing points are along the centerline of the tunnel.

5. The instrumentation could be either hot wire or total pressure probes

6. Laser velocimetry measures the movement of the flow via suspended titanium dioxide powder.

7. The flow on the test flat plate was visualized via "tuft trees," which are tubing manifolds that inject a "red low-viscosity fluid".

8. The flow was measured as a two-dimensional (2D) flow with the following flow parameters calculated:

    - U
    - V
    - $\sqrt{\overline{u^2}}$
    - $\sqrt{\overline{v^2}}$
    - $\overline{uv}$

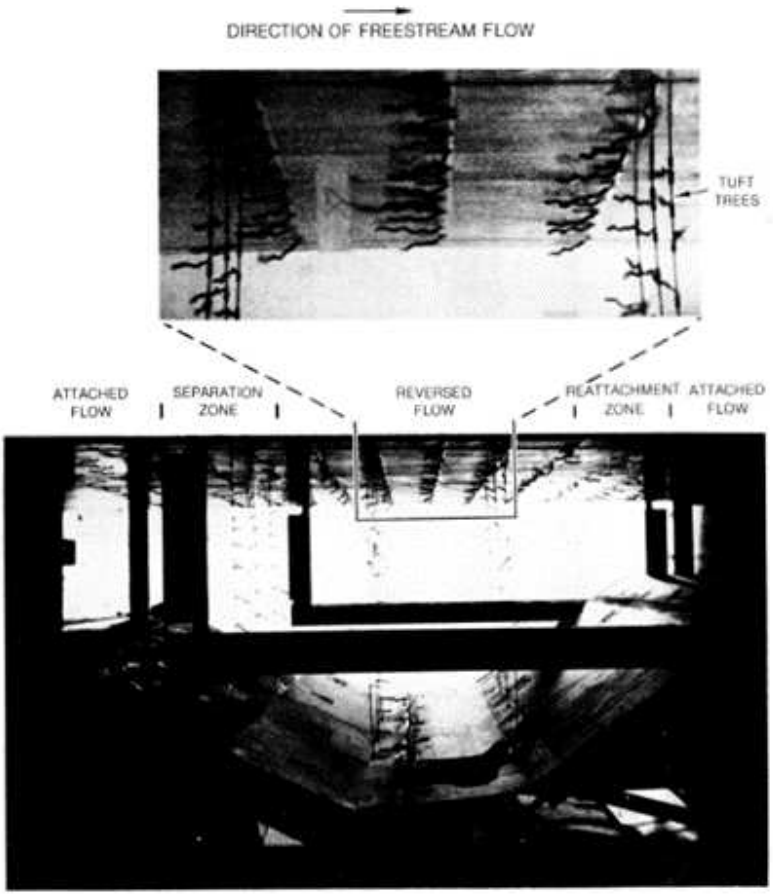

Figure A.4: Tuft Trees. Originally Figure 4-3 from [31].

9. The following conditions were measured during the study:

    - $Re_\theta = 11,400$
    - $V_{\text{inf},in} = 27[m/s]$
    - $T_{in} = 22.2[^\circ C]$
    - $P_{in} = 15.08[psia]$
    - $\delta = 76.7e-3[m]$

10. A form of flow resistance was between the outlet turning guide vanes and the filter inlet plenum seen in A.1. This generated a 22.9 cmH_2O pressure difference between the filter inlet plenum and the outlet of the test section. For the sake of this study, the pressure difference between the filter inlet plenum and the boundary layer bleed scoop out let will be zero.

Based on the measurements of the experiment, there is a streamline that separates the flow bounded by the flat plate from the flow that is opposing this flow and bounded by the walls on the opposite side, illustrated in A.3. This allows for a more informed splitting of the test section CFD domain, which will provide better mesh quality and geometry creation.

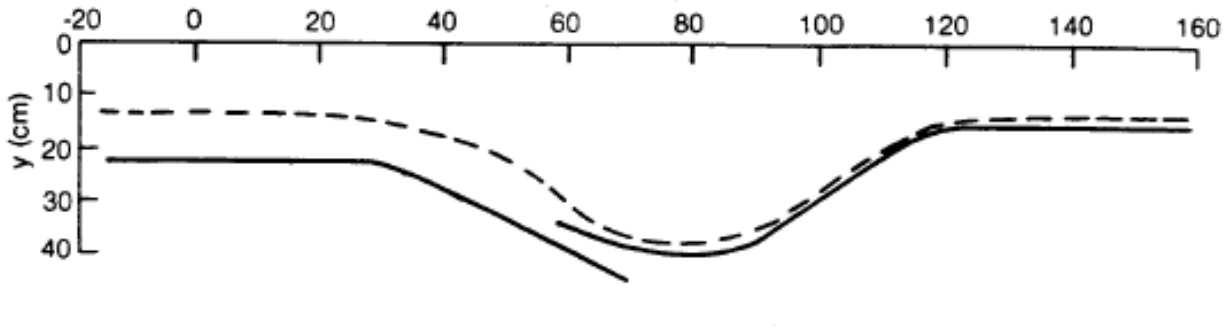

Figure A.5: Midstream Separating Flat Plate-Bounded Flow from Opposing Flows. Originally Figure 4-23 from [31]

STATION NO.	x (cm)	y (cm)
1L	-22.86	13.08
2L	2.54	13.34
3L	7.62	13.46
4L	13.34	13.56
5L	17.78	13.69
6L	37.62	17.58
7L	47.52	21.95
8L	57.63	28.35
9L	58.85	32.74
10L	69.62	37.57
11L	75.57	38.02
12L	82.55	37.34
13L	92.96	34.06
14L	98.43	30.05
15L	106.40	24.69
16L	111.51	21.54
17L	133.99	14.71
18L	140.97	14.76
19L	146.05	14.76
20L	151.13	14.73

Table A.3: Points of Midstream Separating Flat Plate-Bounded Flow from Opposing Flows. Originally Figure 4-23 from [31]

There is much more data that Patrick measured from the experiments. This data comes in both figure and tables that are contained in «PATRICK DATA APPENDIX».

A.1.2 So and Mellor (1972)

The focus of So and Mellor's study from 1972 is turbulent boundary layer development and separation over specifically curved surfaces. Their study is a follow-on to Schmidbauer (1936) [33], Schneider and Wade (1967), Patel (1968b) [30], and Gortler (1940), all of which studied turbulent boundary layer development over curved surfaces. There were others in the literature review, but the authors pointed out issues with those studies not mentioned here.

So and Mellor built a wind tunnel to perform the study on with lower curvature surfaces than many of the previous studies they reviewed. In their study, the convex surface had a normalized

curvature of $\frac{\delta^*}{R} = 0.010$, and the concave surface had a normalized curvature of $\frac{\delta^*}{R} = 0.007$. Again, rather than going in depth on the experimental setup, illustrated in Figure A.6 and described in detail in [41], here are the highlights:

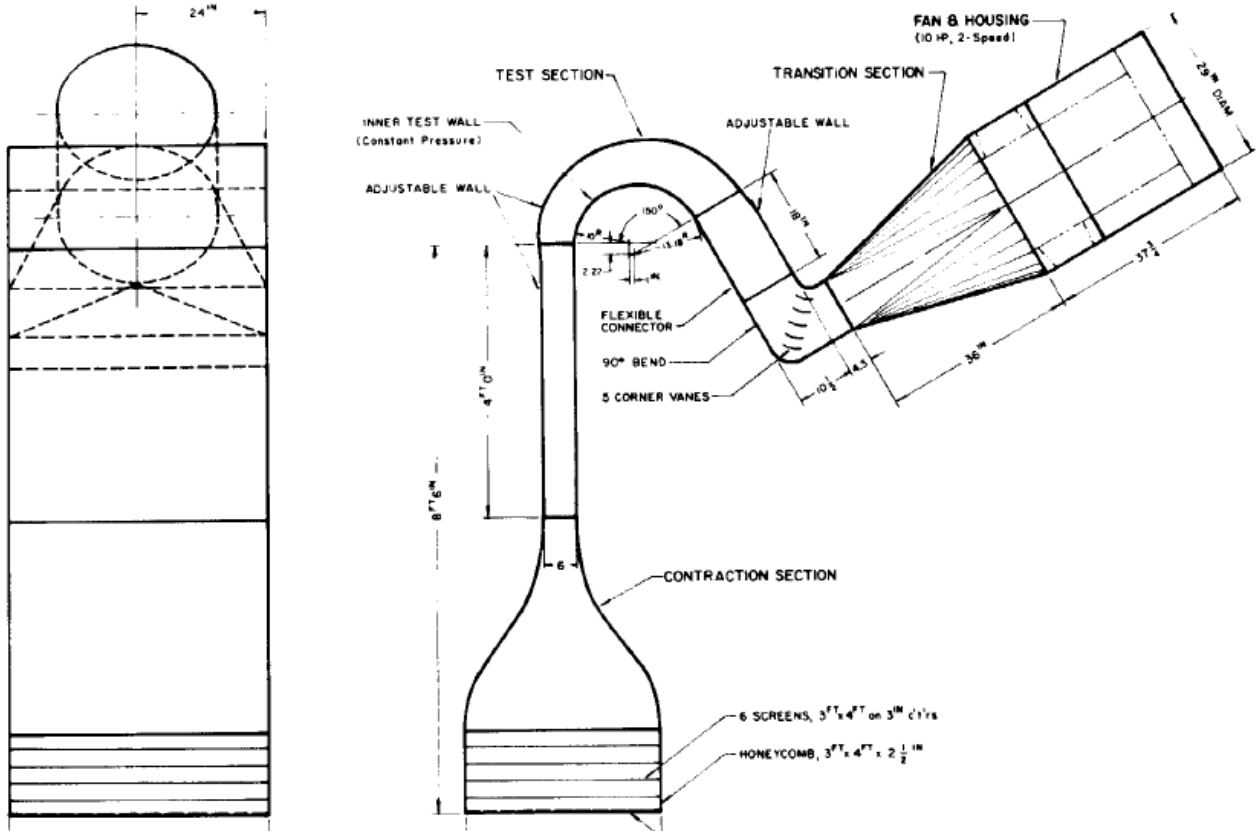

Figure A.6: Wind Tunnel Diagram. Originally Figure 1 from [41].

1. The inlet conditions are taken from the surroundings, which can be assumed ambient conditions.

2. The flow is collimated and then contracted into the straight inlet section.

3. The boundary layer was theoretically tripped to become turbulent with a piano wire. However, based on the figures So and Mellor present, like Figure A.7, it appears that it could have been the curvature or natural transition that caused it, which led to no analogous effect in the CFD

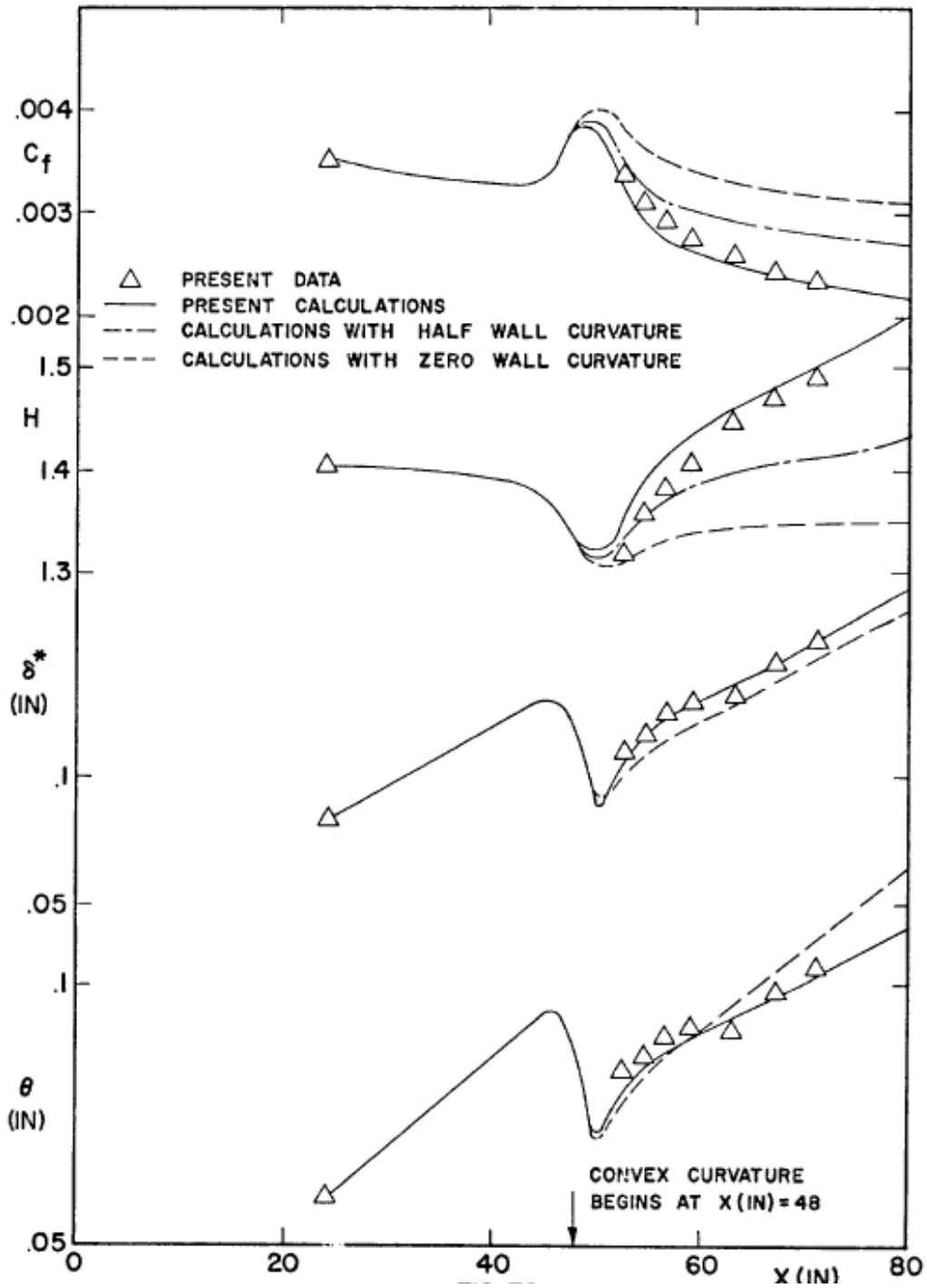

Figure A.7: Wind Tunnel Diagram. Originally Figure 79 from [41].

4. The curvature is normalized to the displacement boundary layer thickness to control the flow via its potential outside the boundary layer. The convex surface had a normalized curvature of $\frac{\delta^*}{R} =$

0.010, and the concave surface had a normalized curvature of $\frac{\delta^*}{R} = 0.007$. The displacement boundary layer thickness is calculated via Equation A.1. So and Mellor produced the curves that are drawn to scale in Figures A.8 and A.9.

$$\delta^*(x) = \frac{0.037x}{Re_x^{1/5}} \tag{A.1}$$

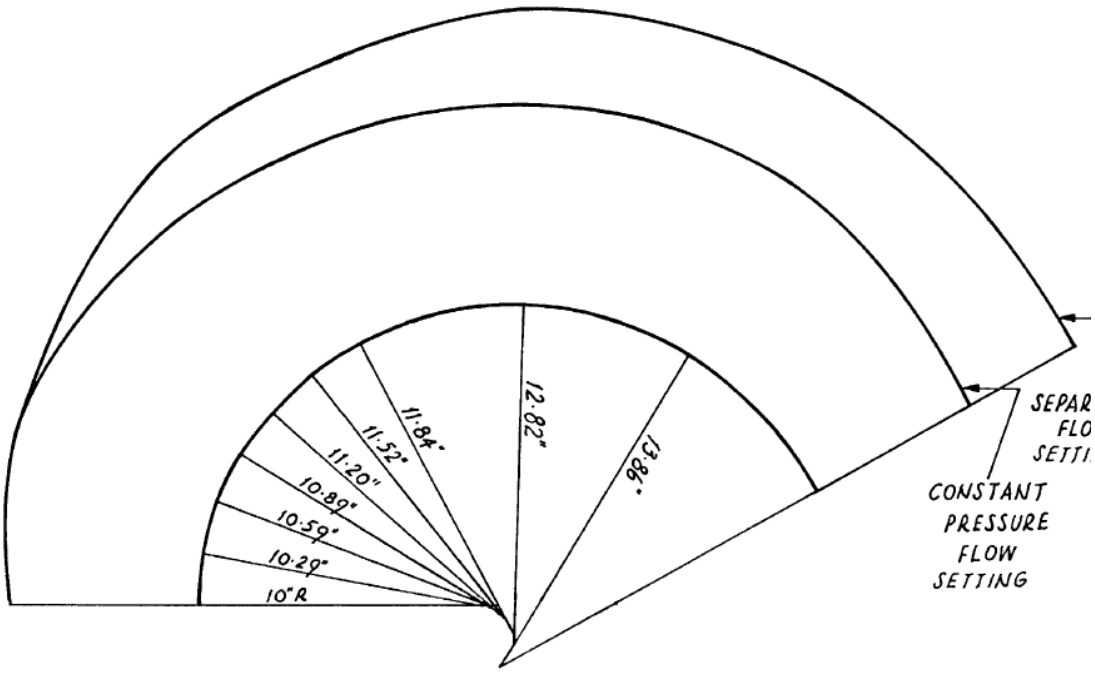

Figure A.8: So and Mellor Convex Curve. Originally Figure 3 from [41].

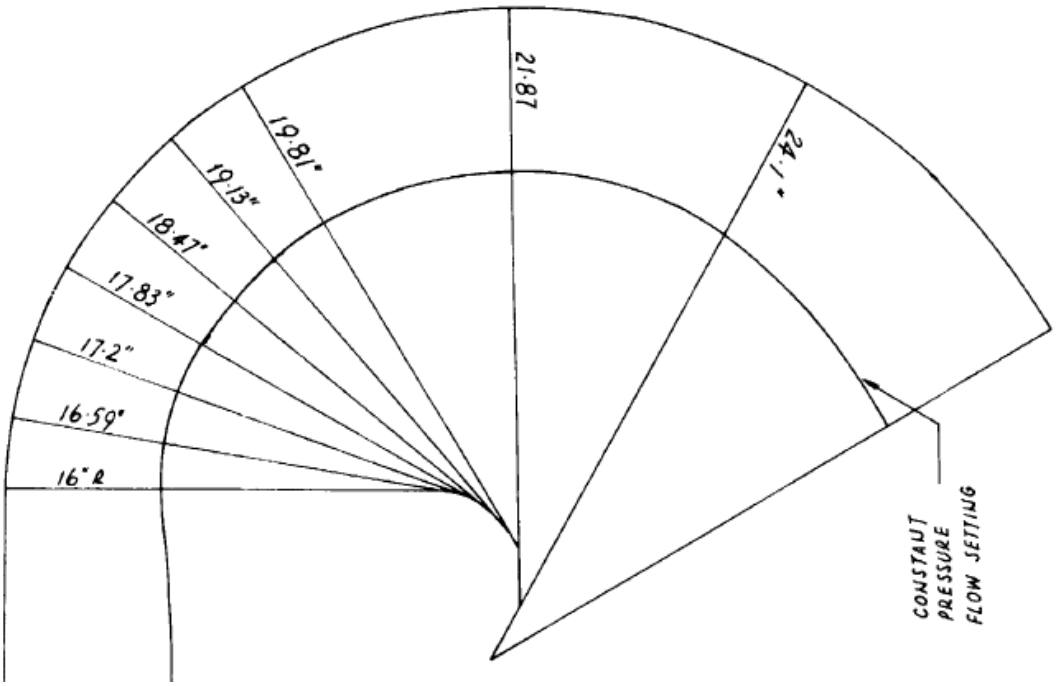

Figure A.9: So and Mellor Concave Curve. Originally Figure 4 from [41].

5. The walls are lined with static pressure taps to expressly measure the velocity in the freestream. Some ports have off-center taps as well as centerline. Measuring the flow profile was done by Conrad probes, which had a yaw axis to measure three-dimensional flow. The downside of the Conrad probes is that they interfere with the flow itself. Hot wire probes measure both the mean flow and turbulence behavior. Like the Conrad probes, these also have a yaw axis, although of different limits. So and Mellor provide their own calibration of these probes.

6. The fan that drove the wind tunnel had two settings. So and Mellor reported that the lower setting was used, but the measured data indicates that the higher setting produced the reported data. This study will match the measured data.

APPENDIX B: MPI RANK STUDY

Cases 8 and 9, a coarse flat plate $32.8\delta_{ref}$'s in length were run with varying amounts of MPI ranks. The results are in Figure B.1.

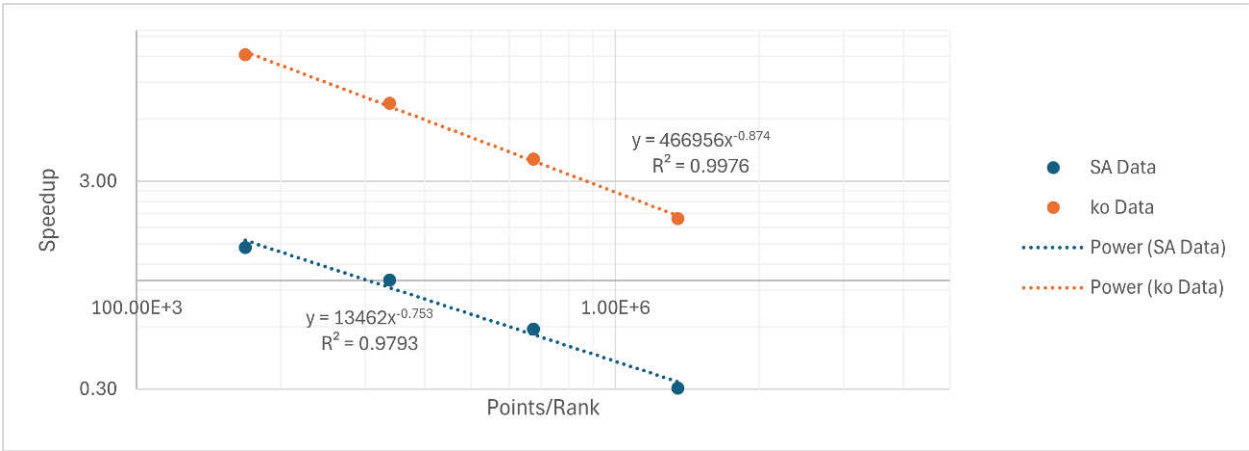

Figure B.1: MPI Rank Study Results

APPENDIX C: IMPROVED PRESSURE BOUNDARY CONDITION FORMULATION

One of the assumptions made in the set up of the CFD was a zero gradient condition for pressure at all the walls. The question after the results is - is this a valid assumption?

C.1 Equations

To understand the physics behind the 2D incompressible case, the three equations that drive the solution are continuity, as in Equations C.1 and C.2, and the Navier-Stokes momentum equations, as seen in equations C.3, C.4, and C.5.

$$\nabla \cdot \mathbf{u} = 0 \tag{C.1}$$

$$\frac{\partial u}{\partial x} + \frac{\partial v}{\partial y} = 0 \tag{C.2}$$

$$\frac{D\mathbf{u}}{Dt} = \nu \nabla^2 \mathbf{u} - \nabla(P') \tag{C.3}$$

$$\frac{\partial u}{\partial t} + u\frac{\partial u}{\partial x} + v\frac{\partial u}{\partial y} = \nu\left(\frac{\partial^2 u}{\partial x^2} + \frac{\partial^2 u}{\partial y^2}\right) - \frac{\partial P'}{\partial x} \tag{C.4}$$

$$\frac{\partial v}{\partial t} + u\frac{\partial v}{\partial x} + v\frac{\partial v}{\partial y} = \nu\left(\frac{\partial^2 v}{\partial x^2} + \frac{\partial^2 v}{\partial y^2}\right) - \frac{\partial P'}{\partial y} \tag{C.5}$$

If one were to differentiate the Navier-Stokes equation with their respective components, and combine with the incompressible continuity equation, the pressure would form a relation as in Equation C.6, as Anderson et. al. did in [15].

$$\nabla^2 P' = 2\left(\frac{\partial u}{\partial x}\frac{\partial v}{\partial y} - \frac{\partial u}{\partial y}\frac{\partial v}{\partial x}\right) \tag{C.6}$$

At the wall for a no-slip condition, velocity is zero, i.e.: $u = v = 0$. Thus, all velocity gradients at the wall are also zero, $\nabla \mathbf{u} = 0$, and furthermore $\frac{\partial^2}{\partial x^2} = 0$. This also means due to continuity that $\frac{\partial v}{\partial y} = 0$. Our study is also considering a steady state flow, thus $\frac{\partial}{\partial t} = 0$. Thus, Equations C.4, C.5, and C.6 can be written as C.7, C.8, and C.9. These equations are at a point were the solver can prescribe a boundary condition to the analysis.

$$\frac{\partial P'}{\partial x} = \nu \frac{\partial^2 u}{\partial y^2} \tag{C.7}$$

$$\frac{\partial P'}{\partial y} = \nu \frac{\partial^2 v}{\partial y^2} \tag{C.8}$$

$$\nabla^2 P' = 0 \tag{C.9}$$

BIBLIOGRAPHY

[1] Anser. https://github.com/mhland10/anser, 2024.

[2] Arc User-Guide. https://hpcsupport.utsa.edu/foswiki/bin/view/ARC/WebHome, 2024.

[3] Lonestar6 user guide. https://docs.tacc.utexas.edu/hpc/lonestar6/, 2024.

[4] OpenFOAM homepage. https://www.openfoam.com/, 2024.

[5] OpenFOAM v12 User Guide. https://doc.cfd.direct/openfoam/user-guide-v12/index, 2024.

[6] OpenFOAM v2112 User Guide. https://www.openfoam.com/, 2024.

[7] G. Araya and L. Castillo. DNS of turbulent thermal boundary layers up to Re_θ = 2300. *Int. Journal of Heat and Mass Transfer*, 64:4003–4019, 2012.

[8] G. Araya and L. Castillo. DNS of turbulent thermal boundary layers subjected to adverse pressure gradients. *Physics of Fluids*, page 095107, 2013.

[9] G. Araya and G. Torres. Structural Reynolds analogy in laminarescent boundary layers via DNS. *Journal of Visualization*, 22:529–540, 2019.

[10] V Baskaran, AJ Smits, and PN Joubert. A turbulent flow over a curved hill part 1. growth of an internal boundary layer. *Journal of Fluid Mechanics*, 182:47–83, 1987.

[11] Ian H. Bell, Jorrit Wronski, Sylvain Quoilin, and Vincent Lemort. Pure and pseudo-pure fluid thermophysical property evaluation and the open-source thermophysical property library coolprop. *Industrial & Engineering Chemistry Research*, 53(6):2498–2508, 2014.

[12] F. H. Clauser. Turbulent boundary layers in adverse pressure gradients. *Journal of the Aeronautical Sciences*, pages 91–108, 1954.

[13] D. Coles. The law of the wake in the turbulent boundary layer. 1956.

[14] D. E. Coles. The turbulent boundary layer in a compressible fluid. 1962.

[15] R. H. Pletcher R. Munipalli D. A. Anderson, J. C. Tannehill and V. Shankar. *Computational Fluid Mechanics and Heat Transfer*. CRC Press, fourth edition edition, 2021.

[16] C. Sanmiguel Vila et al. Adverse-pressure-gradient effects on turbulent boundary layers: Statistics and flow-field organization. *Flow Turbulence Combustion*, 99:589–612, 2017.

[17] C. Sanmiguel Vila et al. Adverse-pressure-gradient effects on turbulent boundary layers: Statistics and flow-field organization. *FLow Turbulence Combustion*, 99:589–612, 2020.

[18] S. E. Guarini, R. D. Moser, K. Shariff, and A. Wray. Direct Numerical Simulation of a supersonic turbulent boundary layer at Mach 2.5. *Journal of Fluid Mechanics*, 414:1–33, 2000.

[19] W. M. Kays and M. E. Crawford. *Convective Heat and Mass Transfer*. McGraw-Hill, 3rd edition, 1993.

[20] P. S. Klebanoff. Characteristics of turbulence in a boundary layer with zero pressure gradient. 1956.

[21] S. V. Patankar L. S. Caretto, A. D. Gosman and D. B. Spalding. Two calculation procedures for steady, three-dimensional flows with recirculation. *Lecture Notes in Physics*, 2007.

[22] B. B. Mandelbrot. *The (Mis)Behavior of Markets*. Profile Books, 2008.

[23] M. P. Martin and S. Priebe. Turbulence in a hypersonic compression ramp flow. *Physics Review of Fluids*, 6, 2021.

[24] I. Marusic and A. E. Perry. A wall-wake model for the turbulence structure of boundary layers. part 1. extension of the attached eddy hypothesis. *Journal of Fluid Mechanics*, 298:361–388, 1995.

[25] I. Marusic and A. E. Perry. A wall-wake model for the turbulence structure of boundary layers. part 2. further experimental support. *Journal of Fluid Mechanics*, 298:389–407, 1995.

[26] F. R. Menter. Zonal two equation equation k-Ï turbulence models for aerodynamic flows. Technical Report 93-2906, AIAA, 1993.

[27] A. G. Zditovets N. A. Kiselev, N. S. Malastowski and Y. A. Vinogradov. Reynolds analogy violation for a compressible turbulent boundary layer with pressure gradient in a small-size superosnic slot channel. *International Journal of Thermal Sciences*, 200, 2024.

[28] I. M. Cohen P. K. Kundu and D. R. Dowling. *Fluid Mechanics*. AP Press, sixth edition edition, 2012.

[29] D. Paeres, C. Lagares, and G. Araya. Assessment of turbulence models over a curve hill flow with passive scalar transport. *Energies*, 15, 2022.

[30] V. C. Patel. Measurements of secondary flow in the boundary layers of a 180 degree channel. 1968.

[31] W. P. Patrick. Flowfield measurements in a separated and reattached flat plate turbulent boundary layer. Technical report, NASA Lewis Research Center, 1987.

[32] S. B. Pope. *Turbulent Flows*. Cambridge University Press, 2003.

[33] H. Schmidbauer. Behavior of turbulent boundary layers on curved convex walls. 1936.

[34] R. Simpson. Two-dimensional turbulent separated flow. *AGARDograph*, 287:Vol I, 1985.

[35] R. L. Simpson. Turbulent boundary layer separation. *Annual Review of Fluid Mechanics*, 21:205–234, 1989.

[36] R. L. Simpson, Y. Chew, and B. G. Shivaprasad. The structure of a separating turbulent boundary layer. Part 1. Mean flow and Reynolds stresses. *Journal of Fluid Mechanics*, 113:23–51, 1981.

[37] R. L. Simpson, Y. Chew, and B. G. Shivaprasad. The structure of a separating turbulent boundary layer. Part 2. Higher-Order Turbulence Results. *Journal of Fluid Mechanics*, 113:53–73, 1981.

[38] R. L. Simpson, M. Ghodbane, and B. E. McGrath. Surface pressure fluctuations in a separating turbulent boundary layer. *Journal of Fluid Mechanics*, 177:167–186, 1987.

[39] M. Skote, D. Henningson, and R. Henkes. Direct numerical simulation of self-similar turbulent boundary layers in adverse pressure gradients. *Flow, Turbul. Combust.*, 60:47–85, 1998.

[40] R. M. C. So. Pressure gradient effects on reynolds analogy for constant property equilibrium turbulent boundary layers. *International Journal of Heat Mass Transfer*, 37(1):27–41, 1993.

[41] R. M. C. So and G. L. Mellor. An experimental investigation of turbulent boundary layers along curved surfaces. Technical report, NASA Lewis Research Center, 1972.

[42] P. R. Spalart and S. R. Allmaras. A one-equation turbulence model for aerodynamic flows. *La Recherche Aerospatiale*, (1):5–21, 1992.

[43] P. R. Spalart and C. L. Rumsey. Effective inflow conditions for turbulence models in aerodynamic calculations. *AIAA Journal*, 45(10), 2007.

[44] Z. Warhaft. Passive scalars in turbulent flows. *Ann. Rev. Fluid Mechanics*, 32:203–240, 2000.

[45] F. M. White and J. Majdalani. *Viscous Fluid Flow*. McGraw-HIll, fourth edition edition, 2022.

[46] D. C. Wilcox. Re-assessment of the scale determining equation for advanced turbulence models. *AIAA Journal*, 26:1299–1310, 1988.

VITA

Matthew Holland was born in Houston, TX in 1996. He earned a Bachelor of Science in Mechanical Engineering, with a minor in Aerospace Engineering from Texas A&M University in 2020. After graduation, Matthew went to work at Dynetics on their Human Landing System program to develop pumps for the main engines on the lander. He led the fluids development for the pumps, and created CFD models to inform the pump design. After the end of the program, he went to work at Hermeus and Southwest Research Institute. Matthew's focus has been advanced aerospace propulsion.

He currently attends the University of Texas at San Antonio, expecting to graduate with a Masters of Science in December 2024 after starting the degree in August 2023. His specialty has become spectral methods and principal component analysis applied to modeling and simulation, CFD specifically, on top of aerospace propulsion. He has also become capable at using HPC systems with parallel processing and GPU-acceleration. During the degree, he had an internship with NASA Glenn Research Center where he applied his specialty to create a CFD post-processing software that makes the results more effective in informing engineering design.